**Centro de Investigación Científica y de Educación Superior de Ensenada, Baja California**


---

**Doctorado en Ciencias**
**en Ciencias de la Tierra con orientación en Geología**

---

# The conductive and advective heat flow budget across the Gulf of California rift system

Tesis

para cubrir parcialmente los requisitos necesarios para obtener el grado de

Doctor en Ciencias

Presenta:

**Florian Neumann**

Ensenada, Baja California, México

2017

Tesis defendida por

**Florian Neumann**

y aprobada por el siguiente Comité

Dra. Raquel Negrete Aranda

Codirector del Comité

Dr. Juan Contreras Pérez

Codirector del Comité

Dr. Arturo Jesús Martín Barajas

Dr. Edgardo Cañón Tapia

Dr. Luis Alonso Gallardo Delgado

Dr. John Sclater

Dr. Juan García Abdeslem

Coordinador del Programa de Posgrado en Ciencias de la Tierra

Dra. Rufina Hernández Martínez

Directora de Estudios de Posgrado

Abstract of the thesis presented by Florian Neumann as a partial requirement to obtain the Doctor of Science degree in Earth Science with orientation in Geology.

**The conductive and advective heat flow budget across the Gulf of California rift system**

Abstract approved by:

| Dra. Raquel Negrete Aranda | Dr. Juan Contreras Pérez |
|---|---|
| Thesis Co-Director | Thesis Co-Director |

A primary control on the geodynamics of rifting is the thermal regime. To better understand the thermal regime of the northern Gulf of California we systematically measured heat-flow across the Wagner Basin, a tectonically active basin that lies at the southern terminus of the Cerro Prieto fault. Seismic reflection profiles show sediment in excess of 5 s two-way travel time implying a sediment thickness $>$ 5 km. The heat flow profile is 40 km long, has a nominal measurement spacing of $\sim$ 1 km, and is collocated with a seismic reflection profile. Heat flow measurements were made with a 6.5 m Fielax violin-bow probe. Most measurements are of good quality in that the probe fully penetrated sediments and measurements were stable enough to perform reliable inversion for heat flow and thermal properties. We have estimated corrections for environment perturbations due to sedimentation and changes in bottom water temperature. The mean and standard deviation of heat flow across the western, central, and eastern parts of the basin are 220 $\pm$ 60, 99 $\pm$ 14, 889 $\pm$ 419 mW m$^{-2}$, respectively. Corrections for sedimentation would increase heat flow across the central part of basin by 40 to 60%. We interpret the relatively high heat flow and large variability on the western and eastern flanks in terms fluid discharge, whereas the more consistent values across the central part of the basin is suggestive of conductive heat transfer. This interpretation is consistent with the seismically imaged pattern of faulting showing faults near the seafloor across the western and eastern flanks of the Basin. Based on an observed fault depth of 1.75 km we estimate the Darcy velocities through the western and eastern flanks at 2 and 8 cm/yr, respectively.

Keywords: **Gulf of California Extensional Province; Narrow rift; Wide rift; Distributed deformation; Advective heat transport**

Resumen de la tesis que presenta Florian Neumann como requisito parcial para la obtención del grado de Doctor en Ciencias en Ciencias de la Tierra.

**El presupuesto de flujo de calor conductivo y advectivo en el sistema de fallas del Golfo de California**

Resumen aprobado por:

| Dra. Raquel Negrete Aranda | Dr. Juan Contreras Pérez |
|---|---|
| Codirector de Tesis | Codirector de Tesis |

Un control primario sobre la geodinámica del rifting es el régimen térmico. Para comprender mejor el régimen térmico del norte del Golfo de California, medimos de forma sistemática el flujo de calor en la cuenca Wagner, una cuenca tectonicamente activa que se encuentra en el extremo sur de la falla Cerro Prieto. Los perfiles de sísmica de reflexión muestran los sedimentos en exceso de 5 s de tiempo doble, lo que implica un espesor de los sedimentos $>$ 5 km. El perfil de flujo de calor tiene 40 km de longitud, tiene un espaciamiento nominal de $\sim$ 1 km, y está colocado con un perfil de sísmica de reflexión. Las mediciones de flujo de calor se realizaron con una sonda tipo arco de violín de la compañía Fielax con una longitud de 6,5 m. La mayoría de las mediciones son de buena calidad ya que la sonda penetró completamente en los sedimentos y las mediciones fueron lo suficientemente estables como para realizar una inversión fiable del flujo de calor y de las propiedades térmicas. Hemos estimado las correcciones para las perturbaciones ambientales debido a la sedimentación y los cambios en la temperatura del agua del fondo. La media y la desviación típica del flujo de calor a través de las partes occidental, central y oriental de la cuenca son 220 $\pm$ 60, 99 $\pm$ 14, 889 $\pm$ 419 mW m$^{-2}$, respectivamente. Las correcciones para la sedimentación aumentarían el flujo de calor en la parte central de la cuenca en un 40 a 60 %. Interpretamos el flujo de calor relativamente alto y la gran variabilidad en los flancos occidental y oriental en términos de descarga de fluido, mientras que los valores más consistentes a través de la parte central de la cuenca sugieren la transferencia de calor conductiva. Esta interpretación es consistente con el patrón sísmico de fallas mostrando fallas cerca del fondo marino a través de los flancos occidental y oriental de la Cuenca. Basándonos en una profundidad de falla observada de 1,75 km estimamos las velocidades de Darcy a través de los flancos occidental y oriental a 2 y 8 cm / año, respectivamente.

Palabras Clave: **Golfo de California, Deformación distribuida, Transporte de calor advectivo**

# Dedication

*To my mother, Katharina Neumann*

*Her support, encouragement, and constant love have sustained me throughout my life.*

*In memory of my father*

*Heinrich Neumann*

## Acknowledgement

The **Consejo Nacional de Ciencia y Tecnología** (CONACYT), the National Council of Science and Technology for founding my postgraduate studies and my stay at Oregon State University through the scholarship number 242956.

The **Centro de Investigación Científica y de Educación Superior de Ensenada** (CICESE), the Center of Scientific Research and Higher Education of Ensenada, especially the Department of Scholar Service and Postgraduate Coordination at the Earth Science Devision. Thanks to the Geology, Geophysics and Seismology Department at CICESE and their faculty members, technical and administrative staff.

The **Centro Mexicano para la Innovación en Energía Geotérmica** (CEMIE Geo), the Mexican Center for Innovation in Geothermal Energy for their support to realize my work and a three month scholarship.

I want to thank my thesis advisers **Dr. Raquel Negrete-Aranda** and **Dr. Juan Contreras** for their support, professional and personal advises, positivism, motivation and patience. Their guidance helped me in all the time of research and writing of this thesis. I could not have imagined having a better advisors and mentors for my work.
I remember very well my first course at CICESE, I just arrived from Germany and next to the board was Juan talking about Geodynamics and scales. At this class I knew, that I wanted to work with him. Now 7 years later I think it was the best choice of my life working with you!
Raquel inspired my to this work, she was always supportive, enthusiastic and energetic during the last 4 years.
To both thank you for being always as you are. I hope that I could be as lively, motivated and energetic as well as you are.

Thanks to my thesis committee: **Dr. Arturo Jesús Martín Barajas, Dr. Edgardo Cañón Tapia, Dr. Luis Alonso Gallardo Delgado** and **Dr. John Sclater** for their time, teachings and valuable

discussions. Especially, I would like to thank John Sclater for having my several times at SCRIPPS and his valuable contributions to the published manuscript.

To **Robert Harris** from Oregon State University for his patience and great support during my stay in Corvallis. Without you I never had made it this far. It was great meeting and working with you. Also to his wife Shelly for having my at their home for two weeks, I had a great time and I'm thankful meeting you both.

I'd like to thank **Dr. Antonio González** for letting me be involved in the project from the beginning and for giving me the facilities to develop the thesis with data collected on board the *Alpha Helix, R/V*.

To the technical and administrative staff of the Earth Science Department, who always had an open door and helped me with problems I encountered during the last few years. Especially thanks to Martha Barrera, Ana Rosa Soto, Magdalena Chavez, Enid Moran, Sergio Arriegui, Humberto Benítez, José Mojarro, Mari Carmen and Celica Cuevas.

To the captain and the crew at "R/V Alpha Helix".

To my friends Olaf Cortes, Erik Ramirez, Claudia Quinteros, Fransisco del Toro, Xochitl Torres, Usama Yarbuh, Nestor Ramirez, Karina Gomez, Diego Tamayo, Tomas Pena, Gina Villalobos, Samuel Villareal, Karen Legorreta, Susana Alfaro, Renee Gonzalez, Rocio Arellano, Daniela Tazzo, the hockey crew and to many other equally important.

To my friends in Germany Timm, Mario, Kathrin, Hanna, Steffie's.

To all the people I met during my stay at OSU, especially Ale, the crew from BSP and all guys from CH3.

Finally, thanks to my loving family and my love Anna Shlyagina for their important support.

# Content

Page

# Content (continuation)

# List of figures

# List of figures (continuation)

# List of tables

## Sinopsis

El Gobierno Federal de México propuso dentro de su Plan para el Desarrollo, generar 20% de su energía a partir de fuentes renovables. Por esta razón, la Secretaria de Energía creó el Centro Mexicano de Innovación en Energía Geotérmica (CeMIE-Geo). El CeMIE-Geo esta formado por varias instituciones académicas, empresas y entidades federales con el fin de la investigación del aprovechamiento de la energía geométrica.

Este trabajo es parte del proyecto “Campaña Intensiva de Exploración Geotérmica de las Cuencas Wagner, Consag, Delfín, Guaymas y Alarcón del Sistema de Rifts del Golfo de California".

En este proyecto se levantaron 33 datos de flujo de calor a lo largo de la cuenca Wagner en el Alto Gulfo de California. El perfil mide 40 km con un espaciamiento de $\sim$ 1 km y esta colocado sobre un perfil de sísmica de reflexión, procesado e interpretado por Aragón-Arreola y Martín-Barajas (2007). Las mediciones de flujo de calor se hicieron con una sonda tipo arco de violin, construida por la compañía FIELAX con una longitude de 6 m. Sobre la sonda de acero inoxidable esta montado el sensor (6 m) que contiene 22 termistores, donde se registran las temperaturas del subsuelo. Para obtener una medición de flujo de calor es necesario realizar 6 pasos: A) La sonda se baja hacia fondo marino; B) La sonda penetra el sedimento y en este paso las temperaturas aumenten debido a la fricción entre el sensor y el sedimento; C) El decaimiento de las temperaturas generado por la fricción determina las temperaturas de equilibrio y se calcula el gradiente térmico; D) Después de un tiempo determinado, donde la sonda se encuentra en condiciones estables, se dispara un pulso de calor (20 s); E) Se mide el decaimiento durante 20 minutos, en donde se calcula las propiedades termicas del sedimento como la conductividad y la difusividad térmica; F) Por último la sonda se retira del fondo marino.

Los datos levantados se analizaron y procesaron usando el método establecido por Hartmann y Villinger (2002). Las mediciones de flujo de calor en general se realizan a altas profundidades (> 1500 m) para reducir los efectos de la variación de la temperatura del fondo, inducida por efectos climáticos. La cuenca Wagner tiene una profundidad máxima de $\sim$ 250 m, y por lo cual, su temperatura del subsuelo esta fuertemente alterada por la variación de la temperatura de superficie. Además de la variación de la temperatura de fondo, el flujo de calor es reducido por el efecto de una sedimentación rápida. Los sedimentos pueden reducir los flujos de calor superficiales hasta que el paquete de los sedimentos llegan a una temperatura de fondo estable. Los sedimentos en el Alto Golfo de California llagan a alcanzar un espesor de > 7 km (Persaud *et al.*, 2003; Aragón-

Arreola y Martín-Barajas 2007; González-Fernández *et al*,. 2005; González-Escobar *et al*., 2009). Los datos deben de corregirse por estos dos efectos. Para el efecto de la temperatura de fondo, se generó un método usando una aproximación sinusoidal con periodo anual. La solución para la ecuación de conducción de calor dependiente del tiempo, unidimensional es: $T(z,t) = T_0 + \Gamma z + \Delta T \exp\left(-z\sqrt{\frac{\omega}{2\kappa}}\right) cos\left(\omega t - z\sqrt{\frac{\omega}{2\kappa}}\right)$, donde $T$ es la temperatura, $t$ el tiempo, $T_0$ es la variación de la temperatura de fondo a largo plazo, $\Gamma z$ el gradiente térmico profundo, $\Delta T$ la amplitud de la variación de la temperatura de fondo, $\kappa$ la difusividad térmica y $\omega$ la frecuencia angular. El gradiente térmico profundo se substituye por el análisis de Bullard (Bullard, 1939). El término exponencial describe la atenuación de la onda térmica y significa que para variaciones cortas (diurnas) la penetración es menor que para variaciones largas (anuales).

La ecuación anterior se emplea para determinar $T_0$, $\Gamma z$, $\Delta T$ y, haciendo el análisis de sensibilidad, resulta que los procentajes de variabilidad de los parametros estimados son bajos ( 2%).

Para explorar la naturaleza de la variación de la temperatura de fondo se usaron perfiles CTD, (Conductividad, Temperatura y Profundidad) en sus siglas en ingles. Se analizaron 1163 perfiles tipo CTD para demostrar, primero, que la variación anual se comporta como una señal sinusoidal y, segundo, que la variación total en superficie es entre 16.4° y 31.0° y para una profundidad de 200 m entre 13.4° y 16.4°.

En el caso del efecto de sedimentación, asumiendo que la taza de sedimentación es de 1-2 mm yr$^{-1}$ en los últimos 5-6 Myr años, la depresión del flujo de calor es aproximadamente 40%.

Los resultados están divididos en tres regiones a lo largo de la cuenca Wagner, la parte occidental donde se observa un promedio de 220 mW m$^{-2}$, la parte central con un valor de 99 mW m$^{-2}$ y la parte oriental con un valor de flujo de calor de 889 mW m$^{-2}$. La parte occidental representa valores ligeramente elevados con respecto a la parte central, donde los valores son relativamente consistentes. La parte oriental representa valores muy altos y variables. El flujo de calor en la parte central de la cuenca, después de la corrección por sedimentación es de 150 mW m$^{-2}$, el cual es apropiado y interpretado como el flujo de calor de fondo. Los valores de flujo de calor en las partes occidental y oriental, por otra parte, están interpretados como flujos enfocado de fluidos.

El análisis del flujo advectivo indica que las velocidades de Darcy usando una profundidad promedio de las fallas de $\sim$ 1.75 km, son de 2 y 8 cm yr$^{-}1$ para la parte occidental y oriental, respectivamente.

El valor para la parte central (150 mW $m^{-2}$) coincide con un modelo establecido por Lachenbruch *et al*., (1985) en el área del Salton Trough, al norte de la cuenca Wagner. Para calcular este flujo se usaron dos diferentes modelos, uno que incluye el flujo de calor superficial orginando por de intrusións magmaticas por debajo de la corteza y otro causado por la intrusión por diques. Si hay intrusión por diques significa que la corteza esta rota, mientras que en el caso de intrusión por debajo de la placa significa que la litosfera esta en proceso de ruptura.

Los resultados de los modelos son de 113 mW $m^{-2}$ y 173 mW $m^{-2}$ para la intrusión magmatica por debajo de la placa y la intrusión por diques, respectivamente.

Concluyendo se puede decir que el valor de flujo de calor en la parte central de la cuenca Wagner es de 150 mW $m^{-2}$ el cual, coincide con el modelo de intrusión magmatica por debajo de la placa y con el valor calculado basado en un análisis de isotermas de Curie de 126 mW $m^{-2}$.

# Chapter 1. Introduction

The Mexican Government proposed, as part of its National Development plan 2020, to generated 20% of its energy from renewable sources. For this purpose, the Secretary of Energy created *El Centro Mexicano para la Innovación en Energía Geotérmica*, (CeMIE-Geo, 2014) (the Mexican Center for Innovation in Geothermal Energy). It combines 23 academic institutions, companies and government entities and houses four major strategic research lines and several laboratories. One of its goals is the development of innovative exploration techniques for geothermal resources. Mexico has an installed thermal capacity (MWt) of 155.82 (Lund and Boyd, 2016) and has the fourth greatest geothermal energy production with an installed capacity of 958 MW (Bertani, 2012) operating at four major geothermal fields which produces 2.3% of the country energy (Flores-Armenta *et al.*, 2014).

This thesis is part of the project: *Intensive survey of geothermal exploration in Wagner, Consag, Delfín, Guaymas and Alarcón basins in the Gulf of California rift system* (P03), led by Dr. Antonio González Fernández at the Centro de Investigación Científica y de Educación Superior de Ensenada, (CICESE), (the Ensenada Center for Scientific Research and Higher Education). As part of this project, high resolution heat flow data were taken in the Northern Gulf of California (NGOC). Data acquisition was carried out with CICESE's oceanographic research vessel ALPHA HELIX R/V, using a (FIELAX, 2017) mulitpenetration heat flow probe instrument. Data analysis was carried out in collaboration with CICESE, CEOAS (College of Earth, Ocean, and Atmospheric Sciences) at Oregon State University and SCRIPPS Institution of Oceanography.

## 1.1 Basic heat terms

Before progressing into further chapters it is useful to revise some basic geothermal terms which are extensively used throughout the text. Firstly, it is not questioned that the interior of the Earth is hotter than the surface. Heat is transported by different mechanism from its interior to the surface, where it is radiated into space. Moreover, the rheology of earth materials is primarily a function of temperature and therefore, to understand the Earth's interior, we must understand its thermal structure. Most of the Earth's heat loss occurs through the oceans (71%) and results from cooling of new oceanic lithosphere created at mid-ocean ridges. The global present-day Earth's

heat loss is estimated about 44.2 $\pm$ 1.0 $\times$ $10^{12}$ W. Pollack *et al.* (1993) estimated an average global heat flow of 87 $\pm$ 2 mW $m^{-2}$ using 20,201 measurements. The average heat flow for the continents and the oceans is 65 $\pm$ 1.6 mW $m^{-2}$ and 101 $\pm$ 2.2 mW $m^{-2}$, respectively.

Heat transfers by *conduction*, *convection*, and *radiation*. Conduction is the transfer of heat at atomic and molecular scale. If a material is heated up, particles gain more energy and vibrate more. The molecules transfer their energy colliding with other particles. The better the conductor, the faster the heat is transfered. This process continues until the material reaches thermal equilibrium. Conduction dominates within Earth's crust (Beardsmore and Cull, 2001; Fowler, 1990; Turcotte and Schubert, 2014).

Convective heat is transfered by when the particles themselves move. It occurs when the heavier colder fluids displace warmer fluids. Under a continuous heat sources, this results in continuous circulation patterns. Examples occur in boiling water or as well as air circulation in the atmosphere. Generally, convection transfers heat faster than conduction and it is the dominant heat transfer in the Earth's mantle, whereas Finally, heat transfer by radiation involves electromagnetic radiation through empty space, often called infrared radiation. This process is responsible for the heat transferred from the Sun.

**Temperature**, (hereafter noted as T) is a physical property. Naturally known as the degree of hotness or coldness measured on a defined scale in SI units is measured in Kelvin (K). Its value is closely linked to the amount of disordered particle movement. If one part of a material is heated, its temperature rises gradually and disseminates towards regions with lower temperature.

**Thermal Gradient** given by Equation 1 is defined as the spatial temperature variation and it is expressed by temperature per unit distance (K $m^{-1}$). In general the thermal gradient is a vector quantity, and its vertical component is given by:

$$\frac{dT}{dz} = \frac{T_2 - T_1}{dz}, \qquad T_2 > T_1 \tag{1}$$

**Heat flow** is the rate at which the heat traverses a unitary surface. According to the Fourier equation when the heat is conductively transferred through a material is proportional to the thermal

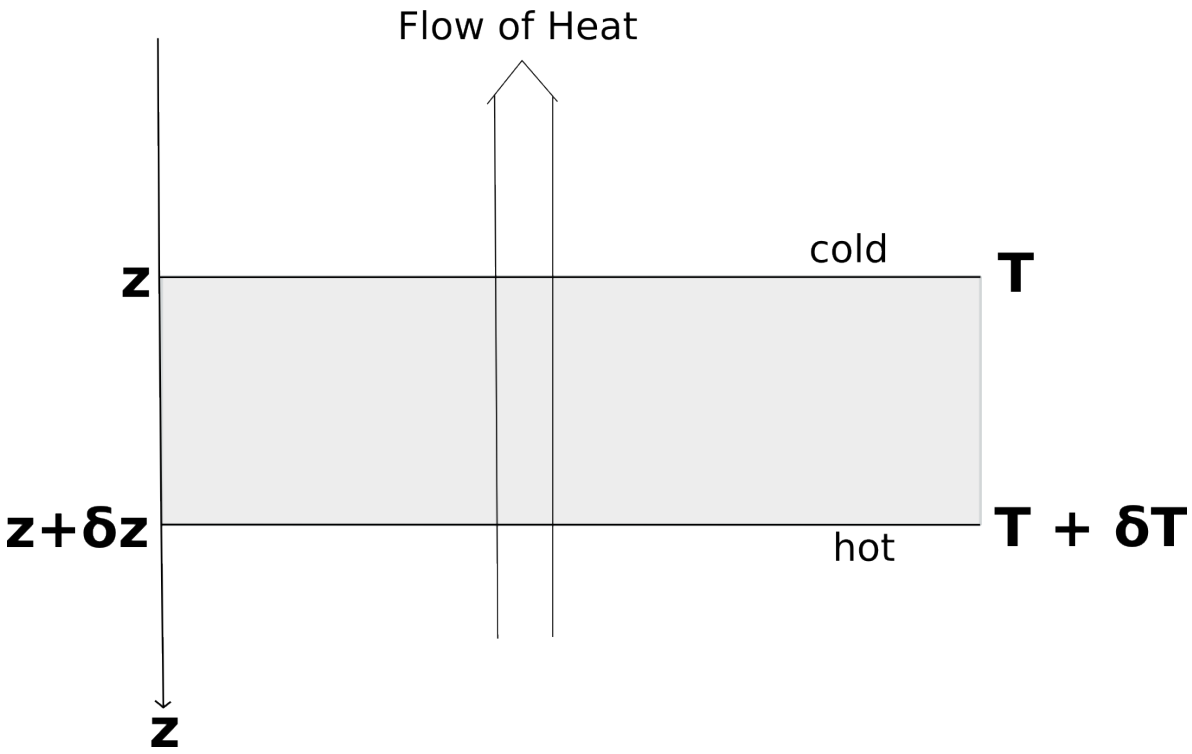


**Figure 1.** Illustration of 1D conductive heat transfer through an infinitely wide and long plate with thickness $\delta z$.

gradient.

For this case, the heat flow is given by:

$$q_z(z) = -k\frac{T + \delta T - T}{z + \delta z - z} = -k\frac{\delta T}{\delta z}, \tag{2}$$

as $\delta z \to 0$, Equation 2 is written

$$q_z(z) = -k\frac{\partial T}{\partial z}, \tag{3}$$

In SI $q$ is expressed in units of watt per square meter (W $m^{-2}$) and in its more general form it is a vector quantity. Many older publications give heat flow parameters in units other than SI (Système international d'unités) and therefore, a conversion of historical measurements is necessary. Table 1 shows SI unit and the equivalent values for centigram-gram-second (cgs) and foot-pound-second (fps) for the most important thermal parameters. Geothermal data is often quoted in heat flow units (1 HFU = $10^{-6}$cal $cm^{-2}$ $s^{-1}$ = 41.87 m W $m^{-2}$), heat generation units (1 HGU = $10^{-13}$cal $cm^{-3}$ $s^{-1}$ = 0.4187 $\mu$ W $m^{-3}$) and thermal conductivity units (1 TCU = $10^{-3}$cal $cm^{-1}$ $^{\circ}C^{-1}$ $s^{-1}$ = 0.4187 W $m^{-1}$ $K^{-1}$).

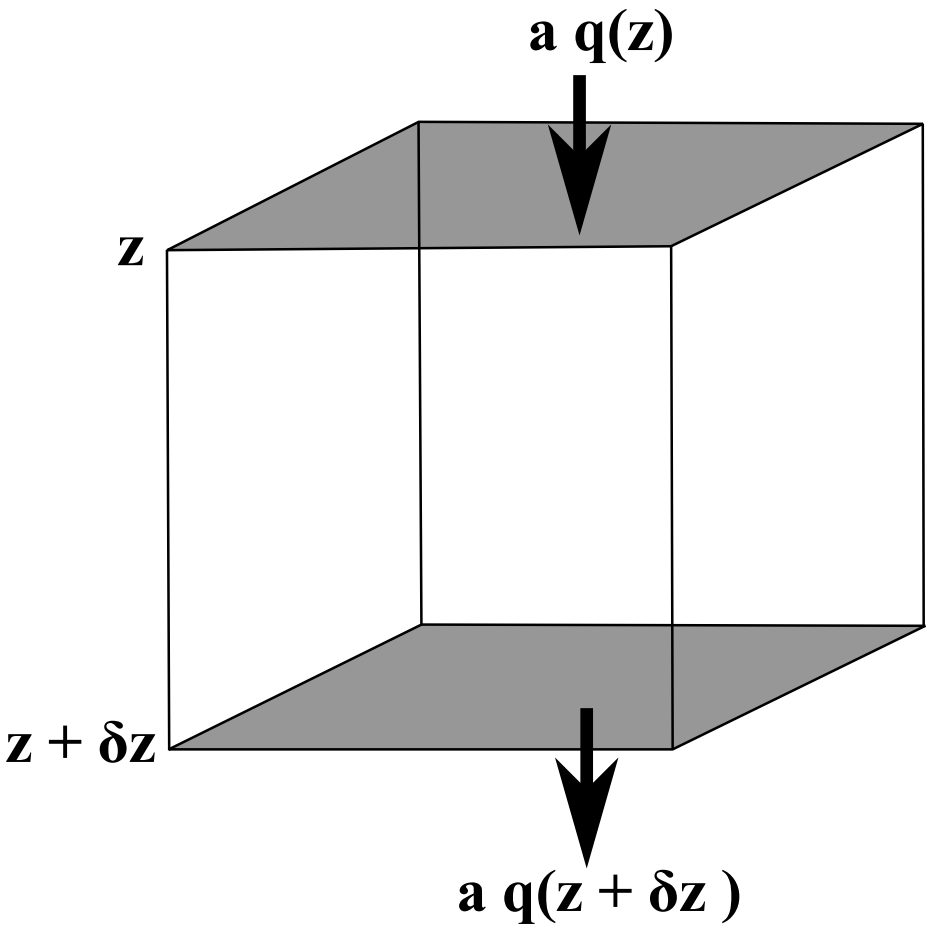


**Figure 2.** Conductive heat transfer through a volume element with height $\delta z$ and cross-sectional area $a$. We assume that heat is only conducted through the shaded areas.

**Thermal conductivity** $(k)$, physical property of the material that relates the heat flow vector to the gradient vector and it is expressed in watts per meter per degree Kelvin (W $m^{-1}K^{-1}$). The thermal conductivity is a physical property of the material.

By convention, a positive heat flow is defined in the direction of decreasing temperature, which is the opposite of the thermal gradient and the reason for the negative sign. Equation 3 is better known as *Fourier's law* in one dimension, it doesn't account for lateral heat flow, heat generation within the measured interval, advective heat transport and temporal variation in heat flow.

Now we consider a small volume element (Figure 2) with height $\delta z$ and cross-sectional area $a$. Change in temperature $\delta T$ and time $\delta t$ depends on the in- and outflow, the heat generation within the volume and thermal capacity. The heat entering $(aq(z))$ the volume must be equal to the heat leaving $(aq(z + \delta z))$. Expanding the second term using a Taylor series:

$$q(z+\delta z) = q(z) + \delta z \frac{\partial q}{\partial z} + \frac{(\delta z)^2}{2}\frac{\partial^2 q}{\partial z^2} + ... \tag{4}$$

All the terms after the second term are small, and can be neglected. From Equation 4, we can now determine the difference between the entering and leaving heat of the volume.

$$= aq(z) - aq(z+\delta z) = -a\delta z \frac{\partial q}{\partial z} \tag{5}$$

Assuming a **heat generation** within the volume at a rate H per unit volume per unit time, the total amount is then $Ha\delta z$. Combining this with Equation 5, the total heat gain per unit time is: $Ha\delta z - a\delta z \frac{\partial q}{\partial z}$

If the material has a **density** $\rho$, a **specific heat** $c_p$, and a temperature increase $\delta T$ in time $\delta t$, heat gain is: $c_p a \delta z \rho \frac{\delta T}{\delta t}$

**Specific heat** is defined by the amount of heat required to raise the temperature of a unit mass of a substance by one unit of temperature. Thus, equating expressions for the heat gain per unit volume per unit time and and the heat gain of the material, assuming the case when $\delta z, \delta t \to 0$ and substituting Fourier's law (Equation 3) gives:

$$\frac{\partial T}{\partial t} = \frac{k}{\rho c_p}\frac{\partial^2 T}{\partial z^2} + \frac{H}{\rho c_p} \tag{6}$$

This is the one-dimensional heat conduction equation, one of the most important equations in geophysics. The term $\frac{k}{\rho c_p}$ is known as the **thermal diffusivity** $\kappa$ and it expresses how a substance lose heat by conduction.

**Thermal resistance** $(R)$ is defined as the reciprocal of the thermal conductivity $k$, over a depth range $z$:

$$R = \sum_{i=1}^{N} \frac{\Delta z_i}{k(z)_i} \tag{7}$$

The thermal resistance is a measure of how effectively a material retards the flow of heat. If $T$ is the temperature at depth,

$$T = T_o + q_0 \sum_{i=1}^{N} \frac{\Delta z_i}{k(z)_i} \tag{8}$$

**Table 1.** Systeme International d'Unites (SI) thermal parameters units and equivalent values for the Centimetre-Gram-Second (cgs) and Foot-Pound-Second (FPS) Measurement Systems

| Parameter | SI Unit | cgs System | fps System |
|---|---|---|---|
| Temperature | Kelvin (K) | Celsius (°C)<br>SI-273.15 | Fahrenheit (°F)<br>SI×1.8 - 459.67 |
| Energy/heat | joules (J) | calories (cal)<br>SI×0.2388 | BTU*<br>SI/1055 |
| Power | watts (W) | cal $s^{-1}$<br>SI×0.2388 | BTU* $h^{-1}$<br>SI×3.413 |
| Heat Flow | W $m^{-2}$ | cal $cm^{-2}$ $s^{-1}$<br>SI×0.2388×$10^{-5}$ | BTU* $ft^{-2}day^{-1}$<br>SI×7.608 |
| Thermal conductivity | W $m^{-1}$ $K^{-1}$ | cal $cm^{-1}$ $C^{-1}$ $s^{-1}$<br>SI×0.2388×$10^{-5}$ | BTU* $ft^{-1}$ $F^{-1}$ $h^{-1}$<br>SI×0.578 |
| Thermal diffusivity | $m^2$ $s^{-1}$ | $cm^2$ $s^{-1}$<br>SI×$10^4$ | $ft^2$ $h^{-1}$<br>SI×3.875×$10^4$ |
| Heat generation | W $m^{-3}$ | cal $cm^{-3}$ $s^{-1}$<br>SI×2.388×$10^{-7}$ | BTU* $ft^{-3}$ $day^{-1}$<br>SI×2.319 |

where $T_0$ is the surface temperature and $q_0$ the heat flow. This equation has a linear relationship between the measured quantities $T$ and $\sum \frac{z}{k}$. A graph, where temperature is plotted against the thermal resistance is called a **Bullard plot** (Bullard, 1939).

### 1.2 Geothermal energy

Geothermal energy is the energy stored in the form of heat below the surface of the solid earth. The word *geothermal* comes from the ancient Greek words *geo*, meaning Earth and *therme* meaning heat. It results from the original energy transformed since the formation of the Earth 4.54 Ga years ago and from the radioactive decay of unstable isotopes within the Earth's crust. Approximately 98% of the radiogenic heat arises from the the decay of uranium ($^{238}$U), thorium ($^{232}$Th) and potassium ($^{40}$K) isotopes. Within the Earth's crust the mean temperature increases 3°C per 100 m depth. 70% of the surface heat flow originates in the crust and 30% comes from the mantle and the Earth's core. The integrated heat flow over the whole Earth's surface results in an impressive thermal power of 40 million megawatts (Stober and Bucher, 2012).

The largest piece of electricity generated from renewable energies in 2008 was hydroelectric power with 860 $GW_{el}$ followed by wind power with 121 $GW_{el}$ and the biomass with 52 $GW_{el}$ (Stober and Bucher, 2012). Solar and geothermal power only produced 11 $GW_{el}$ in 2008. In terms

of thermal energy production leads biomass with 250 $GW_{th}$ followed by solar with 145 $GW_{th}$ and geothermal with 50 $GW_{th}$ (Bertani, 2005, 2012). In 2010, 24 countries used geothermal energy to produce electrical power. Since 1975 the use of geothermal energy increased constantly. In the period between 1980 and 2005 the installed geothermal capacity increased $\sim$ 200 $MW_{el}/a$. Since 2005 an increase of $\sim$ 500 $MW_{el}/a$ is observed (Stober and Bucher, 2012). In 2008 the United States of America had the worldwide highest installed geothermal capacity, with 3040 $MW_{th}$, followed by Philippines (1970 $MW_{th}$), Indonesia (992 $MW_{th}$), Mexico (958 $MW_{th}$), Italy (811 $MW_{th}$), New Zealand (632 $MW_{th}$), Iceland (575 $MW_{th}$) and Japan (535 $MW_{th}$). Geothermal energy has gained in importance in the last decades and it is a new hope for the future energy supply of the planet because of its almost inexhaustible source of energy, its practically everywhere and it regenerates itself continuously.

### 1.3 Gulf of California

The Gulf of California (GC) is a natural laboratory to study the transition from continental rifting to rupture and seafloor spreading (Fig. 3). The GC is a 1200 km long transtensional rift system between Baja California, a sliver of continental lithosphere on the Pacific plate, and the western margin of the North-American continent. The GC links the right lateral continental San Andreas Fault system in the north with the oceanic East Pacific Rise in the south through a series of long transforms separating short rift basins and currently transitions from well developed oceanic spreading in the southern Gulf at the Alarcón basin to continental rifting in the Salton Trough.

Extension in the Gulf began 12-12.5 Myr ago when subduction of the Farallon plate ended west of Baja California (Lonsdale, 1989, 1991; Stock and Lee, 1994; Umhoefer, 2011). At $\sim$ 6 Ma oblique rifting of the GC appears to have began synchronously resulting in $\sim$ 270 km of opening along its length (Oskin *et al.*, 2001; Oskin and Stock, 2003; Dorsey *et al.*, 2007). However, characteristics of this system vary along strike including mode of deformation, oceanic crustal thickness and width, and amount of magmatism (Lizarralde *et al.*, 2007).

In the southern and central GC continental rupturing is complete. The southern GC consists of the Alarcon, Farallon, and Pescadero basins. The Alarcon basin in the southern Gulf is the only basin to exhibit magnetic lineations characteristic of normal oceanic crust. Here, the onset

of seafloor spreading is estimated to have occurred 2-3 Myr ago and has accommodated approximately 135 km of new oceanic crust with a thickness of 6 km (Lizarralde *et al.*, 2007). Continuing north, the Farallon and Pescadero basins show incipient spreading centers. In the central Gulf, the Guaymas basin continental rupture is estimated to have occurred 6 My ago and $\sim$ 280 km of new oceanic crust has accommodated the extension. Seismic reflection data show that the crust is 6-9 km thick a rapid shallowing of the Moho across the continental oceanic transition characteristic of narrow rifts.

North of the Guaymas basin, the situation is less clear because of thick sediment accumulation (> 7 km) and the lack of deep crustal imaging. On the basis of seismic reflection data and an analysis of synrift sedimentation and magmatism, Martín-Barajas *et al.* (2013) infer that lithospheric rupture across the Tiburon and Tepoca-Altar basins is not complete but that the Upper and Lower Delfin basins have ruptured and that between 40 and 70 km of new hybrid oceanic crust, consisting of gabbro and differentiated igneous rocks intruding the sedimentary cover, has been emplaced. Likewise for the Consag basin González-Escobar *et al.* (2014) reported magmatic intrusions and sills, however magmatic activity is not very extensive.

Crustal structure is imaged in the Salton Trough with refraction and wide-angle seismic reflection data (Fuis *et al.*, 1984; Han *et al.*, 2016). These data reveal an upper crust consisting of thick sediments that grade into metasedimentary rocks and thinned felsic crystalline rocks and a lower crust consisting of underplated gabbros. The crust thins from $\sim$ 30 km in the Coachella Valley to < 20 km in the Imperial Valley. The lower crust is formed through gabbroic underplating (Fuis *et al.*, 1984; Lachenbruch *et al.*, 1985; Han *et al.*, 2016). Basal heat flow is estimated to be $\sim$ 140 mW/m$^2$ (Lachenbruch *et al.*, 1985).

These studies suggest that the NGOC is currently hosting the transition from continental rifting to rupture as thinned continental lithosphere gives way to juvenile oceanic crust presently forming in embryonic spreading centers (Fig 3). In the Wagner basin it is unclear if the lithosphere has ruptured or not.

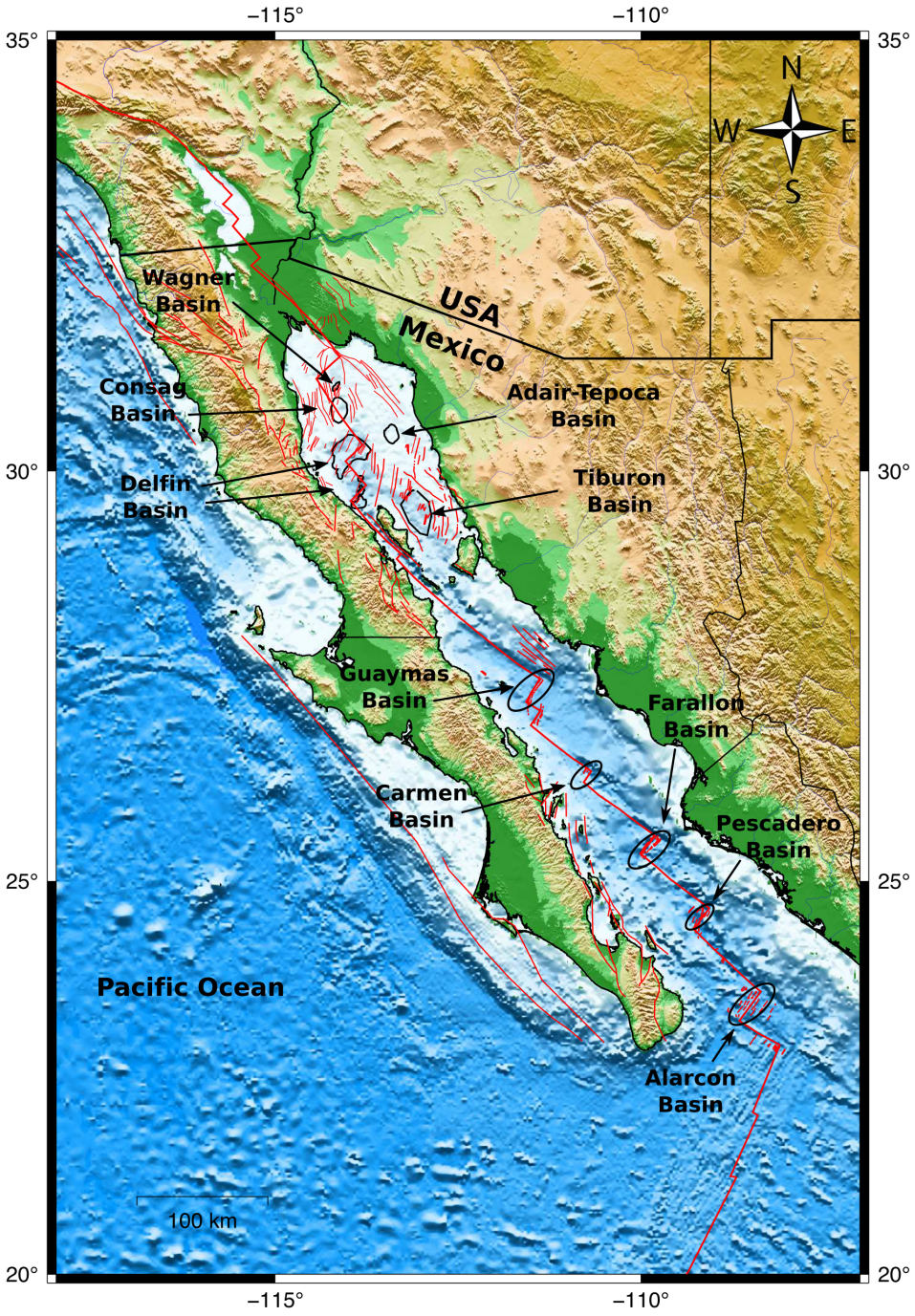


**Figure 3.** Spreading centers, mayor faults and basins in the Gulf of California. The map was generated with GMT (Generic Mapping Tool, Wessel and Smith (1998)) using free Digital Elevation Maps (DEM) from the Geographic Information Network of Alaska (GINA, Lindquist *et al.* (2004))

### 1.4 Wagner basin

In the northern Gulf, there are several tectonically active and inactive rift basins (Aragón-Arreola and Martín-Barajas, 2007; González-Escobar *et al.*, 2009; Martín-Barajas *et al.*, 2013). The group of inactive rifts is located along the eastern part of the Gulf and comprises Adair, Tepoca and Tiburón basins (Figure 4). At $\sim$ 6 Ma, active rifting jumped westward from the now inactive rift basins to form the currently active rift basins that include the Wagner, Consag, Upper Delfin, and Lower Delfin basins. This region is bounded by two major regional right-lateral transform faults. To the northeast is the Cerro Prierto fault with down throw to the west, which established the westerly limit of the Altar basin (Aragón-Arreola and Martín-Barajas, 2007). To the southwest, the Canal de Ballenas Transform fault can be traced north to the Lower Delfin basin. In this area, the Canal de Ballenas Fault splits into several segments forming horsetails structures (Persaud *et al.*, 2003).

The Consag and Wagner basins are the northernmost and shallowest of the active basins in the GC, with maximum depths of $\sim$ 225 m. These basins are connected and controlled by the NNW listric Wagner Fault, which branches out from the Cerro Prieto transform fault. These basins contain a syntectonically deposited sequence that is at least 5 km thick (Pérez-Cruz, 1980; Aragón-Arreola and Martín-Barajas, 2007). Subsidence is controlled by shallow fault arrays rooted in the Wagner Fault, and sediments on it show fault propagation folds (Aragón-Arreola and Martín-Barajas, 2007). In this region, fault scarps are smaller and less common than in other major basins, but the density of faults is higher in the Wagner basin than in the Upper Delfin basin (Persaud *et al.*, 2003). There are many steeply dipping faults and a wide range of fault dips. The structural pattern is asymmetric, with more active faults over a broader region in the SE flank of the basin and a narrower, less active fault zone in the NW side of the basin (Persaud *et al.*, 2003). Wells drilled by the Mexican Oil Company (PEMEX) penetrated $\sim$5 km of Pleistocene sediments, below which the ages where either undetermined or still Pleistocene (Helenes *et al.*, 2009). The thick Pleistocene sediments are faulted downward in the Wagner basin along normal faults with seafloor offsets averaging just a few meters.

The major sources of sediments in the northern GC are the Peninsular Ranges batholith, the Sierra Madre Occidental ignimbrite sequence and the Colorado River basin (Allison, 1964; Andrews, 1991), in addition to a significant eolian supply from the Sonoran Desert (Baba *et al.*, 1991;

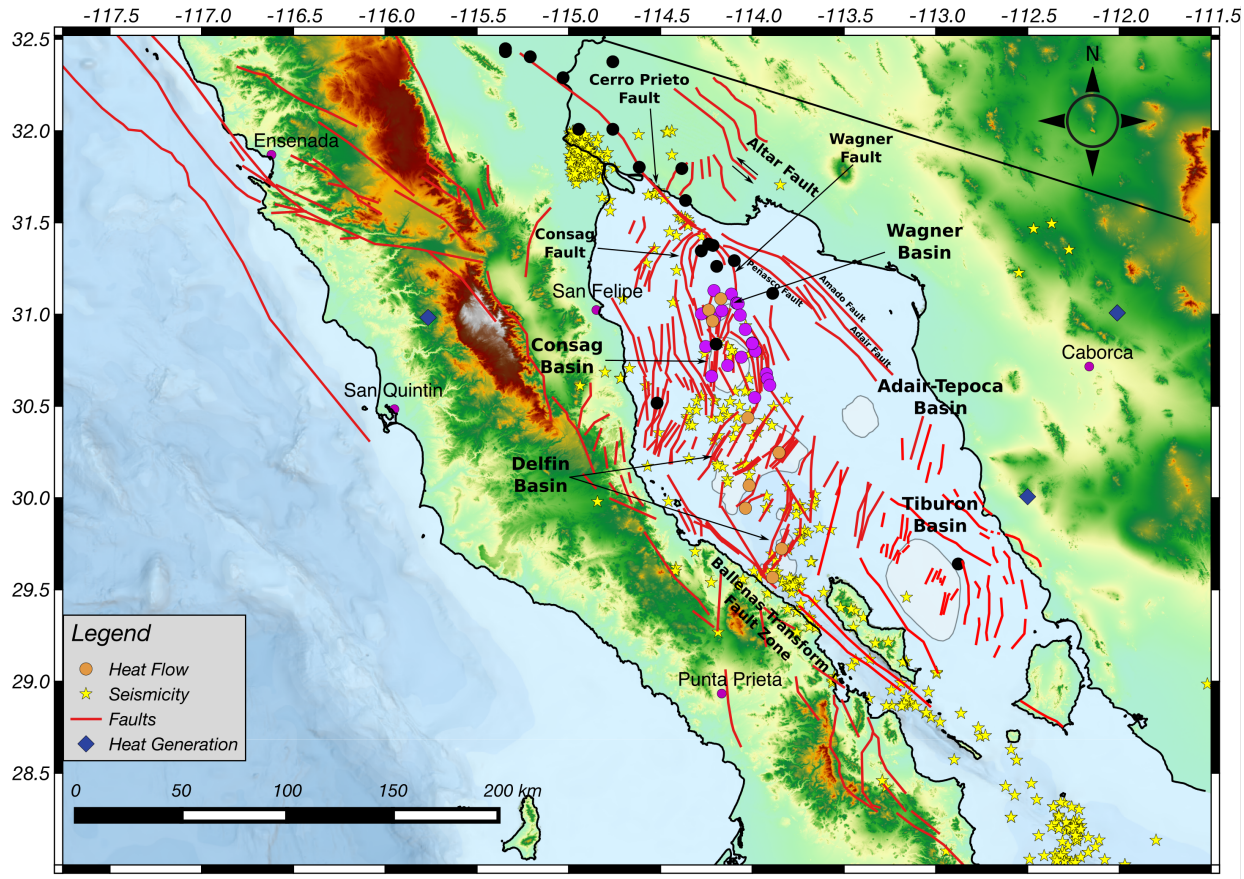


**Figure 4.** Map of the Northern Gulf of California with the rift basin and faults in the region (red lines). Fault traces are from (Persaud *et al.*, 2003; Aragón-Arreola and Martín-Barajas, 2007; González-Escobar *et al.*, 2009; Martín-Barajas *et al.*, 2013). Previous heat flow measurements (circles) from Henyey and Bischoff (1973) (orange), Prol-Ledesma *et al.* (2013) (magenta), Espinoza-Ojeda *et al.* (2017) (black), relocated seismic events (stars, Castro *et al.* (2017)) and radioactive heat generation (squares, Smith (1974)). For more details see the description in the main text. The map was generated with Qgis (QGIS Development Team, 2009) using free digital elevation model from the Shuttle Radar Topography Mission (SRTM), available from the Consortium for Spatial Information (CGIAR-CSI, Jarvis *et al.* (2008))

Carriquiry and Sánchez, 1999) estimate a sedimentation rate of 3.77 cm $yr^1$ (measured in the Upper Delfín basin), and erosion, resuspension and reworking of the Colorado River Delta are between the most important present-day sedimentary processes.

## 1.5 Previous studies

### 1.5.1 Heat flow

The first heat flow data in the NGOC was reported by Henyey and Bischoff (1973). They present 9 heat flow measurements (orange circles in Figure 4) with values from 63 - 92 mW/$m^2$ and 59 - 197 mW/$m^2$ in the Wagner and Delfin basin respectively. Henyey and Bischoff (1973) suggested that the high values in the Delfin basin are associated with near-surface heat sources and that

measurements in the Wagner basin are similar to values found in the Imperial Valley.

Prol-Ledesma *et al.* (2013) report widely spaced heat flow values that range between 16 - 15,436 mW/m$^2$ (magenta circles in Figure 4). Most of the very high values of heat flow are along the Wagner Fault system that cuts the eastern margin of the basin. Prol-Ledesma *et al.* (2013) interpret the high mean heat flow of 1875 mW/m$^2$ as evidence of continental rupture and active seafloor spreading. They envision a system in which hydrothermal circulation is sealed beneath a low permeability sediment cover. However, this interpretation is at odds with the interpretation of distributed deformation between the Cerro Prieto and Canal de Ballenas transform faults (e.g., Persaud *et al.* (2003, 2016)).

Espinoza-Ojeda *et al.* (2017) used geological and thermal information from the Comisión Federal de Electricidad (CFE) and Petróleos Mexicanos (PEMEX) on boreholes mainly located around the Cerro Prieto geothermal field and in the NGOC (black circles in Figure 4). They estimated the thermal gradient from temperature-depth data known as transient boreholes temperatures logs (TBT) or bottom-hole temperature (BHT) and the thermal conductivity from stratigraphic description of the boreholes. Heat flow values offshore vary from 31 - 111 mW/m$^2$ and 36 - 225 mW/m$^2$ onshore.

Unfortunately there exist only 3 (blue squares in Figure 4) reported values of heat generation in the vicinity of the study area (Smith, 1974). This study uses a linear relationship (Equation 9) between the observed heat flow and surface heat generation for measurements in plutonic rocks (Birch *et al.*, 1968; Roy *et al.*, 1968; Lachenbruch, 1968):

$$q = q^* bH \tag{9}$$

where $q$ is the surface heat flow, $q^*$ the reduced heat flow or mantle heat flow, $H$ is the heat generation, determined from the abundances of uranium, thorium and potassium of surface rock samples, and $b$ the parameter that is related to crustal thickness. The two values of heat generation on the mainland are 1 and 2.7 $\mu$W/m$^3$ and 0.18 $\mu$W/m$^3$ on the Baja California Peninsular.

### 1.5.2 Seismic reflection lines and seismic events

Castro *et al.* (2017) present a catalog of accurate epicenter coordinates in the period 2002 - 2014 for the GC using events M > 3.0 (yellow stars in Figure 4). They used body-wave arrivals times from the Broadband Seismological Network of the GC (RESBAN) operated by CICESE. They found that the predominantly mechanisms in the northern part of the Gulf are tensional and that mayor events ($M_s$ > 6.0) are located on the transform faults south of the Delfin basin. Important earthquakes occur on the Canal de Ballenas Transform fault.

Seismic events (M > 0.0) for the northern Gulf of California for a time period between 1975 -

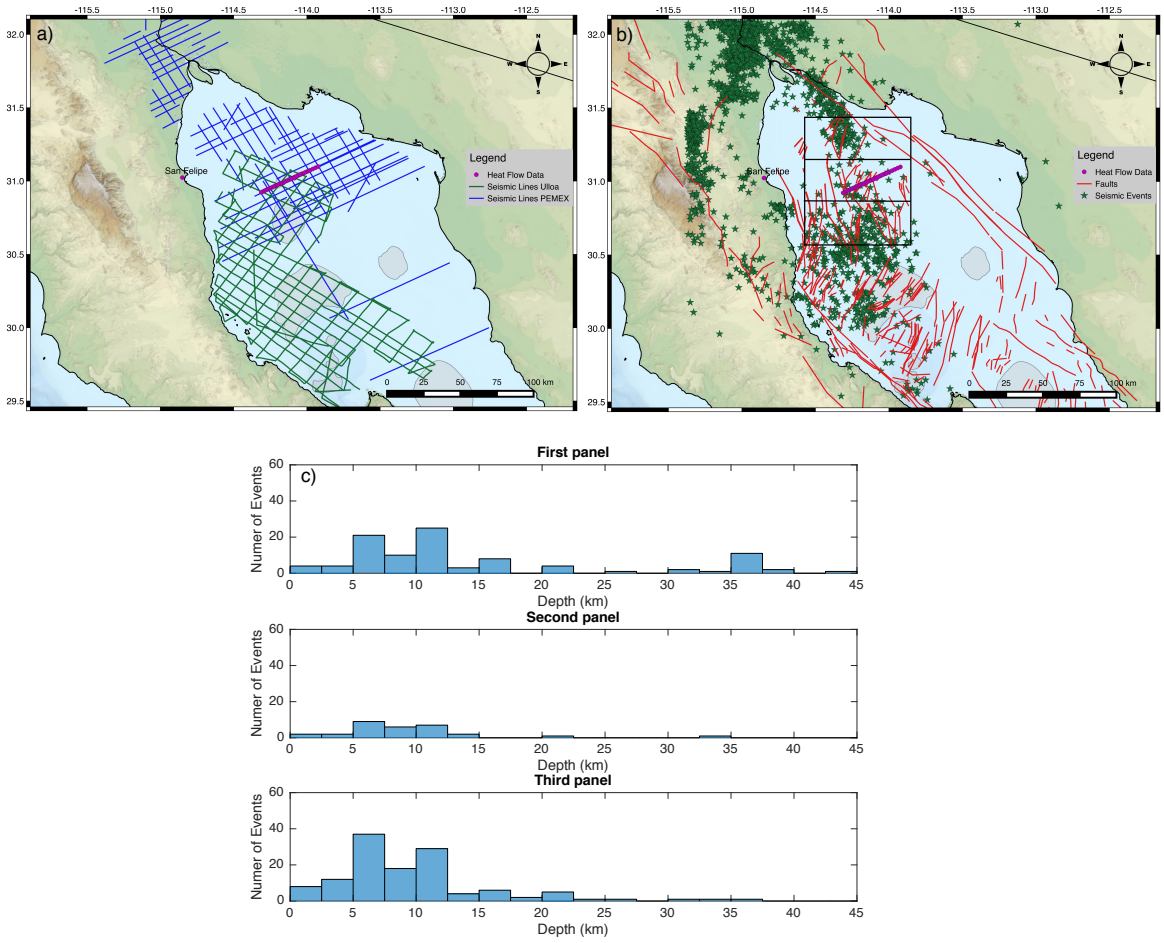


**Figure 5.** a) Map of the Northern Gulf of California. Blue lines are the processed and interpreted seismic lines from PEMEX. Green lines are seismic profiles collected by CICESE. b)Map of the Northern Gulf of California with rift basins and faults (red lines). Fault traces are from (Persaud *et al.*, 2003; Aragón-Arreola and Martín-Barajas, 2007; González-Escobar *et al.*, 2009; Martín-Barajas *et al.*, 2013). The stars are locations for seismic events of the Red Sísmica del Noroeste de México. c) Histograms showing the depth of seismic events for the three panels in Figure 5b. For more details see the description in the main text. The map was generated with Qgis (QGIS Development Team, 2009) using free Digital Elevation Maps (DEM) from the Geographic Information Network of Alaska (GINA, Lindquist *et al.* (2004))

2016 from the Red Sísmica del Noroeste de México (RESNOM, 2015) are represented as green stars in Figure 5b. The data show that earthquakes are mostly concentrated on the western part especially in the Cerro Prieto area, along the Cerro Prieto Fault, Consag and Delfín basins. On the other hand, the eastern part lacks seismic events, which indicates less active faults or stable sliding. The same statement is valid for the NW part of the Wagner basin. Figure 5c shows the number of events against depth. The panels correspond to the three rectangles in Figure 5b. Depth of events are not relocated and therefore spatial errors can be very large. In summary the transition between the brittle and ductile part of the crust is $\sim$ 8-10 km.

The reflection seismic group at CICESE processed and interpreted profiles (blue lines in Fig. 5a) taken in the 70's and 80's by PEMEX (Aragón-Arreola, 2006; Aguilar-Campos, 2007; Aragón-Arreola and Martín-Barajas, 2007; Hernández-Pérez, 2008; Mar-Hernández, 2009; González-Escobar *et al.*, 2009; Sojo-Amezquita, 2012; Chanes-Martínez, 2012; Sánchez-García, 2013; Martín-Barajas *et al.*, 2013; Vega-Saucedo, 2014; Montoya-Valenzuela, 2014). Furthermore 3500 km of seismic reflection data were collected in May-June 1999 aboard CICESE's 28 m long research vessel B/O Francisco de Ulloa (Persaud *et al.*, 2003; Persaud, 2004; Hurtado-Brito, 2012).

Persaud *et al.* (2003) present detailed images of faulting and identified 12 volcanic knolls from multichannel seismic reflection data and sonobuoy refraction data, collected in the NGOC. They found a complex network of dense oblique-normal faults and that the basement consist of a mixture between igneous and sedimentary material. Based on their results they suggest that seafloor spreading will first occur in the Lower Delfín basin and that the transition from continental rupture to seafloor spreading is delayed as a consequence of a broad shear zone beneath the thick sediments.

Aragón-Arreola and Martín-Barajas (2007) found, based on seismic reflection data from PEMEX collected in 1978 and 1979, that the eastern part of the NGOC contains two inactive basins (Tepoc-Adair and Tiburon) and an active western part including the Wagner, Consag, Upper and Lower Delfín basins. They suggest a westward migration of strain during middle to late Pliocene and that the inactive faulting is present along the entire eastern part, while active faulting is located on the western part of the GC.

González-Escobar *et al.* (2009) characterized the extension and the geometry of the Wagner

basin using multichannel seismic reflection data collected in 1979 and 1980 by PEMEX. They identified three mayor boundaries and calculated an area of $\sim$ 1330 km$^2$ of the basin. (Figure 4). The western boundary is marked by the Consag normal fault, the eastern by the Wagner normal fault, which intersects the Cerro Prieto strike slip fault, marking the northeast boundary of the basin.

Several minor structures in the northern Gulf are identified and interpreted from seismic data collected by PEMEX and published as Master and PhD thesis.

### 1.5.3 Bathymetry

The first bathymetry survey was taken between 1994 and 1997 using Ocean Data Equipment continuous depth recorder and GPS on board CICESE's research vessel B/O Francisco de Ulloa (Persaud *et al.*, 2003). They used the traces and interpolated the data points to create a grid. A detailed contour map with geological interpretations around and to the north of the Wagner basin is

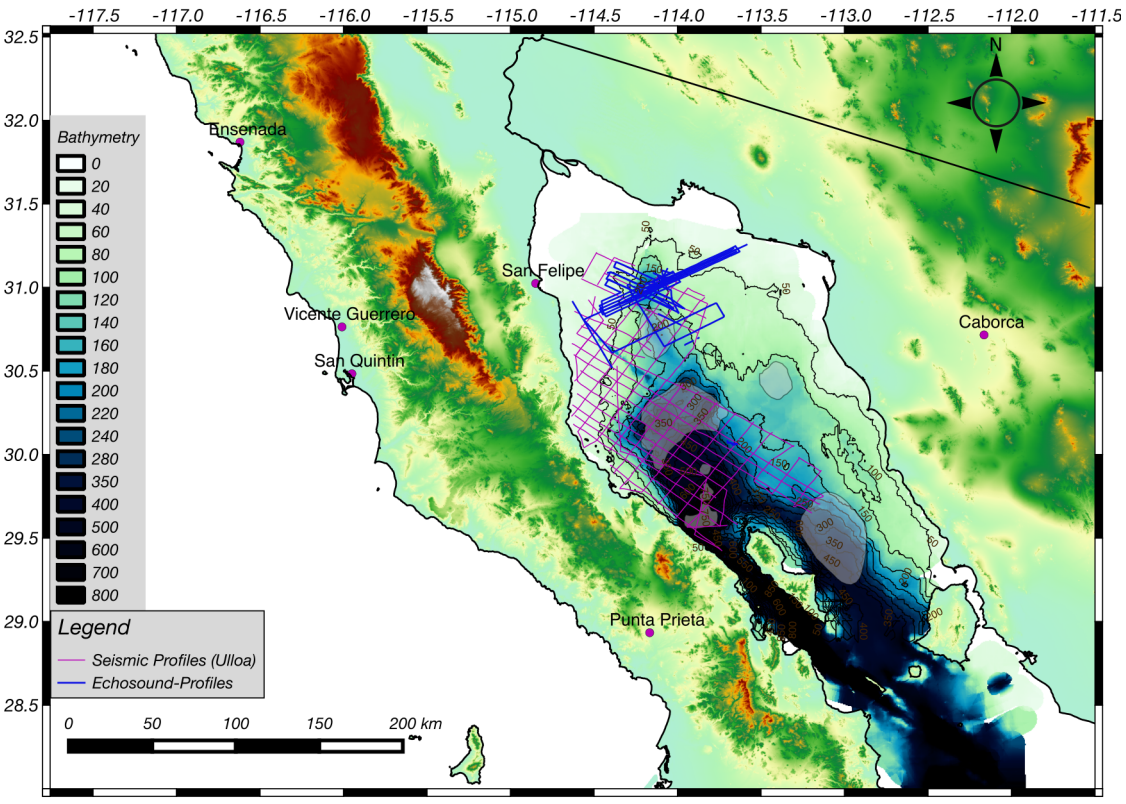


**Figure 6.** Bathymetry of the Northern Gulf of California with contours at intervals of 50 m. The lines in magenta represented the data collected between 1994 - 1997 (Persaud *et al.*, 2003) and data collected in 2015 (Díaz-Méndez *et al.*, 2015).

presented by (Alvarez *et al.*, 2009). During the heat flow survey cruise in May 2015 with CICESE's R/V Alpha Helix (Díaz-Méndez *et al.*, 2015) used the profiles from the water echo sounder to interpolate the data points. Figure 6 shows the compiled processed and corrected grid for the NGOC. In addition traces from the first survey (magenta) and from the second survey in 2015 (blue) are plotted. From the Rio Colorado delta to the northern edge of the Wagner basin water depth increase from 10 m to 40 m. The Wagner, Consag and Adair-Tepoca basin are shallow with depth not exceeding 250 m. Water depth increases gradually southwestwards with depth between 700 - 800 m in the Canal de las Ballenas, whereas the eastern part stays shallow.

### 1.5.4 Magnetic and gravity data

(Klitgord *et al.*, 1974) conducted a closely spaced magnetic anomaly survey in the northern and central part of the Gulf on board the research vessel Velero IV in 1970 and 1971. The results show an absence of magnetic anomalies for the Guaymas, Delfin and Wagner basin attributed to the high sedimentation rate, which inhibits the magnetization of pillow basalts (Larson *et al.*, 1972). Levi and Riddihough (1986) proposed that the magnetized minerals are transported during hydrothermal circulation underneath a thick layer of sediments. This comparatively closed circulation within a relatively impermeable sediment layer causes continuous leaching of remanence-carrying magnetic minerals. This process might explain the magnetically "quite zones" as they are found in the Gulf of California, Gulf of Aden and the northern Red Sea.

Sanchez-Zamora *et al.* (1991) collected magnetic data in the NGOC between 1981 and 1984 to determine the depth of the magnetic source. The deepest source is assumed to be the Curie-point isotherm. The average depths to the bottom of the magnetic source is about 11.5 km above sea level. Sanchez-Zamora *et al.* (1991) computed an average heat flow in the central part of the northern Gulf of 114 mW/m$^2$ from an average thermal gradient of 51.8°C/km, assuming a Curie-point temperature of 500°C and an assumed thermal conductivity of 2.2 W/m°C.

Quantitative interpretation of gravity data from Pérez-Cruz (1980) showed, the existence of a plutonic body with density between 2.6 - 2.7 g/cm$^3$ under sediments with a density of 2.3 g/cm$^3$.

## 1.6 Goals

This study is part of the intensive geothermal exploration of the marine basins and the continental shelf in the Gulf of California to investigate the geothermal potential in the region. During the campaign, active and passive electromagnetic, seismic reflection and refraction, magnetometry, monohaz and multihaz bathymetry, hydrogeochemistry and heat flow data as well as sediment and rock samples will be acquired. The main object is to map the distribution of the heat flow and the geothermal gradient in areas of interest of the rift system in the GC.

The motivation of this work is to understand the thermal distribution and conductivity of the thinned lithosphere of the NGOC, in particular to quantify the geothermal heat budget of the Wagner basin. We have carried out an analysis of the available data in order to plan the acquisition and processing of new heat flow measurements. We propose a new methodology to calculate shallow heat flow measurements, affected by bottom water temperature variation. Furthermore we constructed a thermal model constrained by other geophysical and geological parameters along the study area.

# Chapter 2. Acquisition and analysis of marine heat flow

## 2.1 Marine heat flow probe

The heat flow probe (Figure 7) is an instrument to determine heat flow (heat flux density) by measuring thermal gradients and *in-situ* thermal conductivities of marine sediments. Furthermore, parameters like the sediments thermal diffusivity and heat capacity can be determined. The instrument used in this work was acquired from FIELAX Gesellschaft für wissenschaftliche Datenverarbeitung mbH, a German company located in Bremerhaven (FIELAX, 2017). The company offers operation and production of marine technology, processing scientific datasets and customized software development.

With the increasing importance in the last decades of geothermal marine heat flow measurements, a number of significant questions have arisen in marine geophysics: what processes occurring near the surface of sediments and the oceanic crust drive the the pore water and hydrothermal circulation at the continental margins and flanks of spreading centers (Stein and Stein, 1994; Hutnak and Fisher, 2007). To address these new questions there has been an increase for high resolution heat flow data acquisition and processing techniques over the last decades.

The acquisition part has evolved to the construction of robust violin-type heat probe instruments following the prototype from Lister (briefly described in Hyndman *et al.*, 1979; Davis *et al.*, 1980). Developments in electronics further increased temperature resolution to 1mK and allowed higher storage capacity which led to more sensors along the probe. Another development step from the first *in situ* method to determine thermal conductivity using a line heater along with temperature sensor in the same probe was developed by Von Herzen *et al.* (1982); Jemsek *et al.* (1985). However, the consumption of too much energy by using a continuous heating wire was a disadvantage. Lister (1979) proposed an alternative method to the continuous heating, in which a short calibrated heat pulse (1kJ/m) is applied to a cylindrical probe. The decay of the pulse is used to determine the *in situ* thermal conductivity. These new developments allow multipenetration deployments (pogo-style) over longer time periods (24 h). The main features of the used heat flow probe in this study are:

- 6 m penetration depth, rated for 6000 m water depth,
- Great stability with respect to mechanical strain for use in critical areas where carbonate crusts or gas hydrates may occur,
- Robust design and steel construction for high durability,
- Weight stand for optional additional weights,
- Measurement relative resolution is better than 1 mK,
- Accuracy better than 2 mK after calibration,
- 22 temperature sensors along 6 m sensor string,
- 22 data channels at a sampling rate of 1 Hz,
- Real-time data transmission and communication at a rate of 2400 baud through single conductor deep-sea cable,
- Adjustable sampling frequency (max. 1 Hz),
- Autonomous measurement and data storage for up to three days of operation if no single conductor deep-sea cable is available,
- Seafloor approach and penetration control with integrated tilt, acceleration and pressure sensors,
- Pogo-style-operation, i.e. extended profiles can be acquired whilst minimizing ship charter time.

Figure 7 A shows the heat flow probe consisting of a 15 mm in diameter hydraulic steel tube (string sensor) mounted on the 6 m long strength member. The base plate connects the lower strength member with the 3 steel tubes, housing the data acquisition and power unit for autonomous operation. A total of 40 pieces of extra weight, each of 50 kg can be added to the probe if necessary. The 1000 kg stainless steel probe assembled and ready for deployment on board the ALPHA HELIX R/V and operation position is shown in Figure 7 B, C. Both the data acquisition (Fig. 8 B, C) and the power supply unit (Fig. 8 A) are built-in underwater pressure housing cylindrical tubes. The design is identical, only the lids have different sensors and connectors. The housings are made of seamless titanium for operation depth down to 6000 m. The power supply unit is connected with a Subconn BH2F connector for the power supply cable to the data acquisition unit and supplies the power for the heat pulse. Inside the power supply housing are four MATE-N-LOC connectors for fast recharge of the battery pack.

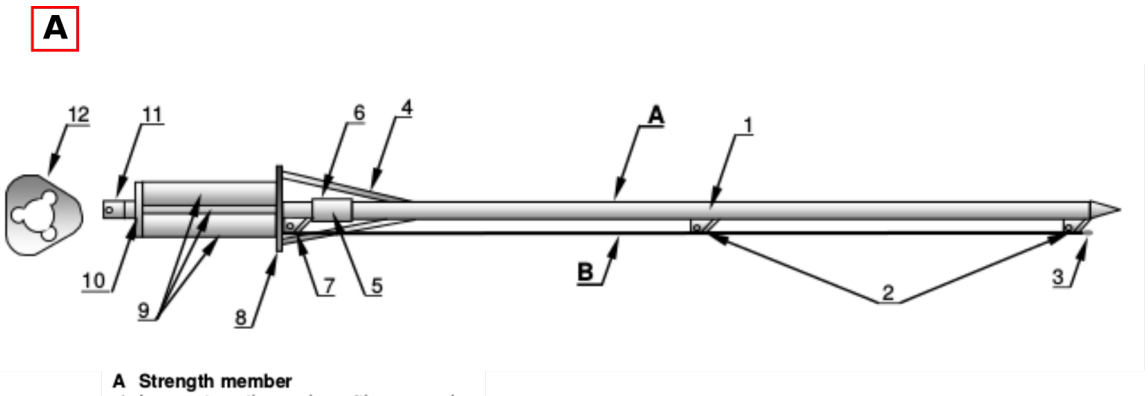


**A Strength member**
1 Lower strength member with cone end
2 Lower clamps (2x)
3 Counter nut and cap nut
4 Cable deflectors (3x)
5 Sleeve socket
6 Bolt
7 Upper clamp
8 Base plate
9 Steel tubes (3x)
10 Cover plate
11 Upper strength member
12 Extra weight (max. 40x)

**B Sensorstring**
22 Thermistors (NTC1 – NTC22)
Heating wire
Connectors (3x Subconn MCIL16M)

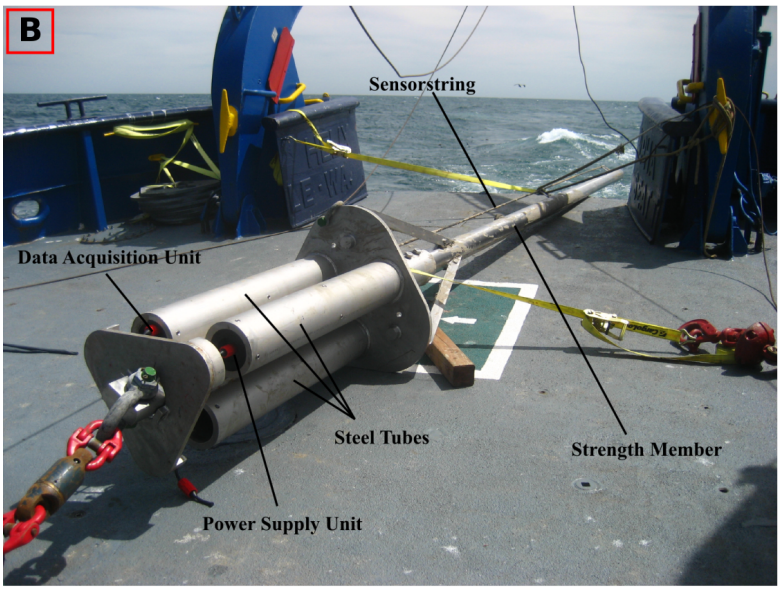


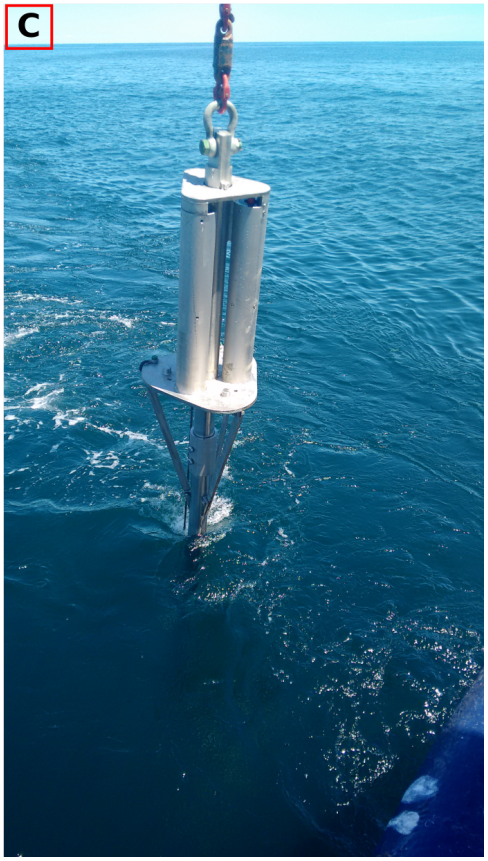


**Figure 7.** Fielax marine heat flow probe device. A) Schematic picture of the probe with data acquisition and power supply unit (Modified from FIELAX (2017)). B) Strength member on deck the ALPHA HELIX R/V. C) Deployed probe in the water before lowering to the seafloor.

The data acquisition unit contains the following components:

- Data logger SST memory probe,
- 32 measuring channels,
- Precision temperature sensor PT100,
- 22 data channels at a sampling rate of 1 Hz,
- Depth measurement up to 6000 m,
- Determination of heat pulse energy,
- Supervision of all battery load conditions,
- 2 axis tilt and vertical acceleration measurement,
- Bidirectional FSK telemetry,
- RS232 interface,
- Internal 1.5V Alkaline battery for logger supply in autonomous mode.

All the parts of the data acquisition unit, in contact with the seawater are made of stainless titanium. The electromechanical parts are all located above the top lid and next to the internal battery (Figure 8 B). The internal battery is only a backup system to ensure the data storage in case that the external power fails. The bottom lid is equipped with three colored 16-pole bulkhead connectors SubConn MCIL16F titanium for connection of the data acquisition unit with the sensor string. Outside the top lid of the data logger are the temperature sensor PT100 (**a**), a pressure sensor (**b**), a reed contact for power switching (**c**), the SubConn BH2M connector for power supply via battery pack (**d**) and the SubConn MCBH5M connector for data transfer (**e**).

The sensor string is a 15 mm in diameter hydraulic steel tube containing 22 temperature, named NTC1 - NTC22, sensors and a heating wire for the heat pulse (Figure 9 A). The steel tube is filled with oil to guarantee thermal coupling between the sensor strings and the cylindrical probe. In addition, the oil should compensate the water pressure. The thermistors (Figure 9 B) are constructed for a temperature range between -2°C - 60°C with a resolution of 1 mK and an accuracy of 2 mK. The thermistors are equally spaced 26 cm apart with a overall length of 5.72 m. The connection to the data logger is via three Subconn MCIL16F connectors. Each thermistor requires 2 wires and the locking sleeves have the same color as their opposites mates on the data acquisition unit. The black sleeves contains the wires for thermistor NTC1 to NTC8, the blue for thermistor NTC9

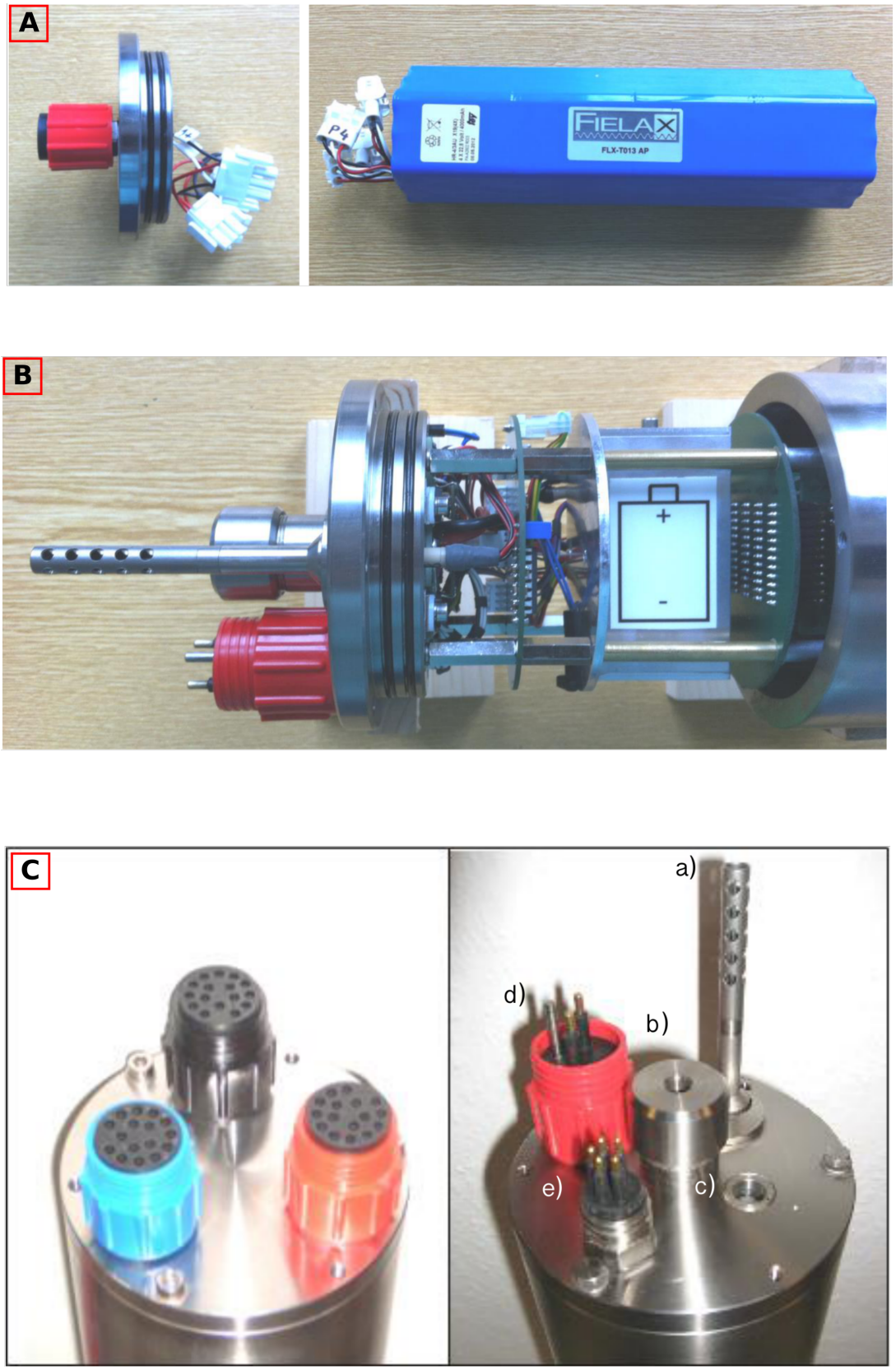


**Figure 8.** A) Power supply unit with lid for the power supply cable. B) Data acquisition unit with data logger and internal battery. C) Lower (left) and upper (right) lid of the data acquisition unit. Modified from FIELAX (2017).

to NTC16 and the red NTC17 to NTC 22. Additionally the red connector contains 4 wires for the heat current.

The data acquisition unit offers four configurable data storage modes:

- Time mode,
- Increment mode,
- Continuous mode,
- Event mode (Section 2.2.1).

and three online modes, which will not be further discussed in this work:

- FSK (for single conductor cable) mode,
- RS232 online mode,

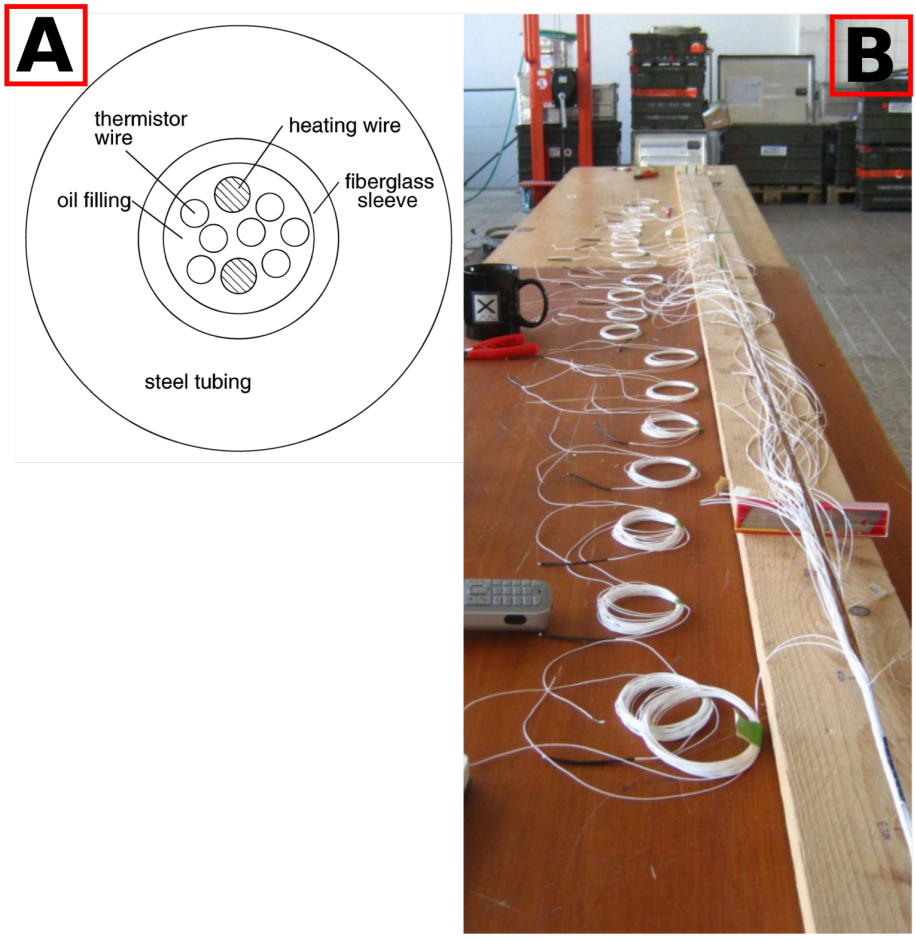


**Figure 9.** A) Cross-section of a sensor string with thermistor and heating wires (Hartmann and Villinger, 2002). B) Assembling thermistor wires.

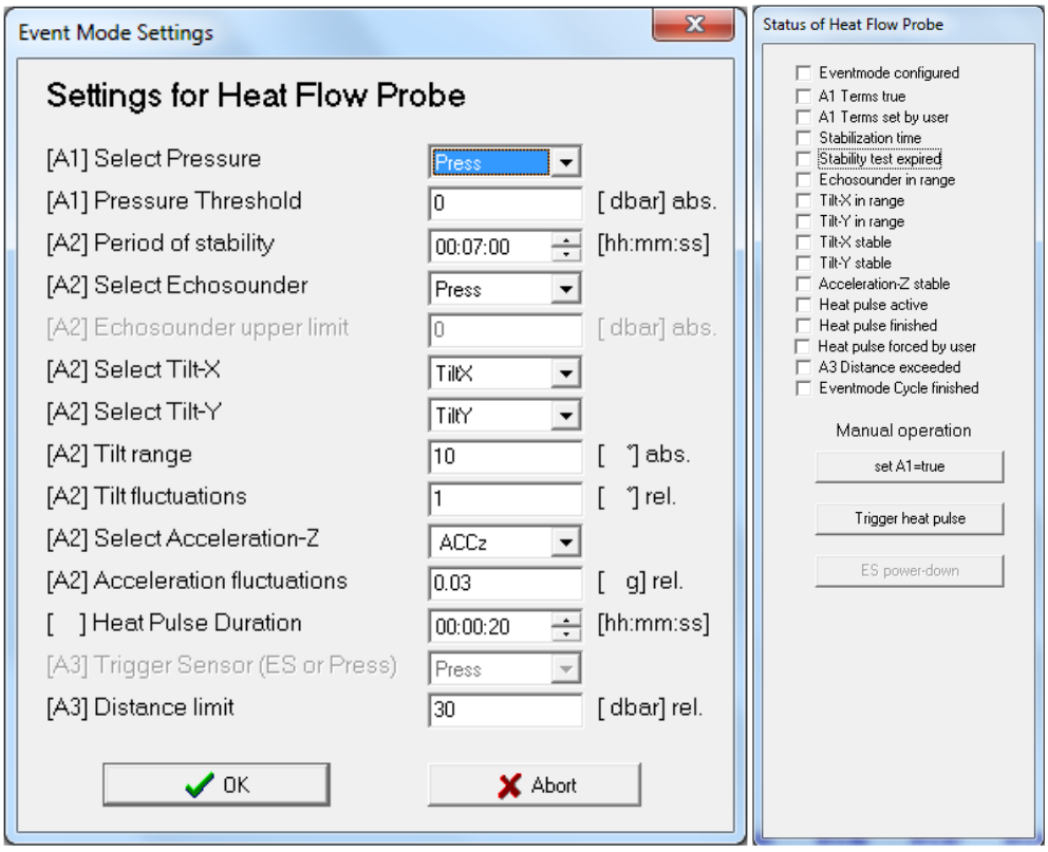


**Figure 10.** (left) Event mode setting window with example values for the limits and stability criteria. (right) Status window for online measurement.

- Command mode.

In this work, only the Event mode will be discussed in detail.

## 2.2 Marine heat flow measurement

### 2.2.1 Configuring the memory probe

Before a measurement can be carried out, the probe needs to be configured. Configuration as well as the retrieval of the data is accomplished by the SST - SDA software that comes with the data acquisition unit from Sea & Sun Technology. The event mode is used to select the parameters for triggering the heat pulse. There are three different groups of criteria **A1**, **A2** and **A3** (Fig. 10), which have to met in order to start, pass and finish one event mode cycle.

**A1** is a threshold criterion where the probe has to pass a certain water depth to activate the

configured event mode and start recording data. The water depth is defined as the pressure value in dbar.

**A2** is the criterion of stability after the probe penetrates the seafloor. This criterion is important to get high quality measurements from the sediment and avoid unnecessary energy loss during the heat pulse. If these criteria are met within the defined period of stability (7 min) the heat pulse is released for the configured period of time (20 s). Both the threshold criteria that activates the probe and the stability criteria for firing the heat pulse need to be checked as follows:

- orientation limits (TiltX, TiltY) in degrees as positive value e.g. for -10°<Tilt<10° enter 10°,
- orientation stability (fluctuations of TiltX, TiltY and AccZ),
- bottom distance (penetration depth),
- position stability (vertical acceleration AccZ).

**A3** is a threshold criterion as well. After the heat pulse is released and dissipated the probe has to be pulled out of the sediment and raised to the configured distance limit in order to start a new event mode cycle.

In case that the probe works online, the operator can check the stability and criteria in-situ and halt a measurement.

Figure 11 shows the procedure for a "Pogo Style" measurement using the different criteria during a measurement. In this case the event mode allows to make several measurements without retrieving the probe from the water. Figure 12 shows the workflow of a heat flow measurement, beginning with the configuration of the probe, followed by the measurement, quality check and ending with the heat flow value.

### 2.2.2 Stages of measuring process

To illustrate the steps involved in the measuring of marine heat flow, a typical temperature - time series is shown in Figure 13. After the probe is lowered to the seafloor (A), the temperature increases due to the friction between the sediment and the probe (B). The frictional decay (C) is

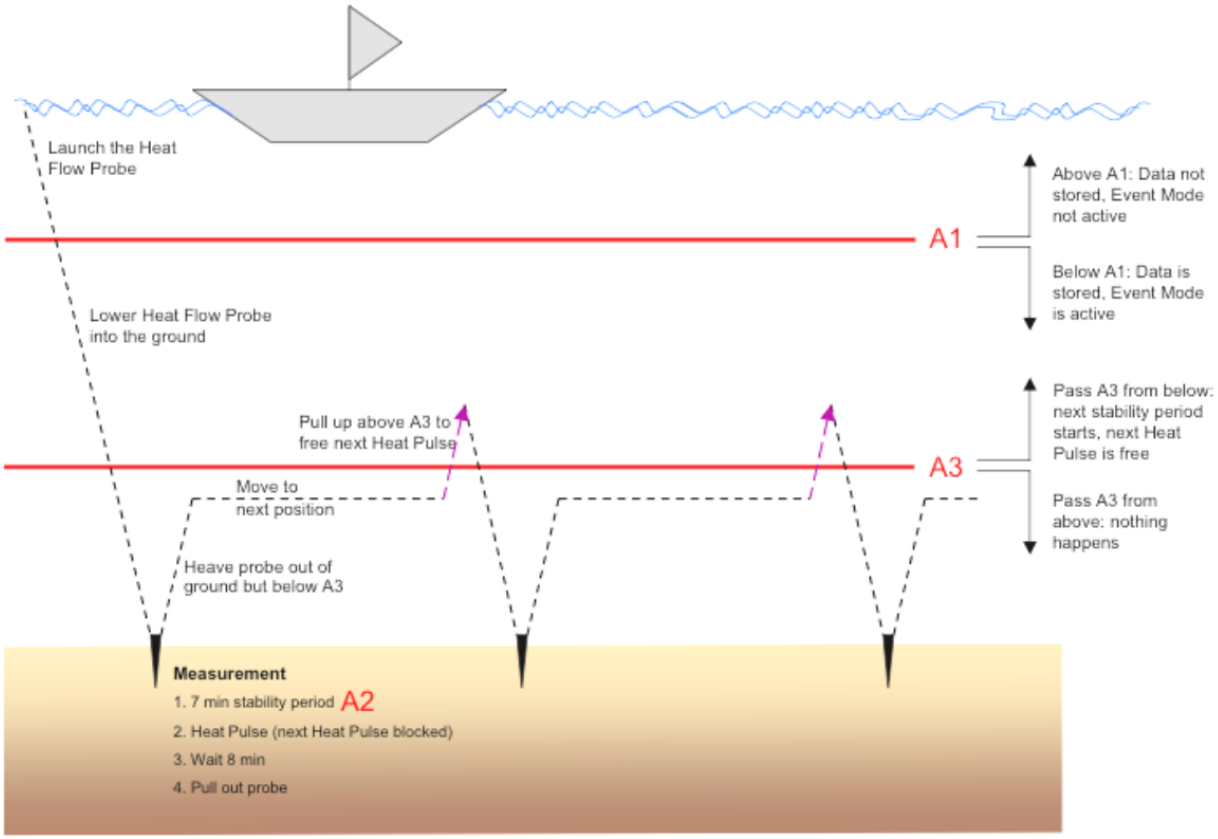


**Figure 11.** Concept of the "Pogo Style" measurements with the Heat flow probe with the different criteria are used for different phase of the measuring process (FIELAX, 2017).

used to determine the equilibrium temperatures and to compute the thermal gradient by fitting a cylindrical decay curve over a 10 min time period and extrapolating to infinite time (Bullard, 1954b; Carslaw and Jaeger, 1959).

After the stability criteria are met, a short induced heat pulse (20s) is fired (D), followed by a 20 minute decay (E) to calculate the *in situ* thermal conductivity. The measurement is concluded by pulling out the probe from the sediment (F). Heat flow is calculated by the product of the linear thermal gradient, indicating steady state conductive heat transport and the thermal conductivity over the same interval also known as Fourier's law (Equation 3).

## 2.3 Data analysis

The Analysis software, part of the FIELAX system is developed in MATLAB© and is a collection of tools for processing and imaging the acquired heat flow data. The software is divided into

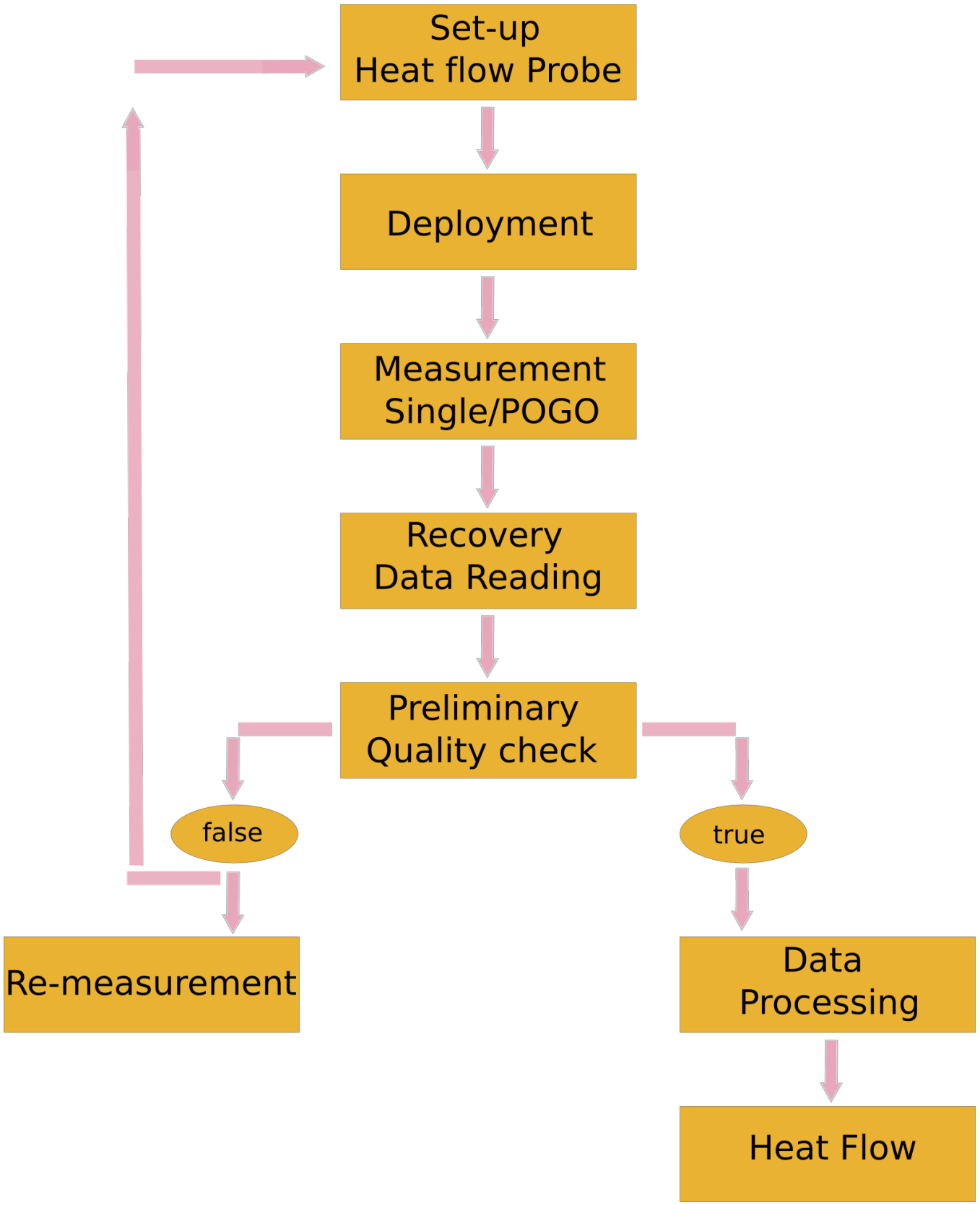


**Figure 12.** Workflow diagram of a heat flow measurement.

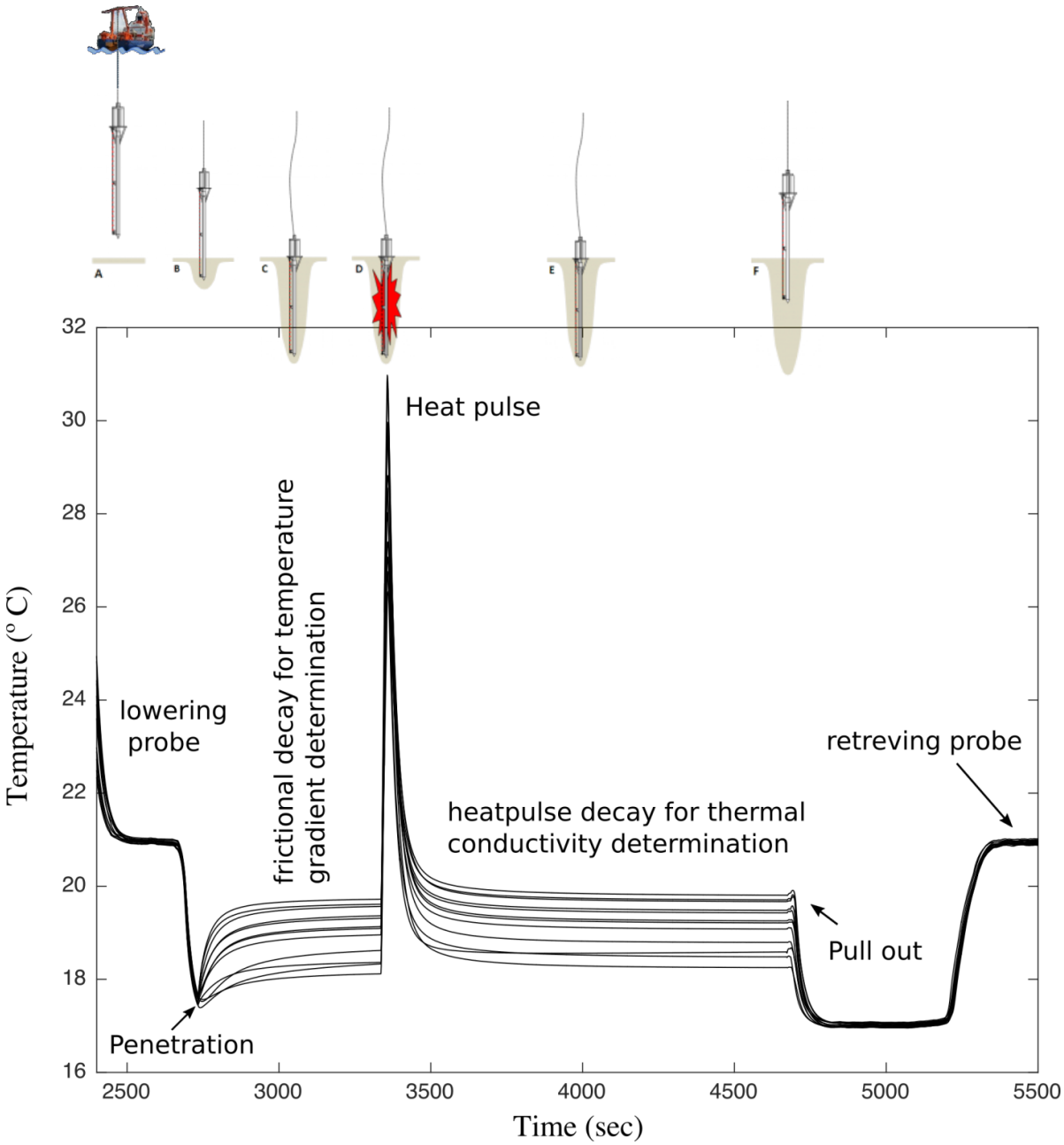


**Figure 13.** Typical temperature vs. time series for a marine heat flow measurement using a FIELAX heat flow probe with 22 thermistors.

two main tools called GHF-Tools (Giant Heat Flow Tools) and T2C (Temperature to Conductivity). GHF-Tools manage the raw data of a measurement, whereas the T2C calculates the depth dependent thermal properties (*in-situ* temperatures, thermal conductivities and diffusivities) and flow estimation. The inversion procedure is based on the algorithm that Villinger and Davis (1987) and Hartmann and Villinger (2002) developed at the University of Bremen and will be explained in detail below (Section 2.3.2). The data that is used to show the different tools and plots in below sections were collected on board ALPHA HELIX R/V in May 2015.

### 2.3.1 Raw data and processing files

The *TOB file* (Figure 14) contains the raw, plain-text data acquired by the probe at each station. One station can contain several penetrations (Pogo Style). The file is downloaded from the data acquisition unit. The file header contains the electronics ID, station name, longitude, latitude and operator. The structure of the TOB-file is seen in Figure 14. The collected parameters are the following:

- dataset number,
- Vbatt [Volt] = voltage of the internal battery,
- Press [dbar] = pressure,
- Temp [°C] = temperature of the PT100,
- Vheat [Volt] = voltage of the heat pulse,
- Iheat [A] = current of the heat pulse,
- Tilt [°] = tilt along the x and y direction,
- ACCz [g] = acceleration,
- NTC1 - NTC22 [°C] = thermistor temperatures,
- Vaccu [Volt] = voltage of the power supply unit,
- IntDt [Time] = date and time.

Figure 15 shows a plot of TOB-file from a multipenetration station. The top plot shows temperature vs. time (Figure 13) series for three penetrations. The different colors represent the individual

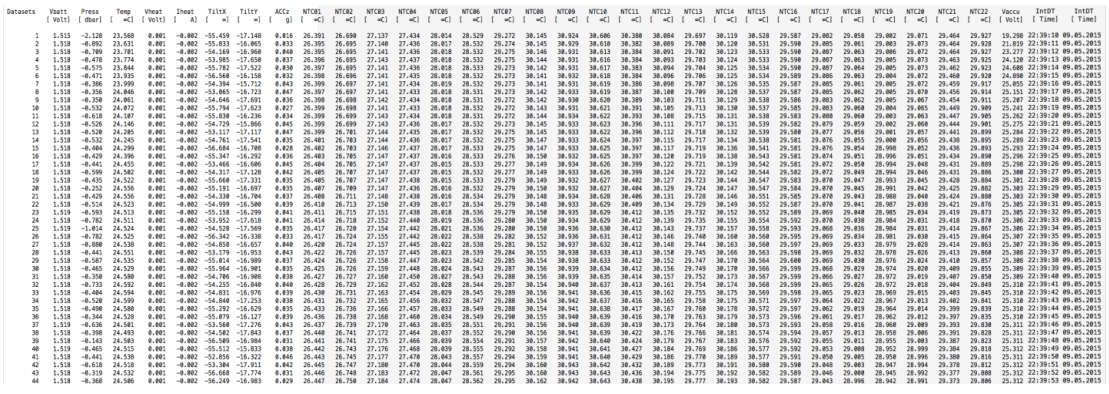

| Datasets | Vbatt [ Volt] | Press [ dbar] | Temp [ °C] | Vheat [ Volt] | Iheat [ A] | TiltX [ °] | TiltY [ °] | ACCz [ g] | NTC01 [ °C] | NTC02 [ °C] | NTC03 [ °C] | NTC04 [ °C] | NTC05 [ °C] | NTC06 [ °C] | NTC07 [ °C] | NTC08 [ °C] | NTC09 [ °C] | NTC10 [ °C] | NTC11 [ °C] | NTC12 [ °C] | NTC13 [ °C] | NTC14 [ °C] | NTC15 [ °C] | NTC16 [ °C] | NTC17 [ °C] | NTC18 [ °C] | NTC19 [ °C] | NTC20 [ °C] | NTC21 [ °C] | NTC22 [ °C] | Vaccu [ Volt] | IntDT [ Time] | IntDT [ Time] |
|---|---|---|---|---|---|---|---|---|---|---|---|---|---|---|---|---|---|---|---|---|---|---|---|---|---|---|---|---|---|---|---|---|
| 1 | 1.515 | -2.128 | 23.560 | 0.001 | -0.002 | -55.459 | -17.148 | 0.016 | 26.391 | 26.690 | 27.137 | 27.434 | 28.014 | 28.529 | 29.272 | 30.145 | 30.924 | 30.606 | 30.388 | 30.084 | 29.697 | 30.119 | 30.528 | 29.587 | 29.802 | 29.858 | 29.802 | 29.871 | 29.464 | 29.927 | 10.298 | 22:39:10 09.05.2015 |
| 2 | 1.518 | -0.092 | 23.631 | 0.001 | -0.002 | -55.833 | -16.805 | 0.033 | 26.395 | 26.695 | 27.140 | 27.436 | 28.017 | 28.532 | 29.274 | 30.145 | 30.929 | 30.610 | 30.382 | 30.089 | 29.700 | 30.120 | 30.531 | 29.590 | 29.805 | 29.861 | 29.803 | 29.873 | 29.464 | 29.928 | 21.819 | 22:39:11 09.05.2015 |
| 3 | 1.518 | -0.709 | 23.701 | 0.001 | -0.002 | -54.169 | -16.960 | 0.040 | 26.395 | 26.695 | 27.141 | 27.436 | 28.018 | 28.532 | 29.275 | 30.146 | 30.931 | 30.613 | 30.384 | 30.091 | 29.702 | 30.123 | 30.533 | 29.590 | 29.807 | 29.863 | 29.806 | 29.872 | 29.464 | 29.927 | 23.277 | 22:39:12 09.05.2015 |
| 4 | 1.518 | -0.478 | 23.774 | 0.001 | -0.002 | -53.985 | -17.650 | 0.037 | 26.396 | 26.695 | 27.143 | 27.437 | 28.018 | 28.532 | 29.275 | 30.144 | 30.931 | 30.616 | 30.384 | 30.093 | 29.703 | 30.124 | 30.533 | 29.590 | 29.807 | 29.863 | 29.805 | 29.873 | 29.463 | 29.925 | 24.128 | 22:39:13 09.05.2015 |
| 5 | 1.518 | -0.575 | 23.844 | 0.001 | -0.002 | -55.782 | -17.522 | 0.030 | 26.397 | 26.695 | 27.141 | 27.436 | 28.018 | 28.533 | 29.273 | 30.142 | 30.931 | 30.617 | 30.383 | 30.094 | 29.704 | 30.125 | 30.534 | 29.590 | 29.807 | 29.864 | 29.805 | 29.873 | 29.462 | 29.923 | 24.600 | 22:39:14 09.05.2015 |
| 6 | 1.518 | -0.471 | 23.935 | 0.001 | -0.002 | -56.560 | -16.150 | 0.032 | 26.398 | 26.696 | 27.141 | 27.435 | 28.018 | 28.532 | 29.273 | 30.141 | 30.932 | 30.618 | 30.384 | 30.096 | 29.706 | 30.125 | 30.534 | 29.589 | 29.806 | 29.863 | 29.804 | 29.872 | 29.468 | 29.928 | 24.890 | 22:39:15 09.05.2015 |
| 7 | 1.518 | -0.306 | 23.999 | 0.001 | -0.002 | -54.394 | -15.712 | 0.043 | 26.399 | 26.697 | 27.141 | 27.436 | 28.019 | 28.532 | 29.273 | 30.141 | 30.931 | 30.619 | 30.386 | 30.098 | 29.707 | 30.126 | 30.535 | 29.587 | 29.805 | 29.861 | 29.805 | 29.872 | 29.459 | 29.917 | 25.055 | 22:39:16 09.05.2015 |
| 8 | 1.518 | -0.356 | 24.046 | 0.001 | -0.002 | -53.065 | -16.723 | 0.047 | 26.397 | 26.697 | 27.141 | 27.433 | 28.018 | 28.531 | 29.273 | 30.142 | 30.933 | 30.619 | 30.387 | 30.100 | 29.709 | 30.128 | 30.537 | 29.587 | 29.805 | 29.862 | 29.805 | 29.870 | 29.456 | 29.914 | 25.151 | 22:39:17 09.05.2015 |
| 9 | 1.518 | -0.350 | 24.081 | 0.001 | -0.002 | -54.646 | -17.691 | 0.036 | 26.398 | 26.698 | 27.142 | 27.434 | 28.018 | 28.531 | 29.272 | 30.142 | 30.930 | 30.620 | 30.389 | 30.103 | 29.711 | 30.129 | 30.538 | 29.586 | 29.803 | 29.862 | 29.805 | 29.867 | 29.454 | 29.911 | 25.207 | 22:39:18 09.05.2015 |
| 10 | 1.518 | -0.532 | 24.072 | 0.001 | -0.002 | -55.784 | -17.623 | 0.027 | 26.399 | 26.698 | 27.141 | 27.433 | 28.018 | 28.532 | 29.272 | 30.143 | 30.931 | 30.621 | 30.391 | 30.105 | 29.713 | 30.130 | 30.537 | 29.585 | 29.803 | 29.860 | 29.804 | 29.865 | 29.449 | 29.909 | 25.241 | 22:39:19 09.05.2015 |
| 11 | 1.518 | -0.618 | 24.107 | 0.001 | -0.002 | -55.830 | -16.236 | 0.034 | 26.398 | 26.699 | 27.143 | 27.434 | 28.018 | 28.531 | 29.272 | 30.144 | 30.934 | 30.622 | 30.393 | 30.108 | 29.715 | 30.131 | 30.538 | 29.583 | 29.800 | 29.860 | 29.803 | 29.867 | 29.447 | 29.905 | 25.262 | 22:39:20 09.05.2015 |
| 12 | 1.518 | -0.526 | 24.146 | 0.001 | -0.002 | -54.729 | -15.866 | 0.045 | 26.399 | 26.699 | 27.143 | 27.436 | 28.017 | 28.532 | 29.273 | 30.145 | 30.933 | 30.623 | 30.396 | 30.111 | 29.717 | 30.131 | 30.539 | 29.582 | 29.879 | 29.859 | 29.802 | 29.868 | 29.444 | 29.901 | 25.275 | 22:39:21 09.05.2015 |
| 13 | 1.518 | -0.520 | 24.205 | 0.001 | -0.002 | -53.117 | -17.117 | 0.047 | 26.399 | 26.701 | 27.144 | 27.435 | 28.017 | 28.532 | 29.275 | 30.145 | 30.933 | 30.622 | 30.396 | 30.112 | 29.718 | 30.132 | 30.539 | 29.580 | 29.877 | 29.858 | 29.801 | 29.857 | 29.441 | 29.899 | 25.284 | 22:39:22 09.05.2015 |
| 14 | 1.518 | -0.532 | 24.245 | 0.001 | -0.002 | -54.761 | -17.541 | 0.035 | 26.401 | 26.703 | 27.144 | 27.436 | 28.017 | 28.532 | 29.275 | 30.147 | 30.933 | 30.624 | 30.397 | 30.115 | 29.717 | 30.134 | 30.538 | 29.581 | 29.876 | 29.855 | 29.800 | 29.856 | 29.438 | 29.895 | 25.288 | 22:39:23 09.05.2015 |
| 15 | 1.518 | -0.484 | 24.299 | 0.001 | -0.002 | -56.684 | -16.708 | 0.028 | 26.402 | 26.703 | 27.146 | 27.437 | 28.017 | 28.533 | 29.275 | 30.147 | 30.933 | 30.625 | 30.397 | 30.117 | 29.719 | 30.136 | 30.541 | 29.581 | 29.876 | 29.854 | 29.798 | 29.852 | 29.436 | 29.893 | 25.293 | 22:39:24 09.05.2015 |
| 16 | 1.518 | -0.429 | 24.396 | 0.001 | -0.002 | -55.347 | -16.292 | 0.036 | 26.403 | 26.705 | 27.147 | 27.437 | 28.016 | 28.533 | 29.276 | 30.150 | 30.932 | 30.625 | 30.397 | 30.120 | 29.719 | 30.138 | 30.543 | 29.581 | 29.874 | 29.851 | 28.996 | 29.851 | 29.434 | 29.890 | 25.296 | 22:39:25 09.05.2015 |
| 17 | 1.518 | -0.441 | 24.455 | 0.001 | -0.002 | -53.466 | -16.606 | 0.045 | 26.404 | 26.705 | 27.147 | 27.437 | 28.015 | 28.533 | 29.277 | 30.149 | 30.934 | 30.626 | 30.399 | 30.122 | 29.721 | 30.139 | 30.542 | 29.581 | 29.872 | 29.850 | 28.994 | 29.848 | 29.431 | 29.889 | 25.298 | 22:39:26 09.05.2015 |
| 18 | 1.518 | -0.590 | 24.502 | 0.001 | -0.002 | -54.317 | -17.128 | 0.042 | 26.405 | 26.707 | 27.147 | 27.437 | 28.015 | 28.532 | 29.277 | 30.149 | 30.933 | 30.626 | 30.399 | 30.124 | 29.722 | 30.142 | 30.544 | 29.582 | 29.872 | 29.849 | 28.994 | 29.846 | 29.431 | 29.888 | 25.300 | 22:39:27 09.05.2015 |
| 19 | 1.518 | -0.435 | 24.522 | 0.001 | -0.002 | -55.660 | -17.331 | 0.035 | 26.405 | 26.707 | 27.147 | 27.438 | 28.015 | 28.533 | 29.279 | 30.149 | 30.932 | 30.627 | 30.402 | 30.127 | 29.723 | 30.144 | 30.547 | 29.583 | 29.870 | 29.847 | 28.993 | 29.845 | 29.428 | 29.884 | 25.301 | 22:39:28 09.05.2015 |
| 20 | 1.518 | -0.252 | 24.556 | 0.001 | -0.002 | -55.191 | -16.697 | 0.035 | 26.407 | 26.709 | 27.147 | 27.436 | 28.016 | 28.532 | 29.279 | 30.150 | 30.932 | 30.627 | 30.404 | 30.129 | 29.724 | 30.147 | 30.547 | 29.584 | 29.870 | 29.845 | 28.991 | 29.842 | 29.425 | 29.882 | 25.303 | 22:39:29 09.05.2015 |
| 21 | 1.518 | -0.429 | 24.556 | 0.001 | -0.002 | -54.330 | -16.704 | 0.037 | 26.408 | 26.711 | 27.148 | 27.438 | 28.016 | 28.534 | 29.279 | 30.148 | 30.934 | 30.628 | 30.406 | 30.131 | 29.728 | 30.146 | 30.551 | 29.585 | 29.870 | 29.843 | 28.988 | 29.840 | 29.424 | 29.880 | 25.303 | 22:39:30 09.05.2015 |
| 22 | 1.518 | -0.514 | 24.523 | 0.001 | -0.002 | -54.999 | -16.500 | 0.039 | 26.410 | 26.713 | 27.150 | 27.439 | 28.017 | 28.534 | 29.279 | 30.148 | 30.933 | 30.629 | 30.409 | 30.134 | 29.729 | 30.149 | 30.552 | 29.587 | 29.870 | 29.841 | 28.987 | 29.838 | 29.421 | 29.876 | 25.305 | 22:39:31 09.05.2015 |
| 23 | 1.519 | -0.593 | 24.513 | 0.001 | -0.002 | -55.158 | -16.299 | 0.041 | 26.411 | 26.715 | 27.151 | 27.438 | 28.018 | 28.536 | 29.279 | 30.150 | 30.935 | 30.629 | 30.412 | 30.135 | 29.732 | 30.152 | 30.552 | 29.589 | 29.869 | 29.840 | 28.985 | 29.834 | 29.419 | 29.873 | 25.305 | 22:39:32 09.05.2015 |
| 24 | 1.518 | -0.782 | 24.511 | 0.001 | -0.002 | -53.952 | -17.610 | 0.041 | 26.414 | 26.718 | 27.152 | 27.440 | 28.019 | 28.536 | 29.280 | 30.150 | 30.934 | 30.629 | 30.412 | 30.139 | 29.735 | 30.155 | 30.554 | 29.592 | 29.870 | 29.838 | 28.984 | 29.831 | 29.418 | 29.870 | 25.306 | 22:39:33 09.05.2015 |
| 25 | 1.519 | -1.014 | 24.524 | 0.001 | -0.002 | -54.528 | -17.569 | 0.035 | 26.417 | 26.720 | 27.154 | 27.442 | 28.021 | 28.536 | 29.280 | 30.150 | 30.936 | 30.630 | 30.412 | 30.143 | 29.737 | 30.157 | 30.558 | 29.593 | 29.868 | 29.836 | 28.984 | 29.831 | 29.414 | 29.867 | 25.306 | 22:39:34 09.05.2015 |
| 26 | 1.518 | -0.702 | 24.525 | 0.001 | -0.002 | -56.342 | -16.330 | 0.033 | 26.417 | 26.724 | 27.155 | 27.442 | 28.022 | 28.538 | 29.282 | 30.152 | 30.936 | 30.631 | 30.412 | 30.146 | 29.740 | 30.160 | 30.560 | 29.595 | 29.869 | 29.834 | 28.981 | 29.830 | 29.415 | 29.864 | 25.307 | 22:39:35 09.05.2015 |
| 27 | 1.518 | -0.800 | 24.530 | 0.001 | -0.002 | -54.858 | -16.657 | 0.040 | 26.420 | 26.724 | 27.157 | 27.445 | 28.022 | 28.538 | 29.281 | 30.152 | 30.937 | 30.632 | 30.412 | 30.148 | 29.744 | 30.163 | 30.560 | 29.597 | 29.869 | 29.833 | 28.979 | 29.828 | 29.414 | 29.863 | 25.307 | 22:39:36 09.05.2015 |
| 28 | 1.518 | -0.441 | 24.551 | 0.001 | -0.002 | -53.179 | -16.953 | 0.043 | 26.422 | 26.726 | 27.157 | 27.445 | 28.023 | 28.539 | 29.284 | 30.155 | 30.938 | 30.633 | 30.413 | 30.150 | 29.745 | 30.166 | 30.563 | 29.598 | 29.869 | 29.832 | 28.978 | 29.826 | 29.413 | 29.860 | 25.308 | 22:39:37 09.05.2015 |
| 29 | 1.518 | -0.587 | 24.535 | 0.001 | -0.002 | -55.014 | -16.989 | 0.037 | 26.424 | 26.726 | 27.158 | 27.447 | 28.023 | 28.542 | 29.285 | 30.154 | 30.938 | 30.633 | 30.412 | 30.152 | 29.747 | 30.170 | 30.564 | 29.600 | 29.869 | 29.830 | 28.976 | 29.824 | 29.410 | 29.857 | 25.308 | 22:39:38 09.05.2015 |
| 30 | 1.518 | -0.465 | 24.529 | 0.001 | -0.002 | -55.964 | -16.901 | 0.035 | 26.425 | 26.726 | 27.159 | 27.448 | 28.024 | 28.543 | 29.287 | 30.156 | 30.939 | 30.634 | 30.412 | 30.156 | 29.749 | 30.170 | 30.566 | 29.599 | 29.868 | 29.829 | 28.974 | 29.820 | 29.409 | 29.855 | 25.309 | 22:39:39 09.05.2015 |
| 31 | 1.518 | -0.350 | 24.580 | 0.001 | -0.002 | -54.706 | -16.900 | 0.038 | 26.427 | 26.727 | 27.160 | 27.450 | 28.027 | 28.543 | 29.288 | 30.156 | 30.939 | 30.635 | 30.414 | 30.157 | 29.752 | 30.173 | 30.567 | 29.599 | 29.866 | 29.827 | 28.972 | 29.819 | 29.407 | 29.850 | 25.309 | 22:39:40 09.05.2015 |
| 32 | 1.518 | -0.733 | 24.592 | 0.001 | -0.002 | -54.255 | -16.840 | 0.040 | 26.428 | 26.729 | 27.162 | 27.452 | 28.028 | 28.544 | 29.287 | 30.154 | 30.940 | 30.637 | 30.413 | 30.161 | 29.754 | 30.174 | 30.568 | 29.599 | 29.865 | 29.826 | 28.972 | 29.818 | 29.404 | 29.849 | 25.310 | 22:39:41 09.05.2015 |
| 33 | 1.518 | -0.404 | 24.594 | 0.001 | -0.002 | -54.831 | -16.976 | 0.039 | 26.430 | 26.731 | 27.163 | 27.454 | 28.029 | 28.545 | 29.289 | 30.156 | 30.941 | 30.636 | 30.415 | 30.162 | 29.755 | 30.175 | 30.569 | 29.598 | 29.865 | 29.823 | 28.969 | 29.815 | 29.403 | 29.845 | 25.310 | 22:39:42 09.05.2015 |
| 34 | 1.518 | -0.520 | 24.599 | 0.001 | -0.002 | -54.040 | -17.253 | 0.038 | 26.431 | 26.732 | 27.165 | 27.456 | 28.032 | 28.547 | 29.288 | 30.154 | 30.942 | 30.637 | 30.416 | 30.165 | 29.758 | 30.175 | 30.571 | 29.597 | 29.864 | 29.822 | 28.967 | 29.813 | 29.402 | 29.841 | 25.310 | 22:39:43 09.05.2015 |
| 35 | 1.518 | -0.490 | 24.580 | 0.001 | -0.002 | -55.292 | -16.629 | 0.035 | 26.433 | 26.736 | 27.166 | 27.457 | 28.033 | 28.549 | 29.288 | 30.154 | 30.941 | 30.638 | 30.417 | 30.167 | 29.760 | 30.178 | 30.572 | 29.597 | 29.862 | 29.819 | 28.964 | 29.814 | 29.399 | 29.839 | 25.310 | 22:39:44 09.05.2015 |
| 36 | 1.518 | -0.344 | 24.528 | 0.001 | -0.002 | -55.879 | -16.127 | 0.039 | 26.436 | 26.738 | 27.168 | 27.460 | 28.034 | 28.549 | 29.290 | 30.155 | 30.940 | 30.639 | 30.416 | 30.170 | 29.763 | 30.179 | 30.573 | 29.596 | 29.861 | 29.817 | 28.962 | 29.812 | 29.397 | 29.835 | 25.310 | 22:39:45 09.05.2015 |
| 37 | 1.518 | -0.636 | 24.541 | 0.001 | -0.002 | -53.560 | -17.276 | 0.043 | 26.437 | 26.739 | 27.170 | 27.463 | 28.035 | 28.551 | 29.291 | 30.156 | 30.940 | 30.639 | 30.419 | 30.173 | 29.764 | 30.180 | 30.573 | 29.593 | 29.858 | 29.816 | 28.960 | 29.809 | 29.393 | 29.830 | 25.311 | 22:39:46 09.05.2015 |
| 38 | 1.518 | -0.398 | 24.493 | 0.001 | -0.002 | -54.502 | -17.843 | 0.037 | 26.440 | 26.741 | 27.172 | 27.464 | 28.037 | 28.552 | 29.290 | 30.156 | 30.941 | 30.639 | 30.422 | 30.176 | 29.766 | 30.181 | 30.574 | 29.594 | 29.857 | 29.813 | 28.958 | 29.806 | 29.391 | 29.828 | 25.311 | 22:39:47 09.05.2015 |
| 39 | 1.518 | -0.143 | 24.503 | 0.001 | -0.002 | -56.509 | -16.984 | 0.031 | 26.441 | 26.741 | 27.175 | 27.466 | 28.039 | 28.554 | 29.291 | 30.157 | 30.942 | 30.640 | 30.424 | 30.179 | 29.767 | 30.183 | 30.576 | 29.592 | 29.855 | 29.811 | 28.955 | 29.803 | 29.387 | 29.823 | 25.311 | 22:39:48 09.05.2015 |
| 40 | 1.519 | -0.465 | 24.515 | 0.001 | -0.002 | -55.512 | -15.833 | 0.030 | 26.442 | 26.743 | 27.176 | 27.468 | 28.039 | 28.555 | 29.292 | 30.158 | 30.941 | 30.641 | 30.427 | 30.184 | 29.769 | 30.186 | 30.577 | 29.592 | 29.853 | 29.808 | 28.952 | 28.999 | 29.384 | 29.818 | 25.312 | 22:39:49 09.05.2015 |
| 41 | 1.518 | -0.441 | 24.538 | 0.001 | -0.002 | -52.856 | -16.322 | 0.046 | 26.443 | 26.745 | 27.177 | 27.470 | 28.043 | 28.557 | 29.294 | 30.159 | 30.941 | 30.640 | 30.429 | 30.186 | 29.770 | 30.189 | 30.577 | 29.591 | 29.850 | 29.805 | 28.950 | 28.996 | 29.380 | 29.816 | 25.311 | 22:39:50 09.05.2015 |
| 42 | 1.518 | -0.618 | 24.518 | 0.001 | -0.002 | -53.304 | -17.911 | 0.042 | 26.445 | 26.747 | 27.180 | 27.470 | 28.044 | 28.559 | 29.294 | 30.160 | 30.943 | 30.642 | 30.432 | 30.189 | 29.773 | 30.191 | 30.580 | 29.590 | 29.848 | 29.803 | 28.947 | 28.994 | 29.378 | 29.812 | 25.312 | 22:39:51 09.05.2015 |
| 43 | 1.518 | -0.319 | 24.532 | 0.001 | -0.002 | -56.668 | -17.774 | 0.031 | 26.446 | 26.748 | 27.183 | 27.472 | 28.047 | 28.561 | 29.295 | 30.160 | 30.943 | 30.643 | 30.436 | 30.194 | 29.775 | 30.192 | 30.582 | 29.589 | 29.846 | 29.800 | 28.945 | 28.992 | 29.377 | 29.808 | 25.312 | 22:39:52 09.05.2015 |
| 44 | 1.518 | -0.368 | 24.506 | 0.001 | -0.002 | -56.249 | -16.983 | 0.029 | 26.447 | 26.750 | 27.184 | 27.474 | 28.047 | 28.562 | 29.295 | 30.162 | 30.942 | 30.643 | 30.438 | 30.195 | 29.777 | 30.193 | 30.582 | 29.587 | 29.843 | 28.998 | 28.942 | 28.991 | 29.373 | 29.806 | 25.312 | 22:39:53 09.05.2015 |

**Figure 14.** TOB-file acquired by the heat flow probe.

thermistors, the blue corresponds to the temperature sensor PT100. The stability of the probe can be seen in the second and third plot representing the tilt along the x and y direction and the acceleration. The bottom plot shows the pressure vs. time which is a direct measure of the water depth.

The *probe device file* contains important parameters about the heat flow probe (i.e., sensor count, device id, length and radius of the string, among others).

The important parameters concerning the station are found in the *station parameter file*.

The *temperature offset file* contains the offset for each thermistor of the sensor string calibrated for ten minutes at a constant water depth.

Time ranges (from deployment to recovery) of all penetration of a station and data like water depth and geographical coordinates are saved in the *pick file*.

After all the above files are read into the GHF-Tool a *penetration file* for each penetration after re sampling the data is created. The *pen-file* contains important information concerning the heat flow measurement.

Before processing the *pen-file* with the T2C-function, the *T2C device parameter file* containing several parameters is loaded for the processing. Furthermore, the *omit file* and the *assumed conductivity file* contain information about omitted sensors and assumed conductivities, respectively. The inferred conductivities may be useful for repeated measurements in similar sedimentary environments. After processing, several result files, which will be discussed in Section 2.3.3, are generated, which include: raw temperature data, thermal gradient, conductivity, diffusivity, capacity and the Bullard plot with errors.

### 2.3.2 Inversion of heat flow data

The first heat flow measurements were carried out by (Revelle and Maxwell, 1952; Bullard, 1954b). They used a a long metal tube with thermistors on the inside. The probe entered the sediment and recorded the temperature during 30 minutes. Because of the frictional heat generated during the penetration, the sediment temperatures could not be directly measured. However, the

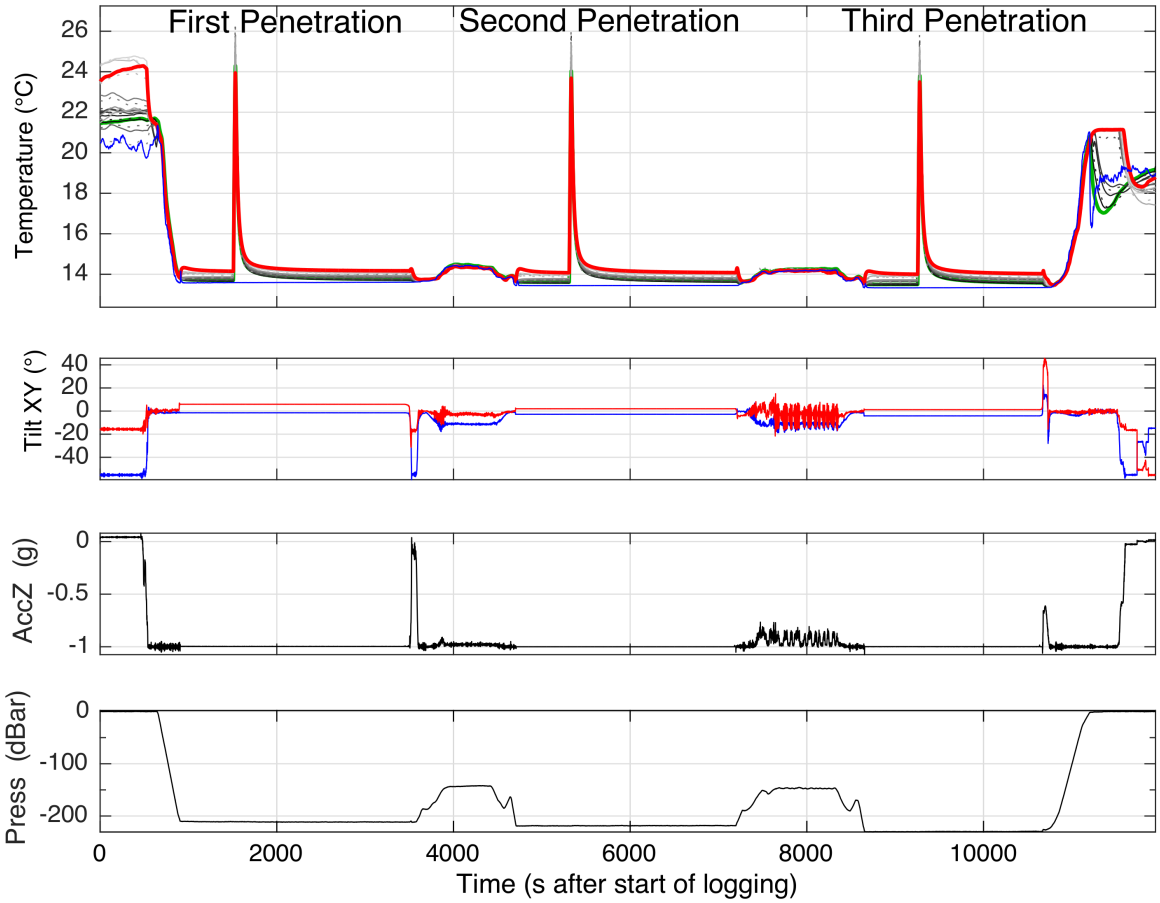


**Figure 15.** Example of multipenetration station. The plots from the top to the bottom are temperature, Tilt, acceleration and Pressure against time.

dissipation of the frictional heat into the sediment could be described by the cooling of a metal cylinder in a homogeneous full-space (Bullard, 1954b; Carslaw and Jaeger, 1959). The extrapolation of this decay leads to the undisturbed sediment temperatures. Sediment cores next to the measurements sites were used to determine the thermal conductivity. Assuming a pure conductive regime without horizontal advective heat transport the heat flow can be calculated using Fourier's law (Equation 3). Bullard proposed that the sediment conductivities can also be determined from the temperature decay but his idea was dismissed, because of the unknown frictional energy. After new mechanical and electronic improvements in the probe's design, both the frictional and heat-pulse decay could be described as a decay of a cylindrical body. These advancements made the analysis easier.

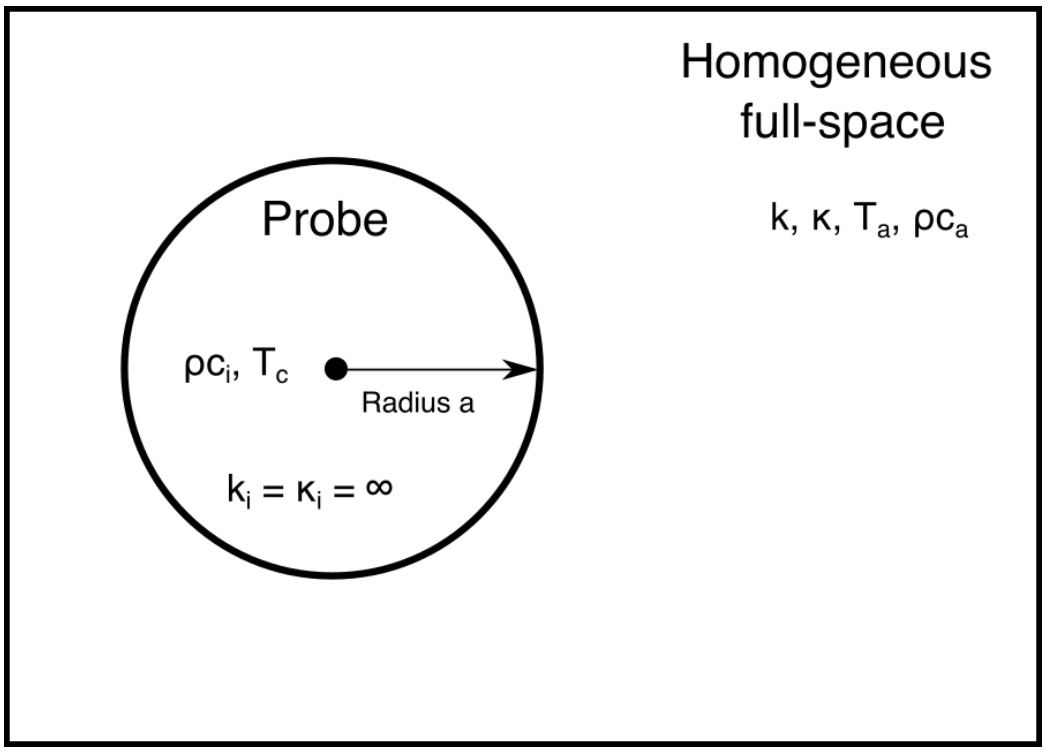


**Figure 16.** Model of a cylindrical probe with an infinitely long cylinder, located in a homogeneous full space. $k_i$, $\kappa_i$, $\rho c_i$ and $T_c$ are the thermal conductivity, diffusivity, capacity and the initial temperature of the cylinder respectively. $k$, $\kappa$, $\rho c_a$ and $T_a$ are the thermal properties of the medium. The problem is cylindrical symmetrical and independent of z. Modified from Hartmann (2004)

#### 2.3.2.1 Calculations on the cylindrical probe

The following two subsections are taken and modified from Hartmann and Villinger (2002); Hartmann (2004).

Pure conductive heat transfer problems are expressed by a parabolic differential equation as seen in Section 1.1:

$$\nabla^2 T = \frac{1}{\kappa}\frac{\partial T}{\partial t} \tag{10}$$

Since this is a radial symmetry problem, it is useful to transform Equation 3 into cylindrical coordinates:

$$\frac{\partial^2 T}{\partial r^2} + \frac{1}{r}\frac{\partial T}{\partial r} + \frac{1}{r^2}\frac{\partial T}{\partial \phi} + \frac{\partial T}{\partial z} = \frac{1}{\kappa}\frac{\partial T}{\partial t} \tag{11}$$

For the calculation of the decay curve of the sensor tube, we used the following model: an indefinitely long cylinder with radius $a$ is located in a homogeneous full space (Figure 16). The cylinder has infinite conductivity and diffusivity. At $t = 0$ the temperature is $T_0$ and $T_a$ for the cylinder and sediment respectively. The full space has finite thermal conductivity and diffusivity. For $t > 0$ the heat flow over the edge of the cylinder is equal to the temporal change in the internal heat of the cylinder. If there is no dependence of $\phi$ and $z$, Equation 11 can be reduced to the one dimensional problem:

$$\frac{\partial^2 T}{\partial r^2} + \frac{1}{r}\frac{\partial T}{\partial r} - \frac{1}{\kappa}\frac{\partial T}{\partial r} = 0 \quad r > a, t > 0 \tag{12}$$

with initial condition at $t = 0$:

$$T = \begin{cases} T_0 & r \leq a \\ T_a & r > a \end{cases} \quad t = 0 \tag{13}$$

and the flowing boundary condition:

$$k\frac{\partial T}{\partial r} 2\pi a = m c_i \frac{\partial T}{\partial t} \quad r = a, t > 0 \tag{14}$$

it is important to note that th following assumptions of the model do not correspond to the reality.

- The geometry of the sensor tube does not correspond to the model assumption. The sensor tube is made off different materials of finite thermal conductivity.
- At the contact surface between the sensor tube and sediment, a water film can provoke contact resistance.
- The model uses an initial temperature $T_0$ of the cylinder, which in practice is an infinite short heating pulse. However, the heating pulse lasts around 20 seconds.
- The sensor tube is not infinitely in the z direction, so axial heat flow may occur.

The axial heat flow is hard to prove but for a continued cylindrical heated source with a ratio

*length/radius* of 30, the error of $k$ is around 0.1% (Blackwell, 1956).

From the decay curve of the cylinder the temperature at the center ($a = 0$) of the cylinder can be determined by Hartmann and Villinger (2002):

$$T(\tau) = (T_0 - T_a)[F(\alpha, \tau) + T_a] \tag{15}$$

with $F(\alpha, \tau)$ (Bullard, 1954b; Carslaw and Jaeger, 1959):

$$F(\alpha, \tau) = \frac{4\alpha}{\pi^2} \int_0^\infty \frac{e^{-\tau u^2}}{u\phi(u, \alpha)} du \tag{16}$$

$$\phi(u, \alpha) = (uJ_0(u) - \alpha J_1(u))^2 + (uY_0(u) - \alpha Y_1(u))^2 \tag{17}$$

Here $\alpha = 2(\rho c)_s/(\rho c)_c$ is the ratio of the heat capacities per volume of the sediment and cylinder, $\tau = (\kappa/a^2)t$ the dimensionless time, $J_0$, $J_1$, $Y_0$ and $Y_1$ are the zero and first order Bessel and Neumann functions, respectively and $u$ the integration variable. With Equation 16 the forward problem is known, which means that by knowing the physical parameters the decay curve can be calculated. However, solving the inverse problem is needed if we want to determine the physical parameters using a decay curve.

#### 2.3.2.2 Inverse problem of the decay curve

In order to determine of the sediment conductivities from a decay curve, the temperature integral $F(\alpha, \tau)$ needs to be inverted for these parameters. $F$ is non linear with respect to both $\alpha$ and $\tau$ and in this case the parameters can only be calculated with an iterative method. $F(\alpha, \tau)$ can be approximated (Hartmann, 2004):

$$F(\alpha, \tau) \approx \frac{1}{2\alpha\tau} - \frac{1}{4\alpha\tau^2} - \frac{\alpha - 2}{4\alpha^2\tau^2} ln \frac{4\tau}{C} \tag{18}$$

with $C \sim 1.7811$ being the Euler constant. Using only the first order term of Equation 18 and the definitions of $\alpha$ and $\tau$ we can substitute into Equation 16 and obtain the temperature given by $F$, and , the temperature then is given by:

$$T(t) = \frac{Q}{4\pi k t} + T_a \tag{19}$$

with $Q$ being the heat per unit length within the cylinder. Figure 17 shows the approximation and exact solution for $F(\alpha, \tau)$. It is noticed that the approximation gets a 1% accuracy for $\tau > 10$.

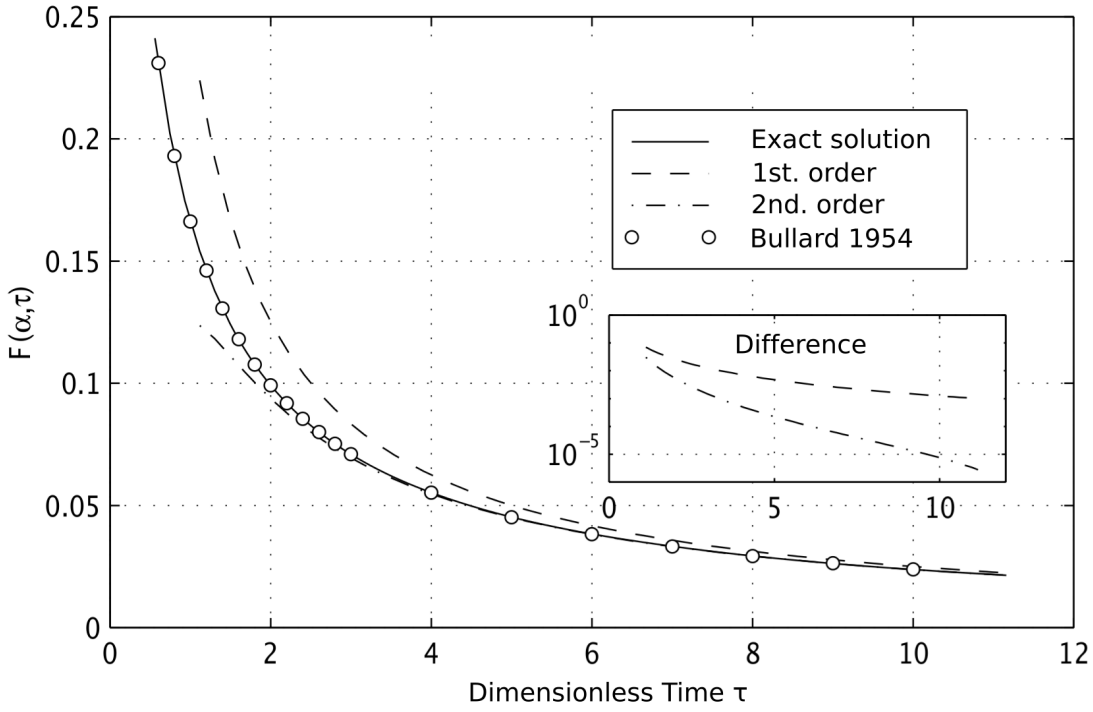


**Figure 17.** Comparison of approximations with the exact solution for the decay curve. The approximation for first and second order are dashed and dashed point curves, respectively. Furthermore the vales calculated by Bullard (1954a) are plotted (o). Modified from Hartmann (2004)

Higher order approximations are excluded from this discussion. Early temperature records are affected by a deviation from the model and must therefore be excluded from the analysis (Hartmann and Villinger, 2002). Records within the analyzed time range still deviates slightly from the ideal fit, due to a contact resistance between the sensor tube and the sediment and due to a finite heat pulse of 20 s length. This deviation can be compensated by shifting the time origin introducing a new parameter, the time-shift $t_s$, which, from a physical point of view, has shown reliable results but has no mathematical proof (Hyndman *et al.*, 1979; Villinger and Davis, 1987). Time-shift can

be originated by the heat that is not instantly and equally distributed over the whole sensor tube, but depends on the material which the tube is made of. Another possible source is the increasing amount of contact wires of the 22 thermistors within the sensor tube to the top, which increases the contact resistance. For this reason, the time-shift for each thermistor is inverted separately.

The negative time-shift for the frictional decay curve is explained by the fact that the frictional heat from the penetration, produced at the surface of the sensor tube, partly reaches the sediment. Second, the frictional energy generated at the interface of the sensor tube/sediment takes time to reach the thermistors inside the tube. This same phenomenon leads to a positive time-shift for the pulse decay curve. Overall, the time-shift for the frictional decay curve is negative, but less consistent and has greater variation, because the frictional heat of the sensor tube and the sediment for each measurement is different (Hartmann, 2004).

A meaningful parametrization of the problem is the following:

- $k$: thermal conductivity, [$\frac{W}{mK}$].
- $\kappa$: thermal diffusivity, [$10^{-7}\frac{m^2}{s}$].
- $Q$: heat per unit length, at $t = 0$, generated by the friction at the penetration of the probe or the heat pulse, [$\frac{J}{m}$].
- $\rho c$: heat capacity of the probe per volume, [$10^6\frac{J}{Km^3}$].
- $t_s$: displacement of the initial time, which is necessary to compensate for deviations of the model from the reality, [$s$].
- $T_a$: The undisturbed sediment temperature, [$^\circ C$].

These set of parameters are called the parameters vector **m**.

$$m = (k, \kappa, Q, \rho c, t_s, T_a) \tag{20}$$

The temperature rise after the heat pulse can be expressed:

$$T_0 - T_a = \frac{Q}{\pi a^2(\rho c)} \tag{21}$$

To achieve the inversion for Equation 15 the actual physical parameters need to be substituted into Equation 16 and Equation 17. This yields:

$$T = \frac{8\lambda Q}{\pi^3 a^2 \kappa (\rho c)^2} \int_0^\infty \frac{e^{-u^2 \frac{\kappa}{a^2}(t-t_s)}}{u\phi(u)} du + T_a \tag{22}$$

$$\phi(u) = \left(uJ_0(u) - \frac{2\lambda}{\kappa(\rho c)} J_1\right)^2 + \left(uY_0(u) - \frac{2\lambda}{\kappa(\rho c)} Y_1\right)^2 \tag{23}$$

A Taylor expansion can be used to invert Equation 22 (Menke, 1989). Once linearized, the inverse problem can be formulated as a linear system of equations such as:

$$G \cdot \Delta m = \Delta d \tag{24}$$

where $G$ is the kernel, containing the jacobian derivatives associated to Equation 23, $\Delta m$ the parameter vector and $\Delta d$ the data vector residuals. The solution of the problem is to solve the liner system (Equation 24) to obtain $m$. Hartmann (2004) provides details of the jacobian computation and solves Equation 24 using a single value decomposition (SVD) (Menke, 1989). In an SVD solution, the model matrix is decomposed in three matrices $G = U \cdot S \cdot V^T$. Since U and V are orthogonal systems, the solution to the inverse problem is simply:

$$\Delta m = V S^{-1} U^T d. \tag{25}$$

Once the conductivity and temperature are calculated from the decay curves, the heat flow is determined using a method proposed by Bullard (1939). It is based on the concept of thermal resistance $R = \sum_{i=1}^{N} \frac{\Delta z_i}{k(z)_i}$ with units of $[m^2 K/W]$. Using Fourier's law for a horizontally layered case,

$$q \sum_{i=1}^{N} \frac{1}{k(z)_i} = \frac{T_i - T_0}{\Delta z_i} \tag{26}$$

```
Cruise-Transect          Wagner2015
Station                  HF005
Penetration_No.          08
Device ID                CTM950
String ID                T82SD
Date/Time_of_Pen.        2015-05-11 08:49:00
Latitude[ddd_mm.mmm]     30 59.67
Longitude[ddd_mm.mmm]    114 09.240
Depth[m]                 202.00
Tilt[ ]                  16.5
HeatingWireLength[m]     6.05
HeatingPower[J/m]        986.92

lambda_mean[W/m K]       0.987
kappa_mean[1e-07 m^2/s]  3.131
rho_c_mean[MJ/(m^3 K)]   3.158
dT/dz[K/m]               0.0692
Q[mW/m^2]                71.44


Sens_used Sens_depth T_insitu Bull_depth lambda_insitu kappa_insitu rho_c_insitu
    #         m          C    m^2 K/W      W/(m K)    1e-07 m^2/s   MJ/(m^3 K)

   22       0.000     14.619    0.000        0.875        2.621        3.339
   21       0.240     14.651    0.260        0.972        3.059        3.179
   20       0.480     14.696    0.516        0.908        2.765        3.283
   19       0.720     14.751    0.772        0.963        3.016        3.194
   18       0.960     14.804    1.021        0.967        3.031        3.188
   17       1.200     14.849    1.273        0.943        2.922        3.227
   16       1.440     14.899    1.525        0.962        3.011        3.196
   15       1.680     14.938    1.772        0.975        3.072        3.175
   14       1.920     14.978    2.016        0.992        3.149        3.149
   13       2.160     15.017    2.255        1.017        3.272        3.110
   12       2.400     15.049    2.492        1.006        3.218        3.127
   11       2.640     15.082    2.732        0.996        3.169        3.143
    9       3.120     15.142    3.211        1.007        3.223        3.125
    8       3.360     15.167    3.446        1.038        3.372        3.078
    7       3.600     15.183    3.688        0.949        2.951        3.217
    6       3.840     15.214    3.933        1.010        3.238        3.121
    5       4.080     15.225    4.175        0.978        3.086        3.170
    4       4.310     15.248    4.403        1.035        3.354        3.085
    3       4.550     15.262    4.635        1.038        3.372        3.079
    2       4.790     15.279    4.868        1.021        3.290        3.104
    1       5.030     15.292    5.097        1.078        3.568        3.022


#
#    Heatflow probe with sensor numbers:
#
#   _|=====|__22_____________11____________1__
#    |=====|
#
```

**Figure 18.** Processing results from a heat flow measuring penetration

the depth-dependent temperature is given by:

$$T(z) = T_0 + q \sum_{i=1}^{N} \frac{\Delta z_i}{k(z)_i}. \tag{27}$$

The slope of the linear regression from the temperature profiles gives the heat flow and thermal diffusivity is calculated after a relation proposed by Hyndman *et al.* (1979):

$$\kappa = \frac{k}{5.79 - 3.67k + 1.016k^2} \; [10^{-6} \frac{m^2}{s}] \tag{28}$$

The inversion is restricted to only three parameters per iteration which leads to a sequence of

processing steps for each penetration (Villinger and Davis, 1987).

1) For the frictional decay $Q, T_a, t_s$ are calculated whereas $k, \kappa, (\rho c)$ are held fixed, assuming values for $k$ and $\kappa$.

2) The residual from the former is subtracted from the heat pulse decay, reducing the $T_a$ to a known value of zero. The heat pulse decay is inverted for $k, \kappa, t_s$ with $Q, T_a, (\rho c)$ held constant. $Q$ is known from the heat pulse and $T_a$ is zero after reduction.

3) Steps 1 and 2 can be repeated using new calculated values of $k$ and $\kappa$ obtained in previous cycles.

### 2.3.3 Data presentation for a typical heat flow probe measurement

The depth-dependent temperature, thermal conductivities and thermal diffusivities are determined by T2C. The geothermal heat flow is calculated from the steady state geothermal gradient and the thermal conductivity. The volumetric thermal heat capacities are calculated from the thermal conductivities and diffusivities.

For each penetration a data file with all relevant information about the station and the sensors is saved (Figure 18).

Figure 19 shows the relative temperature plotted against time with the four stages of a heat flow measurement: penetration friction, frictional decay, heat pulse and heat pulse decay for a single penetration. Each sensor is represented by its color and is numbered from 1, representing the lowermost to 22, the uppermost sensor. The red dashed lines mark the time frame used for the inversion of the sediment temperatures and the thermal conductivities and diffusivities. The triangles represent the start of the penetration process and the heat pulse.

Figure 20 presents the temperature, thermal conductivities, diffusivities and the calculated volumetric heat capacities against penetration depth. Horizontal blue error bars show the uncertainties of the inverted temperature and thermal conductivities. The black dashed lines for the conductivity, diffusivity and volumetric heat capacity represent the mean values. Temperature points with the filled black circles are used to estimate the thermal gradient (dashed line). Note that open circles

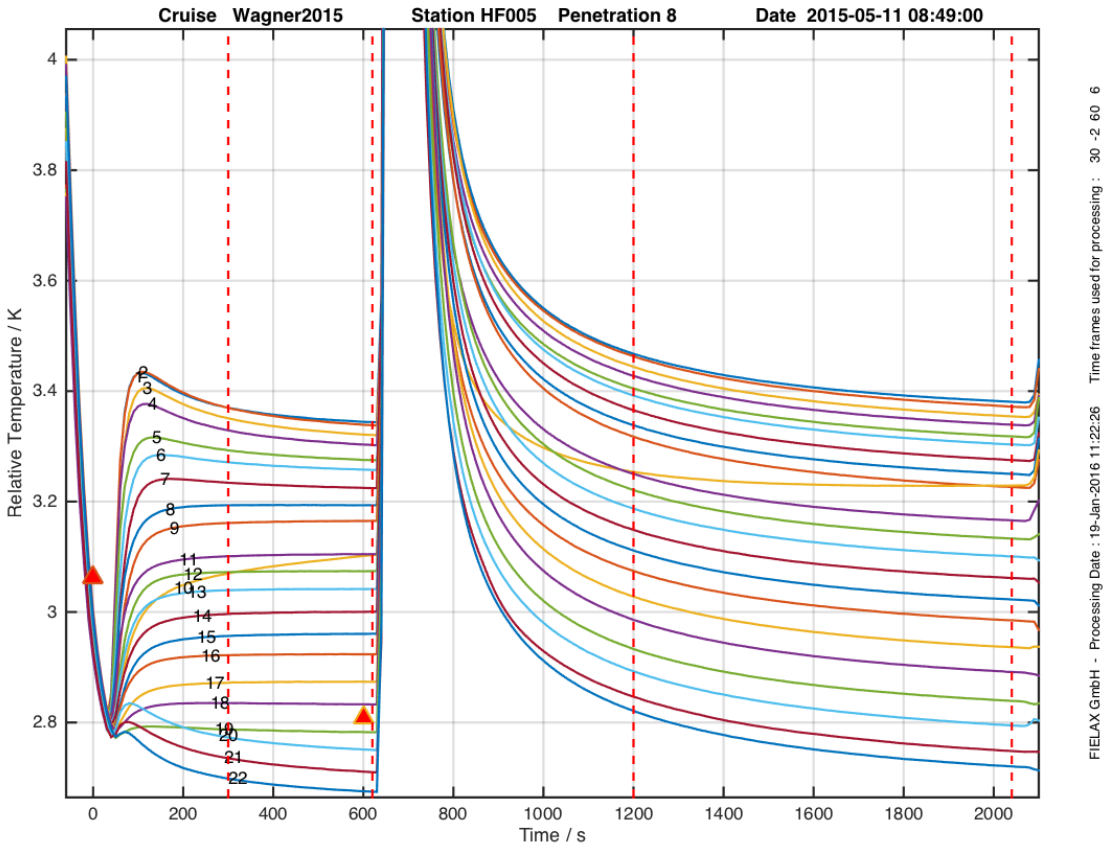


**Figure 19.** Relative temperature vs. time. The first temperature decay is generated by frictional heat. The second temperature decay results from the heat pulse. The frictional decay is used to invert for sediment temperatures, the heat pulse decay for thermal conductivity and diffusivity. Red dashed lines represent the inversion windows of the frictional and heat pulse decay.

are excluded from the estimation. The left side of Figure 21 shows the Bullard plot of the penetration, where temperature is plotted against the integrated thermal resistance. Horizontal blue error bars show the uncertainties of the temperature. The black filled circles are used for the linear regression to estimate the heat flow (dashed line). Once again, open circles are excluded from this estimation. The three panels on the right side of Figure 21 shows from top to bottom, the errors of in situ temperature, in situ thermal conductivity, and residual temperatures from the linear fit of thermal resistances against the sensor number.

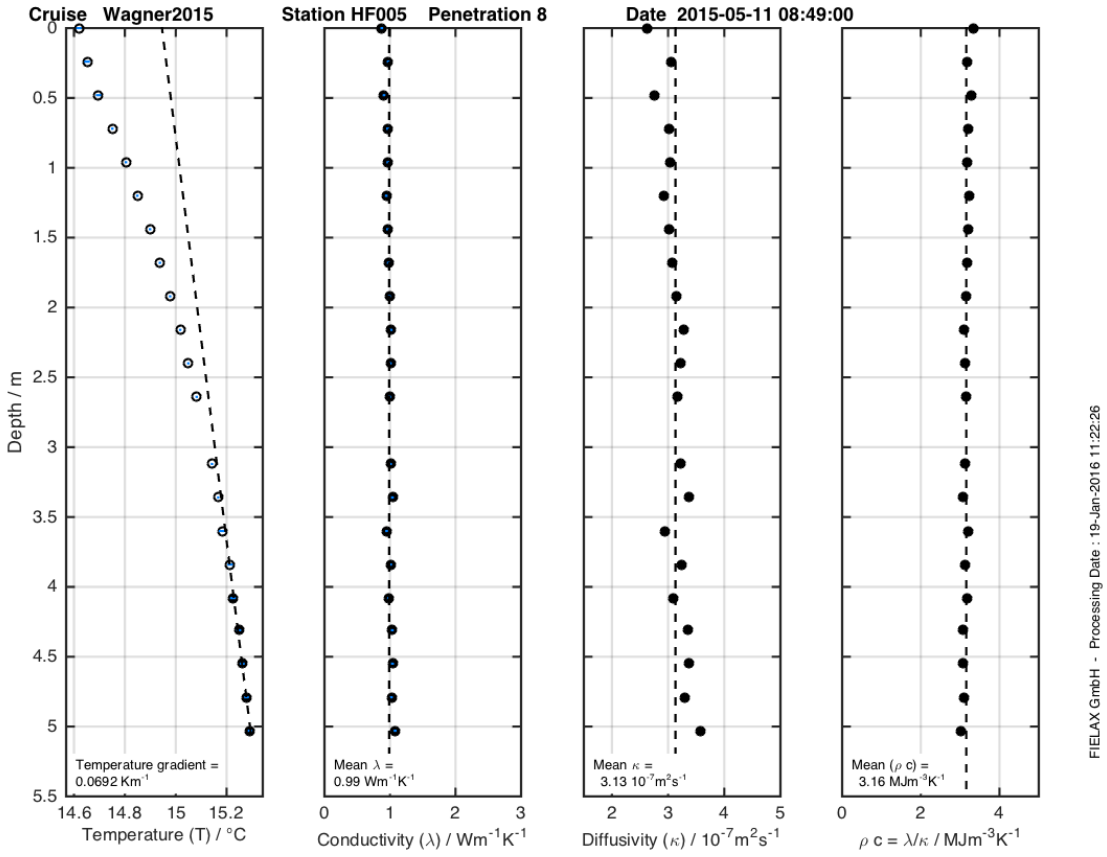


**Figure 20.** Depth-dependent in-situ temperatures, thermal conductivities and thermal diffusivities and the calculated volumetric heat capacities. Dashed lines show the mean values.

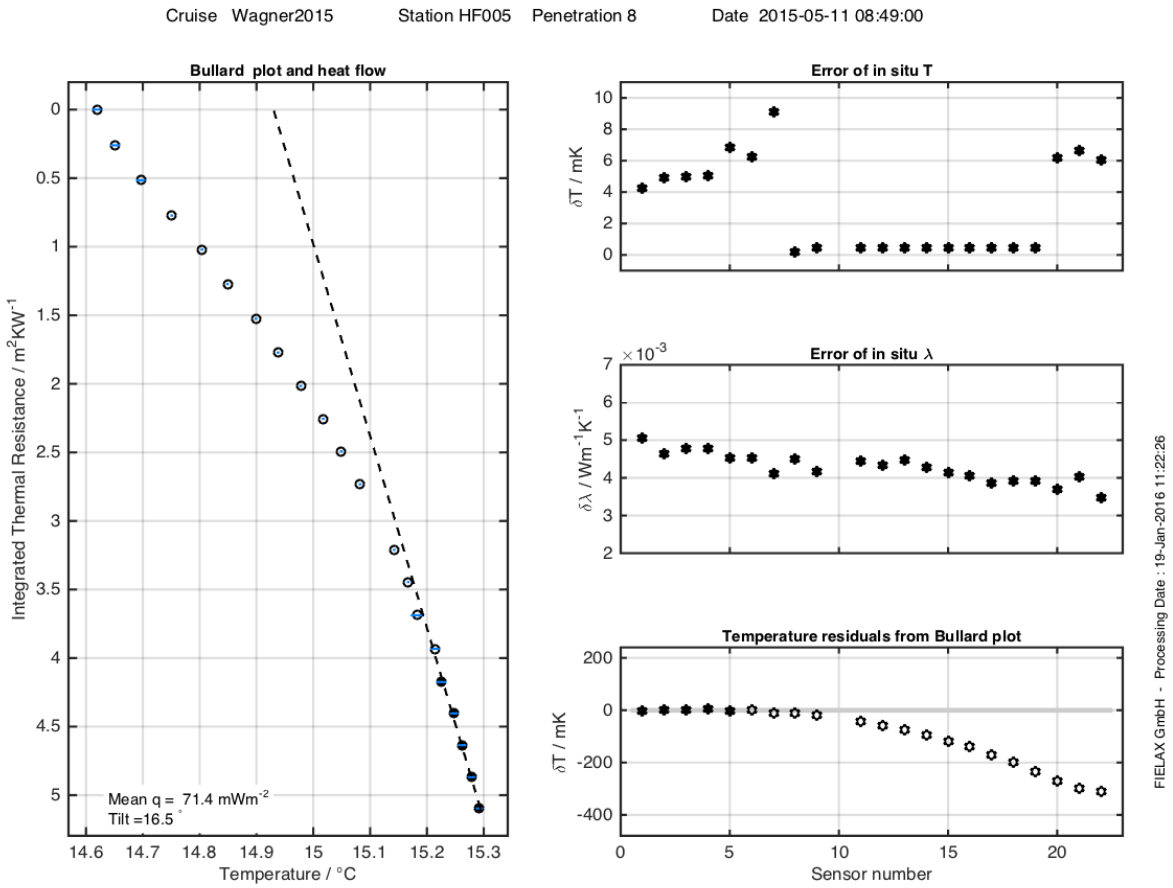


**Figure 21.** Bullard plot with resulting heat flow (heat flow evaluation, not relevant for thermal parameters profiling) and error estimates.

# Chapter 3. Environmental corrections

## 3.1 Bottom water temperature variation

In the northern Gulf of California, shallow water depths are likely lead by high variations in sediment temperature caused by significant, mainly climate induced, seasonal variation in bottom water temperature (BWT). These annual climate related oscillations show a typically sine-shaped curvature in the temperature depth profiles (Figure 22). This curvature depends on amplitude, period and sediment properties, and it is significant at shallower water depths (<300 m). Possible sources are mixing by currents in the water, gravity, and wind (Duchkov and Kazantsev, 2007). The large changes in BWT can alter sediment temperatures to depths of 6 - 8 m and disturb the steady thermal regime produced by deep heat flow.

The BWT variations can be approximated with a sinusoid at annual time scales described by Turcotte and Schubert (2014) to solve the one-dimensional, time-dependent heat conduction equation.

$$\frac{\partial T}{\partial t} = \kappa \frac{\partial^2 T}{\partial z^2}, \tag{29}$$

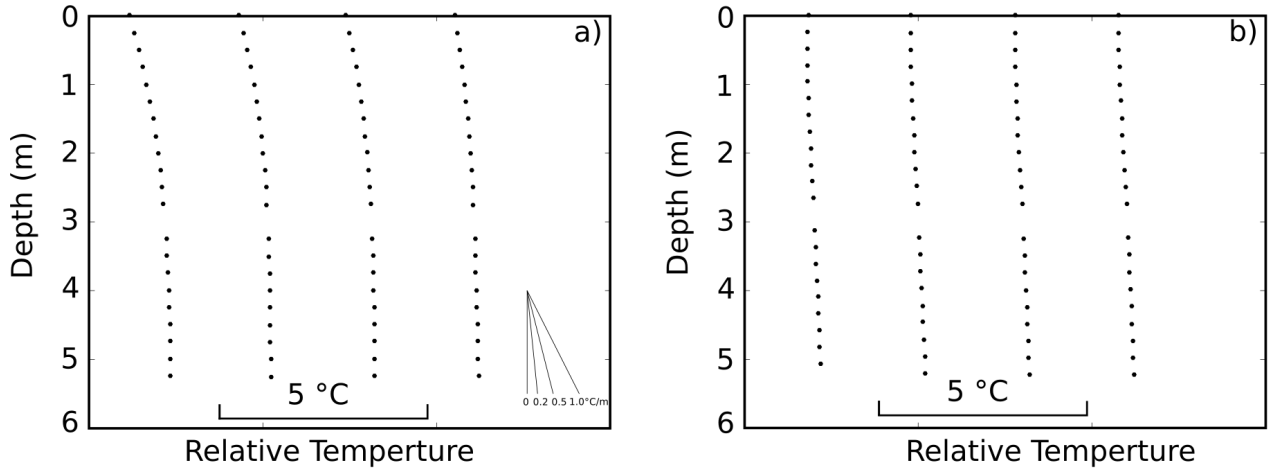


**Figure 22.** Temperature-depth profiles in the Northern Gulf of California. Profiles were obtained using a Fielax heat flow probe instrument of 22 thermistors along a 6 m long strength member. Thermistor 10 was removed from the profiles because of thermal perturbations caused by a mount point of the probe. a) Profiles taken in the Wagner basin. b) Profiles taken in the Delfín basin.

where $\kappa$ is the thermal diffusivity, which is a group of parameters composed by $k$ thermal conductivity and $\rho c$ heat capacity

$$\kappa = \frac{k}{\rho c}. \tag{30}$$

Considering a semi-infinite half-space with depth z $\geq$ and a surface with z=0. Assuming that the surface temperature is a periodic function of time:

$$T_s = T_0 + \Gamma + \Delta T cos(\omega t), \tag{31}$$

where $T_s$ is the temperature, $t$ is time, $T_0$ is the long term bottom water temperature, $\Gamma z$ the deep thermal gradient, $\Delta T$ is the amplitude of the BWT and $\omega$ the circular frequency. The circular frequency is related to the the annual temperature oscillation $\tau$:

$$\tau = \frac{1}{f} = \frac{2\pi}{\omega}. \tag{32}$$

For a yearly fluctuation of the surface temperature, $\tau$ = 1 year, $f$=3.171 $\times$ $10^{-8}$ $s^{-1}$, and $\omega$=1.992 $\times$ $10^{-7}$ rad $s^{-1}$. Assuming that $T \rightarrow T_o$ as $z \rightarrow \infty$, Equation 29 can be solved by using the method of separation of variables. Detailed mathematical steps to solve the problem can be found in Turcotte and Schubert (2014).

The temperature variation in the subsurface due to a time-periodic surface temperature is

$$T(z,t) = T_0 + \Gamma z + \Delta T \exp\left(-z\sqrt{\frac{\omega}{2\kappa}}\right) cos\left(\omega t - z\sqrt{\frac{\omega}{2\kappa}}\right) \tag{33}$$

Eq. 33 shows that the amplitude of the sinusoid decreases exponentially with depth. The surface value of this fluctuation decrease to a value of $1/e$ in a skin depth $d_\omega$:

$$d_\omega = \left(\frac{2\kappa}{\omega}\right)^{1/2} = \sqrt{\kappa\tau/\pi} \tag{34}$$

For a yearly variation in the surface temperature, the circular frequency is $\omega$=1.992 $\times$ $10^{-7}$ rad $s^{-1}$. Using a thermal diffusivity of $\kappa$ = 1 $mm^2s^{-1}$, the skin depth is 3.17 m. The more rapid the fluctuation in temperature is. The less it can penetrate subsurface because the skin depth is inverse proportional to the square root of the frequency.

To get a better value of heat flow the variability of the conductivity with depth is included by substituting Equation 8 for the deep background gradient ($\Gamma$) Equation 33 changes to:

$$T(z,t) = T_0 + q_o \sum_{i=1}^{N} \frac{\Delta z_i}{k(z)_i} + \Delta T \exp(-\xi) \, cos\left(\frac{2\pi}{\tau} t - \xi\right) \tag{35}$$

In this case Equation 35 can now be inverted for both the background thermal regime ($T_0, q_0$) and the BWT variations ($\Delta T$) and

$$\xi = \sqrt{\frac{\pi}{\tau} \sum_{i=1}^{N} \frac{z_i}{k_i/\rho c}}, \tag{36}$$

where $\tau$ is the period of the BWT variation, and $\rho c$ is the heat capacity. Here we use a constant heat capacity of 2.36 MJ $m^{-3}$ $K^{-1}$. The first two terms on the right-hand side of Equation 35 describe the background, lineal thermal regime. The ratio of the depth interval to the thermal conductivity over that interval is the thermal resistance and is summed over N intervals defined by the measured data points. The third term describes the perturbations due to the BWT variation and the summation accounts for variations in thermal conductivity with subsurface depth. The exponential term describes the attenuation of the thermal wave, which scale as the square root of the period $\pi/\tau$. Short period variations attenuate away at relatively shallow depths while long period variations penetrates to greater depth.

### 3.1.1 Sensitivity analysis

In the following section the relationship between different parameters influencing the sub-bottom temperatures as a function of depth and time are discussed. Figure 23a shows a sinusoidal bottom water temperature (BWT) curve with a period of 1 year. In this example the long-term mean

BWT sets the temperature intercept with the seafloor, $T_0$, and $\Delta$T sets the amplitude envelope. We use this curve as a forcing function at the seafloor and calculate sub-bottom temperatures using Equation 35. Figure 23b shows perturbations of the background thermal regime determined by $T_0$ and the basal heat flow, $q$.

To illustrate our ability to recover the basal heat flow in the presence of variations in BWT and thermal conductivity we perform a sensitivity experiment using Equation 35. The forward model is shown in Figure 24 and is constructed with a mean bottom water temperature of 10 °C, and a background heat flow of 150 mW m$^2$. We impose a thermal conductivity structure that has a uniform random distribution between values of 0.8 and 1.5 W m$^{-1}$ K$^{-1}$, the minimum and maximum observed thermal conductivities of our measurements. In this test the BWT has a period of 1 year, an amplitude of 1.5 °C and a phase corresponding to July. We add 10 mK of normally distributed

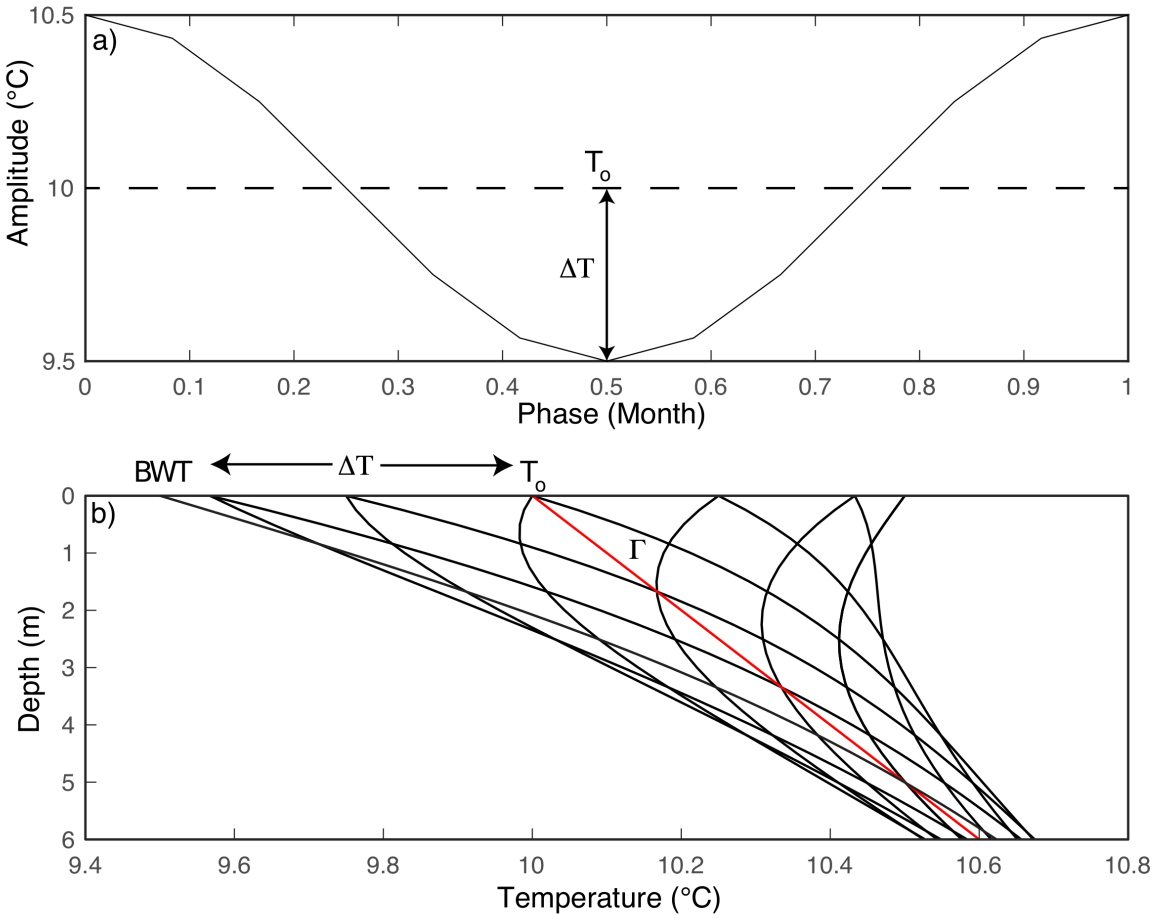


**Figure 23.** a) Temperature as a function of phase for an annual sinusoid with an amplitude $\Delta$T . b) Resulting temperature-depth profiles. $T_0$ is the long-term seafloor temperature, BWT is the bottom water temperature, $\Gamma$ is thermal gradient. This analysis shows that the BWT perturbation does not decay to negligible values within 6 m of the seafloor.

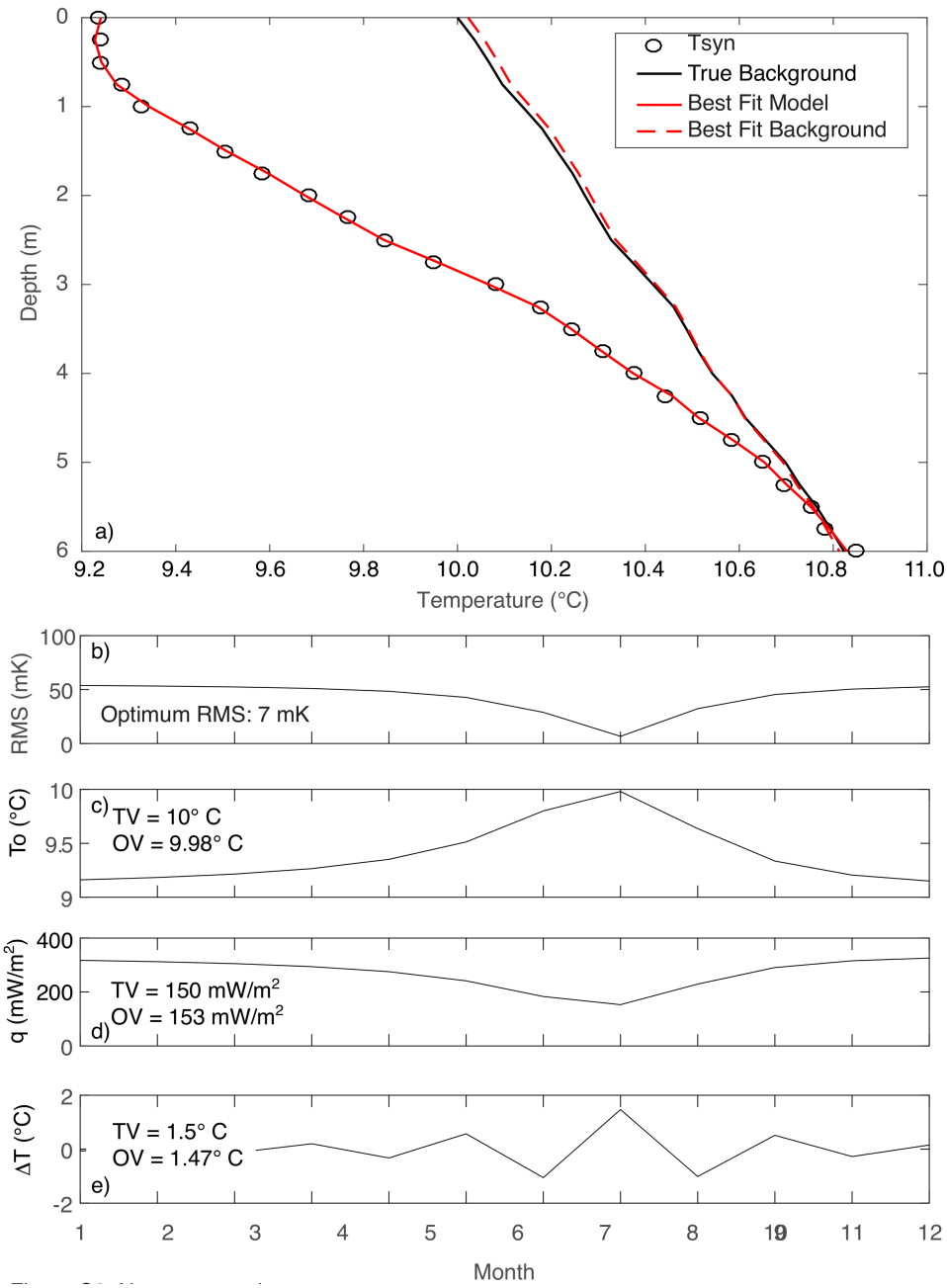


**Figure 24.** a) Synthetic temperature depth points and true background thermal parameters with their respective best fitting curves. b) Root mean square misfit, c) long-term mean BWT, d) Heat flow and e) BWT amplitude.

noise to the signal which is a generous estimate of actual measurement noise. Because Equation 35 is linear with the exception of the phase we use a linear inversion technique and iterate over the phase. Figure 24 shows the root mean square (RMS) misfit, and inverted parameters as a function of the phase. Our results show that we accurately recover the input parameters and the background heat flow to within a few percent.

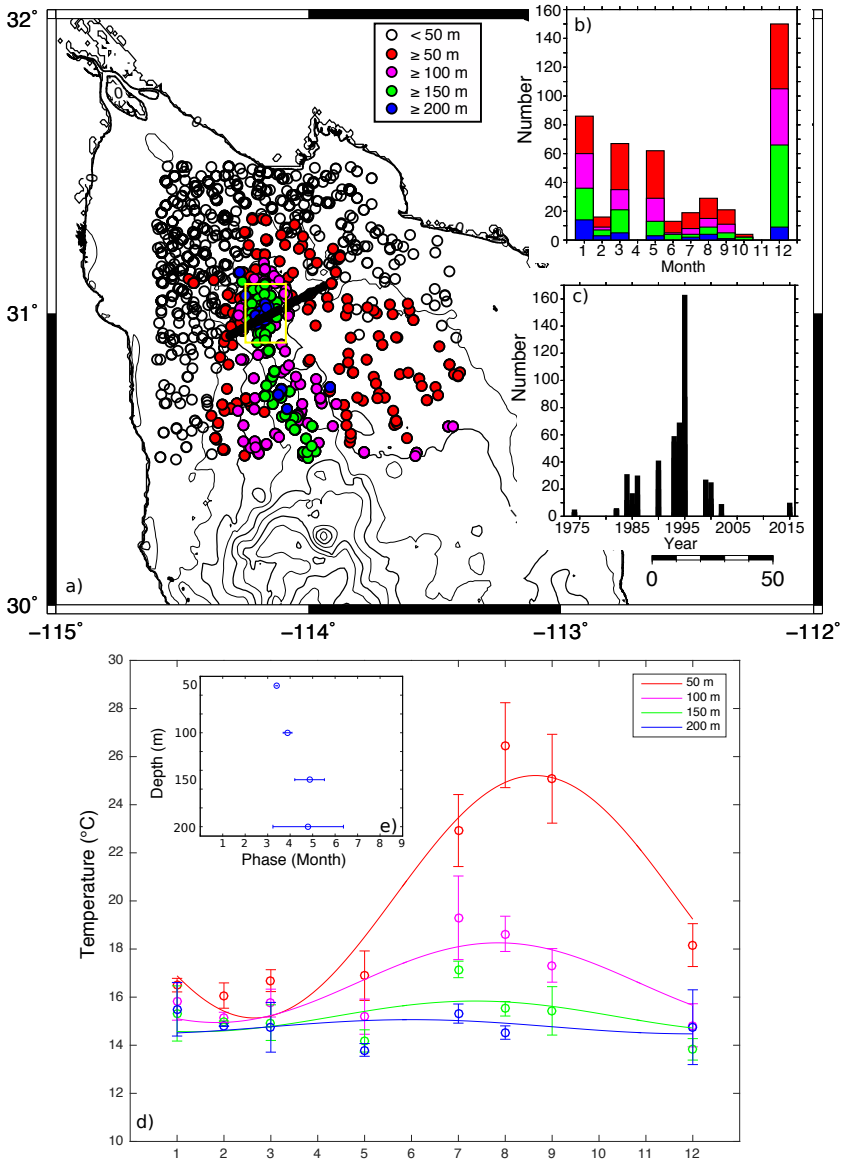


**Figure 25.** a) CTD casts in the northern Gulf of California. Black circles show heat flow measurements. Color coded circles are according to the depth. Yellow rectangle represents temperature depth profiles shown in Figure 26. b) Monthly distribution of CTD casts. Color are according to depth. c) Number of CTD casts by year. d) Average temperature-month (circles) with standard deviation for CTD casts. Curves show best fitting sinusoid with a period of one year to the average temperature. Color are according to depth. e) Phase for fitted sinusoid

### 3.1.2 CTD-casts

A challenge in interpreting heat flow data in shallow water is removing the influence of temporal variations in BWT. The shallow water depths (< 250 m) of the Wagner Basin are susceptible to large temporal variations in BWT that can produce significant source of curvature. Temperature-depth profiles are most sensitive to the last large event. Unfortunately, time-series of BWT prior

to and during the period of the experiment are not available for the northern GC. We explore the nature of BWT variations using studies of sea surface temperature (SST) and electric conductivity, temperature and depth (CTD) casts available from the NOAA database (Levitus *et al.*, 2013) and from the department of oceanography at CICESE (Godínez *et al.*, 2013).

Lavín and Marinone (2003) used satellite infrared images collected between January 1984 and December 2000 to analyze SST anomalies. Eight-day averages were combined to form monthly averages. The spatial resolution is 18 x 18 km. This analysis indicates maximum SST between July and August and minimum SST between January and March. An empirical orthogonal function analysis shows that the first mode explains 97% of the variability. The time evolution of this mode is strongly sinusoidal with an annual period due to seasonal heating and cooling combined with tidal mixing (Lavín and Marinone, 2003). The annual harmonic accounts for 95% of the SST variability in the northern GC.

Thermodynamic studies of the northern GC indicate that the water around the Wagner Basin is only weakly stratified between the surface and bottom (e.g., Montes *et al.* 2015). Mixing occurs through the combined effects of thermohaline circulation, tidal mixing and coastal upwelling (Alvarez-Borrego and Lara-Lara, 1991). Vertical mixing induced by tidal currents in the northern Gulf is strong because the length of the gulf is somewhat shorter than a half wavelength of the semidiurnal constituents therefore the gulf is almost resonant at the frequency (Argote *et al.*, 1995). These results suggest the dominant variability in bottom water is at the annual time scale.

To check this assertion, we compiled CTD casts available from the NOAA database (Levitus *et al.*, 2013) and CICESE (Godínez *et al.*, 2013). Over 1163 CTD casts exist between 1980 and 2015, though most of the casts were recorded between 1984 and 2004 (Figure 25a). We averaged temperatures at 50, 100, 150, and 200 m depth and plotted them as a function of month for all available years (Figure 25d). A sinusoid with an annual period fits the data well for all depths but amplitude and phase must decay with depth to explain the data properly, which is consistent with the physical oceanography studies previously discussed. At 200 m depth, the amplitude of the variation is small at 0.24 °C, and the root-mean-square (RMS) misfit shows little sensitivity to the phase. Variations in BWT shorter than one month produce perturbations in the sub-bottom that diffuse away at very shallow depths. For a monthly variation the fluctuation decreases to 1/e of the

BWT at a depth of approximately 0.6 m. We checked for long-wavelength variations by plotting the CTD temperatures as a function of time for depths of 150 m and 200 m. Linear trends to this data are not statistically significant. These analyses suggest that the dominant period of BWT variation is at the annual time scale and that extreme BWT temperatures are in winter and summer months, respectively.

We show the vertical temperature structure of the water column using a subset of CTDs in the immediate vicinity of Wagner Basin (Figure 25a). Water column temperature profiles based on these CTD casts vary from about 16.4 ° to 31 ° C at the surface and diminish to 13.4 ° to 16.4 °C at a depth of 200 m (Figure 26a). Figure 26a also shows the mean BWT measured at the top of the probe during each penetration plotted as a function of water depth. These values follow a depth trend similar to that observed in the CTD casts. The standard deviation of these temperatures is plotted as a function of depth (Figure 26b) and gives a rough sense of what BWT variation might be.

### 3.2 Sedimentation

In addition to fluctuation in sediment temperature by seasonal variation heat flow values are likely suppressed due to the effect of rapid sedimentation. Sedimentation can transiently depress surface heat flow until the deposited sediments are warmed to the background thermal conditions. Sediment in the northern Gulf of California reaches thicknesses of up to 7 km (Persaud *et al.*, 2003; Aragón-Arreola and Martín-Barajas, 2007; González-Fernández *et al.*, 2005; González-Escobar *et al.*, 2009). Sedimentation rates in the northern GC are not precisely known. Chronostratigraphic studies in deep ($\sim$ 4 km) boreholes drilled by PEMEX in the northwestern part of the Wagner basin suggest sediment accumulation rate of $\sim$ 1 mm yr$^{-1}$ (Aragón-Arreola and Martín-Barajas, 2007; Helenes *et al.*, 2009). Dorsey (2010) estimates an average sediment accumulation rate in the Salton Trough and NGOC of 1.9 – 2.3 mm yr$^{-1}$ based on eroded volume of rock transported by the Colorado River over the past 5 – 6 Myr. These rates might be overestimated as observations indicate large drainage networks mobilize only a fraction of the total volume of sediments produced in their catchment areas (Rodríguez-Iturbe and Rinaldo, 2001). Moreover, observations in the Laguna Salada basin, farther north, suggest the sedimentation rate is approximately 0.7 mm yr$^{-1}$ (Contreras *et al.*, 2005). We estimate the potential impact of sedimentation on heat flow values using the one dimensional advective heat transport equation,

$$\kappa \frac{\partial^2 T}{\partial z^2} = \frac{\partial T}{\partial t} + V_z \frac{\partial T}{\partial z} \tag{37}$$

where $V_z$ is the sedimentation rate.

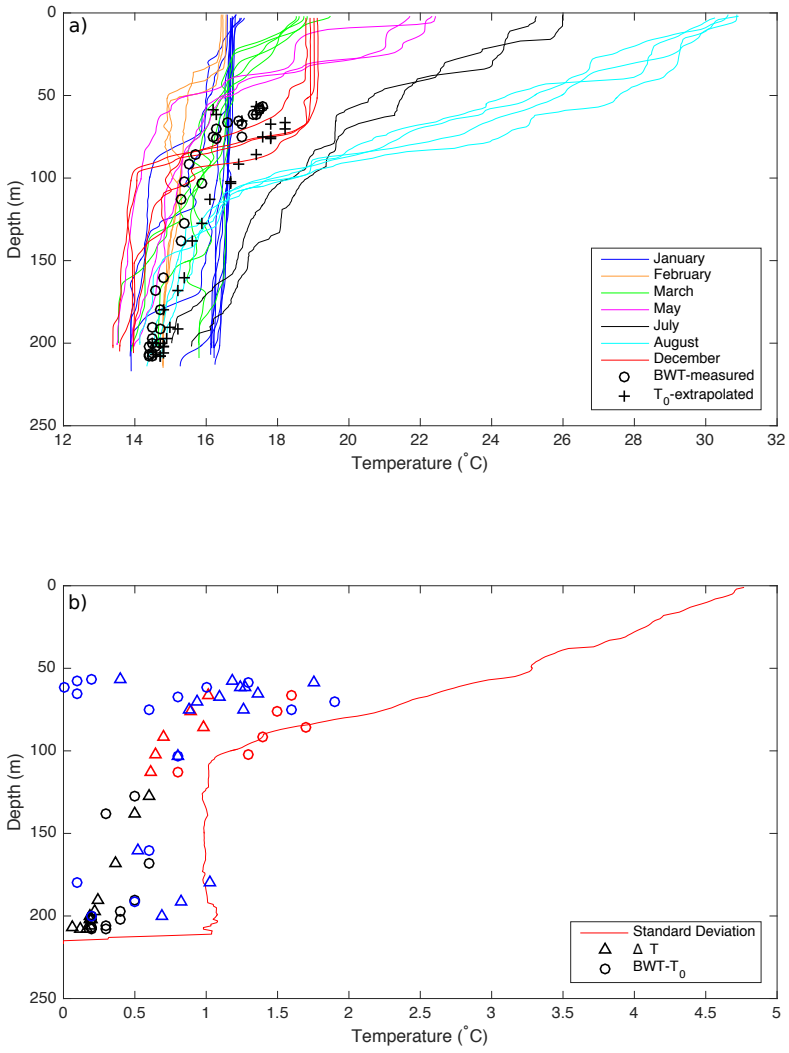


**Figure 26.** a) Temperature profiles from CTD casts in the northern Gulf of California (yellow rectangle Figure 25). Profiles are color coded by month of acquisition. Open circles show mean bottom water temperature (BWT) measured at top of the probe during each heat flow measurement (May, 2015). Crosses show seafloor temperature extrapolated from the data. b) Red line corresponds to one-standard deviation of the CTD measurements. Triangles show the best fitting amplitude of seasonal variation ($\Delta$T) to the temperature-depth profiles. Circles show the difference between the BWT and extrapolated seafloor temperature ($T_0$). Circles and triangles are color coded by geographic position, blue corresponds to the western margin, red to the eastern margin, and black to the central basin

The solution to this problem, assuming a equilibrium gradient $\Gamma_b$ throughout the subsurface at $t = 0$ is (Powell *et al.*, 1988):

$$
\begin{aligned}
T(z,t) = T_0 + \Gamma_b(z - V_z t) + \frac{1}{2}\Gamma_b \\
\Big[(z + V_z t)\exp(\frac{V_z z}{\kappa})erfc\left(\frac{z + V_z t}{2(\kappa t)^{1/2}}\right) \\
- (z - V_z t)erfc\left(\frac{z - V_z t}{2(\kappa t)^{1/2}}\right).
\end{aligned}
\tag{38}
$$

The corresponding gradient is:

$$
\begin{aligned}
\Gamma(z,t) = \frac{\partial T(z,t)}{\partial z} = \Gamma_b + \frac{1}{2}\Gamma_b\Big[ - erfc\left(\frac{z - V_z t}{2(\kappa t)^{1/2}}\right) \\
- \frac{(z + V_z t)}{(\pi\kappa t)^{1/2}}\exp\left(\frac{V_z z}{\kappa}\right)\exp\left(-\left(\frac{z + V_z t}{2(\kappa t)^{1/2}}\right)^2\right) \\
+ \frac{(z - V_z t)}{(\pi\kappa t)^{1/2}}\exp\left(-\left(\frac{z - V_z t}{2(\kappa t)^{1/2}}\right)^2\right) \\
+ \left(1 + \frac{V_z z}{\kappa} + \frac{v^2 t}{\kappa}\right)\exp\left(\frac{V_z z}{\kappa}\right) erfc\left(\frac{z + V_z t}{2(\kappa t)^{1/2}}\right)\Big]
\end{aligned}
\tag{39}
$$

Figure 27 shows the effect of 1-D sedimentation on the thermal gradient as a function of sedimentation rate and basin development timescale. The disturbance on the thermal gradient is negligible for smaller times but grow as the sedimentation event increases.

Assuming a sedimentation rate of 1-2 mm yr$^{-1}$ over the past 5-6 Myr results in a heat flow depression of approximately 40%-50%.

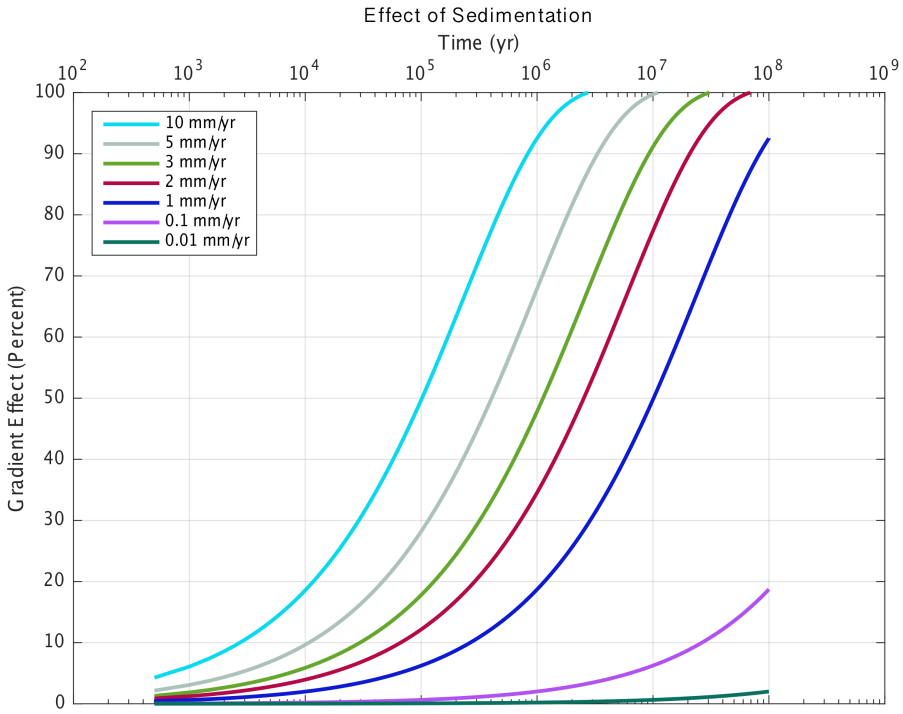


**Figure 27.** Effects of sedimentation on the thermal gradient at the Earth's surface using Equation 37 using a thermal diffusivity of $1mm^2s^{-1}$. The different curves represent the sedimentation rates.

# Chapter 4. Results

## 4.1 Heat flow across the Wagner Basin

Here we present 33 heat flow measurements (Table 2) from the Wagner basin collected on the R/V Alpha Helix in 2015 (Figure 28) as discussed in Chapter 2. Of the 33 measurements, 5 are partial penetrations that do not yield reliable values of heat flow. Heat flow measurements were made with a FIELAX multi-penetration heat flow probe based on the violin bow design that provides both the mechanical robustness to withstand repeated insertions and withdrawals from the sediment, and sensitivity needed to make highly accurate measurements. The thermistor string

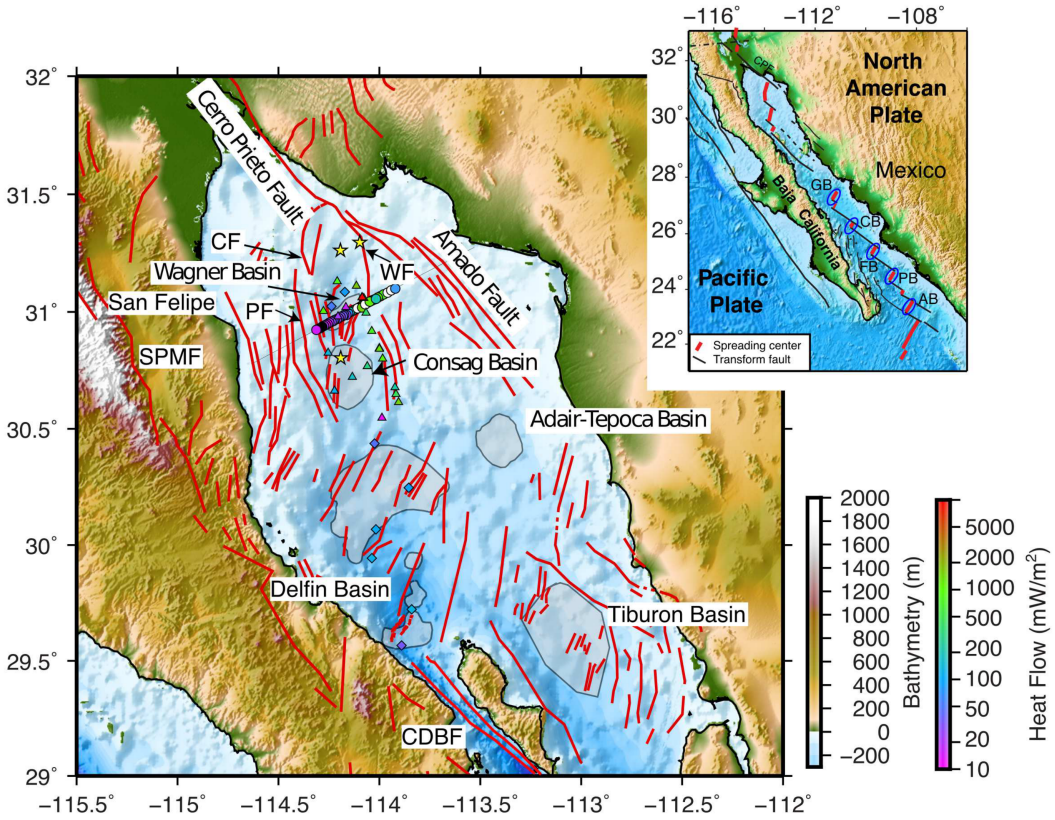


**Figure 28.** Elevation and bathymetry map of the northern Gulf of California showing the distribution of rift basins and faults in the region (red lines). Fault traces are from (Persaud *et al.*, 2003; Aragón-Arreola and Martín-Barajas, 2007; Plattner *et al.*, 2007; González-Escobar *et al.*, 2009; Martín-Barajas *et al.*, 2013). Circles are new heat flow measurements collected for this study; Triangles and squares represent heat flow data from Prol-Ledesma *et al.* (2013) and Henyey and Bischoff (1973) respectively; circle color is proportional to heat flow magnitude, white circles show the partial penetrations. Black line across the Gulf of California is the location of a regional seismic reflection line collected by PEMEX and processed by Aragón-Arreola and Martín-Barajas (2007). Stars represent boreholes drilled by PEMEX. Abbreviations: WF = Wagner Fault; PF = Percebo Fault; CF = Consag Fault; SPMF = San Pedro Mártir Fault; CDBF = Canal de Ballenas Fault; Southern basins on inset map: AB = Alarcón basin; PB = Pescadero basin; FB = Farallon basin; GB = Guaymas basin.

is 6-m long and houses 22 thermistors of 1 mK precision. Other parameters measured by the system include time, pressure (depth), water temperature, tilt, and a stable reference resistance. The procedure to obtain these parameters out of the measurements were discussed in Chapter 2.

Heat flow measurements are collocated with seismic reflection profile 5037 (Figure 28), acquired by PEMEX and processed by Aragón-Arreola and Martín-Barajas (2007). Echo sounder profiles were also collected during the cruise. Spacing between each measurement is nominally 1 km but decreases to approximately 500 m around targets of interest (Figure 28).

All heat flow determinations are processed based on the formulation described by Hartmann and Villinger (2002) also described in Chapter 2 of this dissertation. Probe insertion into the sediment generates a frictional heat pulse whose decay is described by a cylindrical source. I compute equilibrium temperatures by fitting the time series to a cylindrical decay curve (see Equation 16) over a 10 min time period and extrapolating to infinite time. After the initial 10 min time period a 20 s calibrated heat pulse of 1 kJ $m^{-1}$ (Lister, 1979) is generated and the temperature decay is used to estimate the in situ thermal conductivity. The mean thermal conductivity over the transect is 1.16 W $m^{-1}$ $K^{-1}$ and the standard deviation of the measurements is 0.28 W $m^{-1}$ $K^{-1}$. Moreover, thermal conductivity-depth profiles generally show a slight increase of this material parameter with depth (Figure 29).

The temperature-depth profiles (Figure 30) show two conspicuous features. The first feature is the large thermal gradients and the second is curvature in the shallow sub-bottom profiles. Also note the short wavelength variability in the gradients associated with the eastern Wagner basin. Possible sources of curvature include the effects of bottom water temperature variation (BWT), bathymetry and the advective transport of heat caused by sedimentation (see Chapter 3) and fluid flow (see below).

**Table 2.** Heat flow data across the Wagner basin

| Penetration | Longitude (deg) | Latitude (deg) | Water Depth (m) | BWT (°C) | To± 2$\sigma$ (°C) | $\Delta$T± 2$\sigma$ (°C) | Phase (Month) | Heat flow ± 2$\sigma$ (mW m$^{-2}$) |
|---|---|---|---|---|---|---|---|---|
| HF007P05 | -114.3112 | 30.9234 | 66 | 16.65 | 18.2± 0.16 | -1.01± 0.2 | 12 | 326± 56 |
| HF007P04 | -114.3022 | 30.9277 | 76 | 16.27 | 17.84± 0.14 | -0.89± 0.2 | 9 | 223± 48 |
| HF007P03 | -114.2929 | 30.9320 | 85 | 15.69 | 17.36± 0.13 | -0.98± 0.19 | 10 | 201± 44 |
| HF007P02 | -114.2835 | 30.9364 | 92 | 15.45 | 16.91± 0.12 | -0.7± 0.16 | 10 | 237± 45 |
| HF007P01 | -114.2747 | 30.9405 | 102 | 15.42 | 16.66± 0.11 | -0.64± 0.15 | 9 | 151± 34 |
| HF006P08 | -114.2653 | 30.9448 | 113 | 15.34 | 16.12± 0.1 | -0.61± 0.18 | 1 | 182± 38 |
| HF006P07 | -114.2557 | 30.9488 | 127 | 15.39 | 15.87± 0.08 | -0.6± 0.16 | 1 | 123± 29 |
| HF006P06 | -114.2468 | 30.9535 | 138 | 15.29 | 15.57± 0.07 | -0.5± 0.14 | 1 | 121± 25 |
| HF006P05 | -114.2373 | 30.9572 | 163 | 14.61 | 15.24± 0.05 | -0.37± 0.13 | 12 | 106± 20 |
| HF006P04 | -114.2279 | 30.9617 | 190 | 14.52 | 15.01± 0.05 | 0.24± 0.11 | 1 | 97± 16 |
| HF006P03 | -114.2197 | 30.9656 | 197 | 14.46 | 14.92± 0.05 | 0.21± 0.1 | 1 | 87± 16 |
| HF006P02 | -114.2093 | 30.9700 | 202 | 14.44 | 14.81± 0.05 | 0.19± 0.11 | 1 | 86± 14 |
| HF006P01 | -114.2004 | 30.9742 | 206 | 14.45 | 14.79± 0.06 | 0.18± 0.09 | 1 | 83± 16 |
| HF005P12 | -114.1916 | 30.9784 | 208 | 14.45 | 14.73± 0.06 | 0.17± 0.1 | 1 | 86± 15 |
| HF005P11 | -114.1811 | 30.9825 | 208 | 14.43 | 14.65± 0.05 | 0.12± 0.1 | 1 | 94± 14 |
| HF005P10 | -114.1731 | 30.9862 | 207 | 14.42 | 14.63± 0.07 | 0.06± 0.09 | 1 | 99± 18 |
| HF005P09 | -114.163 | 30.9860 | 200 | 14.5 | 14.75± 0.06 | 0.18± 0.1 | 1 | 93± 18 |
| HF005P08 | -114.1539 | 30.9945 | 202 | 14.63 | 14.78± 0.06 | 0.18± 0.09 | 1 | 111± 19 |
| HF005P07 | -114.1442 | 30.9992 | 200 | 14.66 | 14.46± 0.15 | -0.69± 0.36 | 8 | 388± 54 |
| HF005P06 | -114.1349 | 31.0034 | 191 | 14.71 | 15.15± 0.05 | 0.82± 0.22 | 12 | 440± 31 |
| HF005P05[1] | -114.1259 | 31.0072 | 180 | 14.72 | | | | |
| HF005P04 | -114.1168 | 31.0111 | 160 | 14.75 | 15.37± 0.07 | -0.52± 0.17 | 12 | 1005± 48 |
| HF008P02[1] | -114.08425 | 31.0200 | 103 | 15.91 | | | | |
| HF004P04 | -114.0518 | 31.0415 | 75 | 16.2 | 17.75± 0.12 | -1.26± 0.21 | 1 | 774± 46 |
| HF010P03 | -114.048 | 31.0445 | 75 | 17 | 17.62± 0.12 | 0.88± 0.30 | 11 | 1570± 97 |
| HF004P03 | -114.0426 | 31.0459 | 70 | 16.29 | 18.22± 0.13 | -0.94± 0.23 | 12 | 1581± 74 |
| HF004P01 | -114.0233 | 31.0533 | 65 | 16.93 | 17.02± 0.16 | -1.36± 0.35 | 10 | 981± 57 |
| HF003P01 | -114.0166 | 31.0564 | 67 | 16.96 | 17.78± 0.05 | 1.09± 0.21 | 1 | 637± 30 |
| HF008P09[1] | -114.0065 | 31.0621 | 62 | 17.23 | | | | |
| HF008P010 | -113.9951 | 31.0662 | 62 | 17.4 | 17.41± 0.06 | -1.27± 0.23 | 9 | 913± 31 |
| HF008P011[1] | -113.9776 | 31.0745 | 59 | 17.53 | | | | |
| HF008P012[1] | -113.9592 | 31.0828 | 58 | 17.52 | | | | |
| HF008P013 | -113.9406 | 31.0912 | 57 | 17.62 | 17.43± 0.27 | 0.4± 0.4 | 8 | 602± 95 |

[1]Partial penetration that does not yield a reliable model.

Optimum heat flow values are shown in Figure 32 and in Table 2. Uncertainties represent the 95% confidence interval. Based on the inverted parameters (Figure 31) and the heat flow I divided our transect into three regimes: the western portion with heat flow slightly higher than the central basin where heat flow is relatively consistent and the eastern portion where heat flow is relatively high and variable. Water depths associated with the western side range between 66 and 113 m, those in the central portion are between 127 and 202 m and those on the eastern side range

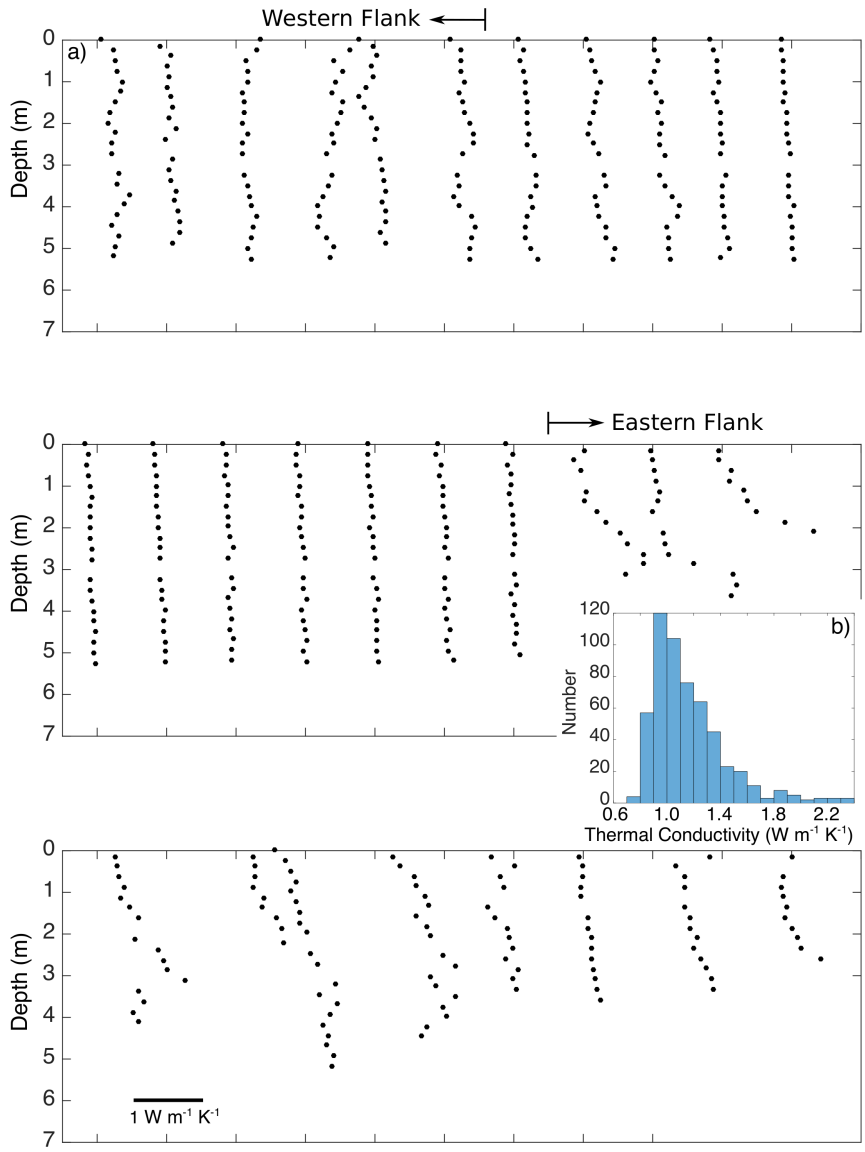


**Figure 29.** Thermal conductivity-depth profiles across the Wagner rift of the Gulf of California. Profiles were obtained using a Fielax system of 22 thermistors along a thermistor string 6 m long. Thermistor 10 was removed from the profiles because of thermal perturbations caused by a mount point of the probe. I assumed conductivities for penetrations 25 and 29 based on neighboring profiles and are not shown.

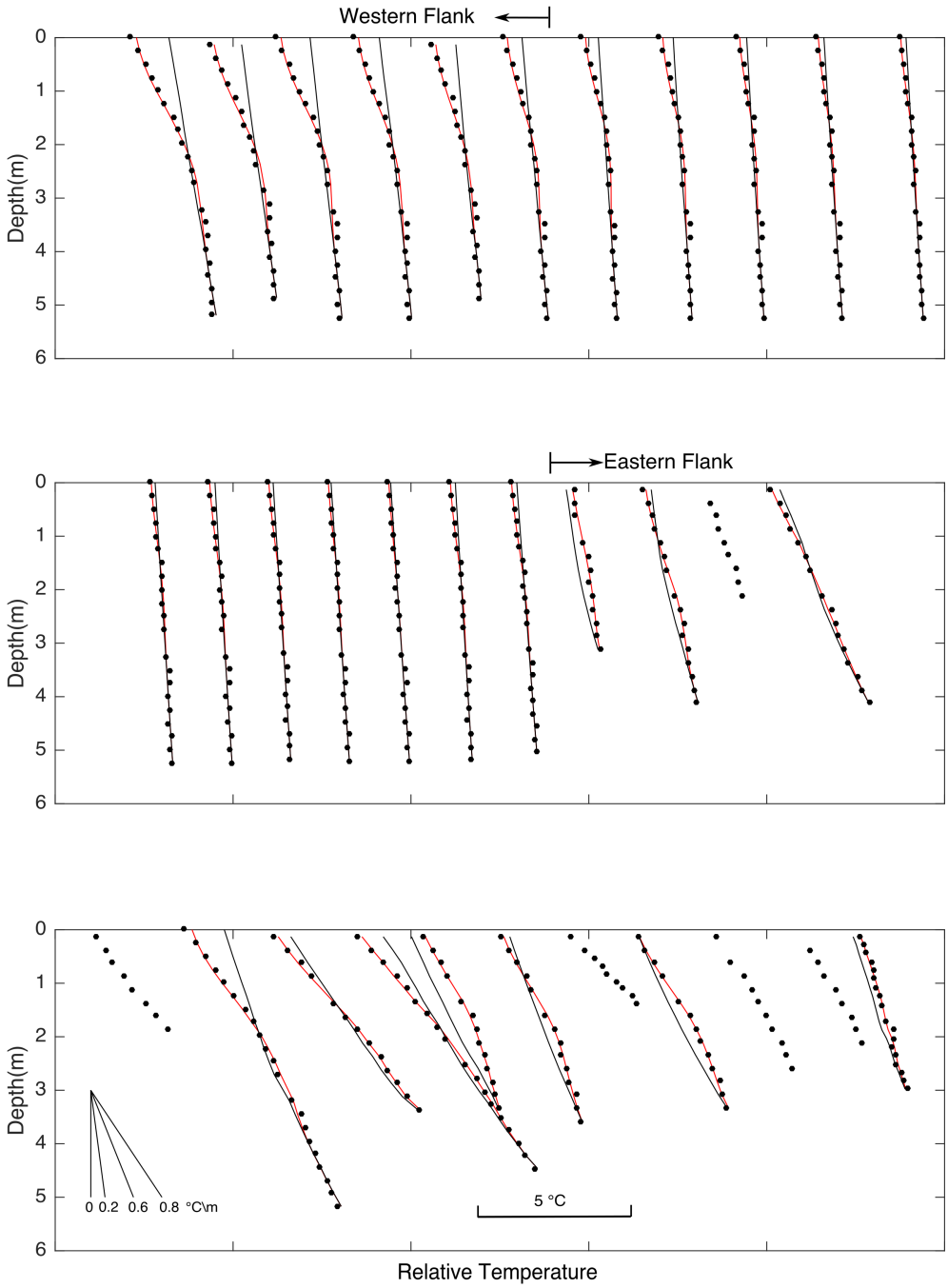


**Figure 30.** Temperature-depth profiles across the Wagner rift of the Gulf of California. Profiles were obtained using a Fielax system of 22 thermistors along a thermistor string 6 m long. Thermistor 10 was removed from the profiles because of thermal perturbations caused by a mount point of the probe. Best fitting curve from the inversion model is shown in red. Black curve represents background thermal regime. For the partial penetrations the poor model fit precludes the interpretation of these measurements.

between 200 and 57 m. The relatively small uncertainties associated with measurements in the central Wagner basin reflect the goodness of fit, whereas the large uncertainties associated with measurements on the western and eastern portions of the transect basin indicate generally poorer

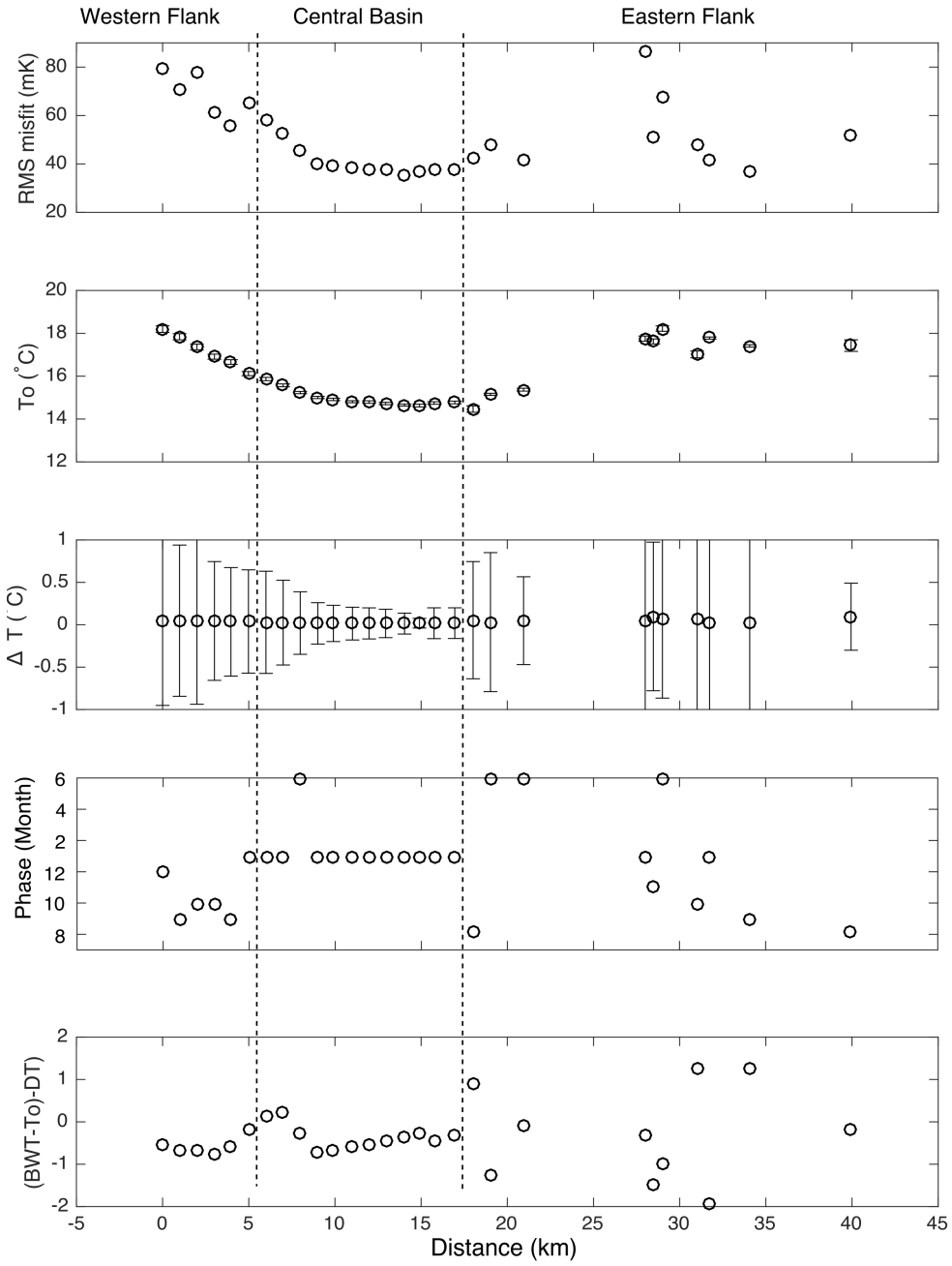


**Figure 31.** Parameters resulting from inversion scheme as a function of distance. a) RMS misfit between the observed and predicted temperature. b) Long term seafloor temperature ($T_0$). Uncertainties show 95% confidence interval. c) Optimum amplitude of seasonal variation ($\Delta$T) to the temperature-depth profiles with 95% confidence interval. d) Optimum phase. e) Circles show the difference between the BWT, extrapolated seafloor temperature ($T_0$) and amplitude of seasonal variation ($\Delta$T). Dashed lines show the limits of geographic position, corresponding to the western, eastern margin, and the central basin.

fits. The mean heat flow across the central basin is 99 $\pm$ 14 mW m$^{-2}$. The estimated magnitude of bottom water variation across the basin floor is 0.5 °C, leading to an approximately 10% change in the gradient, well within the standard deviation of the data.

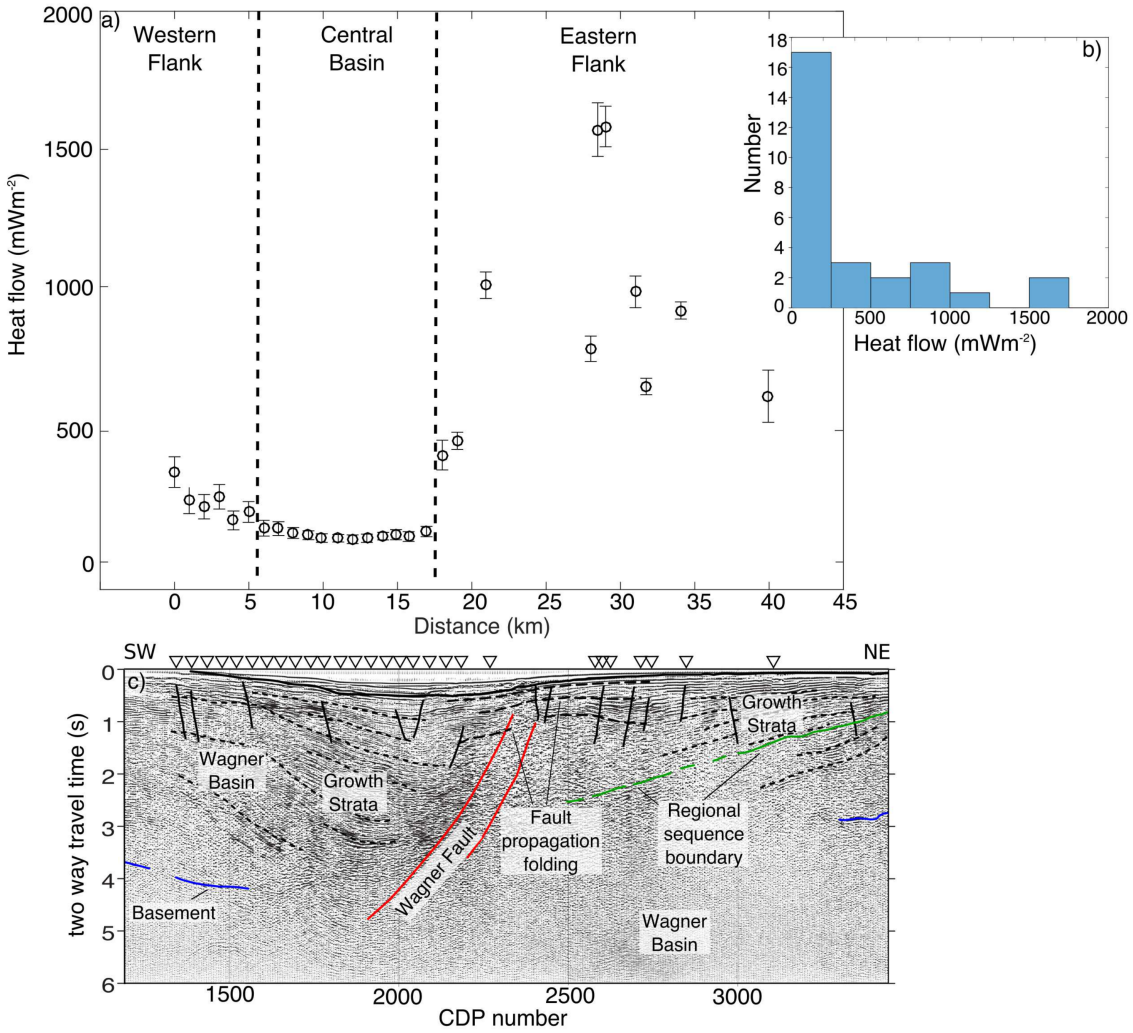


**Figure 32.** a) Heat flow values across the Wagner basin. Error bars show 95% confidence interval. b) Seismic reflection profile (modified from Aragón-Arreola and Martín-Barajas (2007)) Red lines show Wagner fault. Black lines show faults across the basin, blue the acoustic basement, green the regional sequence boundary and triangles show heat flow measurements.

## 4.2 Advective fluid flow

Heat flow measurements on the eastern and western sides of the Wagner basin show higher and more variable heat flow than in the central basin. The very high and variable heat flow values, especially that associated with the eastern basin, are difficult to interpret with the available information. If conductive heat transfer is responsible for the high and variable heat flow, it would need an extra source of heat that is shallow and variable. This region sits on top of a regional low shear-wave velocity anomaly (Di Luccio *et al.*, 2014; Persaud *et al.*, 2015, 2016), which might be the product of a thermal anomaly but the source is too deep and regional to account for the horizontal gradient in heat flow between the central and eastern portions of the Wagner basin and we see no

evidence for a shallow conductive heat source in the seismic reflection profile. This rationale leads us towards an interpretation of advective heat transfer. One possibility for advective heat transfer is fluid flow focused along permeable pathways such as faults. Indeed, the seismic reflection profile shows numerous faults that can be traced much closer to the seafloor in the eastern and western portions of the Wagner basin than in the central part of the basin and fault offsets are observed in the eastern portion of the basin (Persaud *et al.*, 2003). With this scenario the variability may be explained with alternating regions of fluid discharge or recharge or flow in and out of the plane of the transect.

An alternative scenario is fluid seepage caused by transient flow from arrested compaction or asymmetric loading that leads to two-dimensional flow. The sediments comprising the Wagner basin generally consist of fine sands and silt that have relatively high permeability making the development of overpressure unlikely. Moreover, asymmetric loading of the sediments is not observed. These arguments cause us to discount fluid seepage as a source of advective heat transfer.

It is straight forward to show that sedimentation and consolidation are unlikely to drive significant flow across the seafloor by considering an upper bound on the steady state dewatering flux results from assuming fully drained burial. Assuming a porosity-depth function such as Athy's law (Athy, 1930)

$$\phi(z) = \phi_0 \exp(-\lambda z) \tag{40}$$

where $\phi$ is the surface porosity and $\lambda$ is the compaction factor (a quantity in the order of $10^{-2}m^{-1}$). The change in porosity with time is given by,

$$\frac{\partial \phi(z)}{\partial t} = -\phi_0 \lambda \exp(-\lambda z) = -\lambda \phi \tag{41}$$

where $\frac{\partial \phi(z)}{\partial t} = s$, the sedimentation rate. The volume flux can be expressed by

$$Q(z) = \int_0^z \frac{\partial \phi}{\partial t} dz' = \int_0^z -\lambda \phi(z) s dz' = s\phi_0(\exp(-\lambda z) - 1) \tag{42}$$

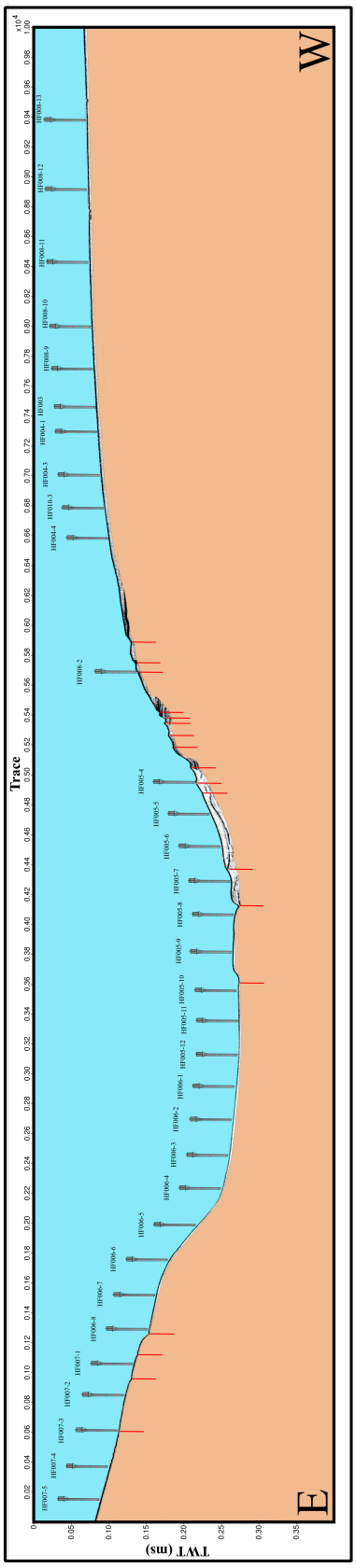


**Figure 33.** Echo sound profile across the Wagner basin with heat flow measurement sites. Red lines show faults.

Because $\exp(-\lambda z) - 1$ is less than 1, the sedimentation rate

$$Q(z) < s. \tag{43}$$

Note that assuming is Darcy's law applies here, sediment compacts according to Equation 40, and aquathermal pressuring and clay dehydration can be neglected. As compaction drives fluid upward relative to the local sediments, this flow is offset by subsidence. Thus, although fluids are moving up relative to the sediments, they are moving downward relative to the seafloor.

Based on the previous results, focused fluid flow along faults is more likely and leads to the relatively larger values and variability in heat flow over short spatial scales as observed in the eastern part of the survey area. This interpretation is consistent with the seismic reflection profile showing numerous faults that can be traced much closer to the seafloor than in the central part of the basin. Indeed, fault offsets are observed at the seafloor (Persaud *et al.*, 2003) and can be observed in the echo sound profile across the Wagner basin (Figure 33). Moreover, conductive heat transfer as a source of the large measurement-to-measurement variability can be ruled out, because such a source would need to be very shallow and there is no evidence of this in the seismic reflection profile. To explore the implications of this conjecture, a one-dimensional steady-state model of the vertical flow through a porous media is used based on the following equation:

$$\frac{\partial^2 T}{\partial z^2} - \frac{\phi \rho_w c_w}{k_e} V_z \frac{\partial T}{\partial z} = 0 \tag{44}$$

where $\phi$ is porosity, $k_e$ is the effective thermal conductivity, $\rho_w c_w$ is the heat capacity of water, and $V_z$ is the mean vertical fluid velocity. For boundary conditions we assumed an isothermal seafloor $T(z = 0) = T_0$, and a constant thermal gradient, $\Gamma_L$ at depth $L$, the base of the system. The solution for this model is,

$$T(z) = T_0 + \frac{\Gamma_L L \exp(\frac{\beta}{L} z) - 1}{\beta \exp(\beta)} \tag{45}$$

where $\beta$ is the Peclet number given by,

**Table 3.** Parameter values for Porous Flow Calculation

| Parameter | Value |
|---|---|
| Porosity, $\phi$ | 0.2 |
| Fluid density, $\rho_w$ | 1000 kg m$^{-3}$ |
| Specific heat of fluid, $c_w$ | 4186 J kg$^{-1}$ K$^{-1}$ |
| Effective thermal conductivity, $k_e$ | 2 W m$^{-1}$ K$^{-1}$ |

$$\beta = \frac{\phi \rho_w c_w V_z L}{k_e} \tag{46}$$

From Equation 40 an analytical expression for heat flow by taking the derivative and multiplying through by $k_e$ is obtained,

$$k_e \frac{\partial T}{\partial z} = \frac{k_e \Gamma_L \exp(\frac{\beta}{L} z)}{\exp(\beta)} \tag{47}$$

This expression for surface heat flow, $q_0$, at $z = 0$ is evaluated, and set the product $k_e \Gamma_l$ equal to the basal heat flow, $q_b$, we obtain,

$$q_b = q_0 \exp(\beta) \tag{48}$$

In this way, $q_0$, can be expressed as a multiple of $q_b$, and with this ratio known, $V_z$ can be expressed as a function of $L$, as follows:

$$V_z(L) = \frac{k_e}{\phi \rho_w c_w L} ln \left( \frac{q_b}{q_0} \right) \tag{49}$$

Figure 34 shows the relationship between $V_z$ and $L$ appropriate for the western and eastern flanks of the Wagner basin, with $q_0/q_b$ = 1.5 and 6, respectively. Here, it is assumed that the heat flow in the central graben of the Wagner basin corresponds with the background heat flow of the system $q_b$. Material parameters for this calculation are given in Table 3.

Faults in the western and eastern flanks are observed to depths of $\sim$ 1.75 km, which is used as estimate of $L$. Below this depth the Darcy velocity is relatively constant. This calculation leads to flow rate estimates of approximately 2 and 8 cm yr$^{-}1$ for the western and eastern flank, re-

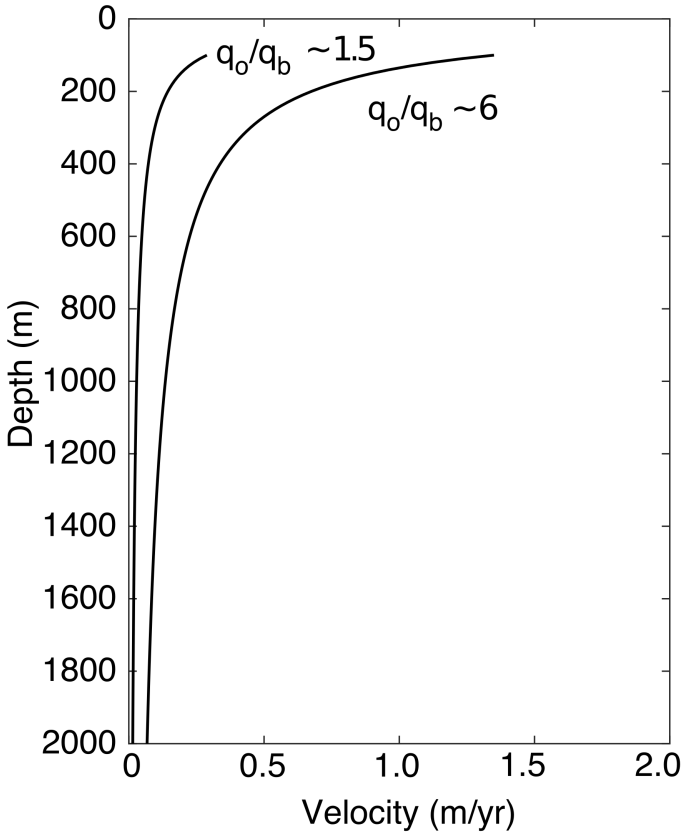


**Figure 34.** Darcy velocity as a function of flow length, $L$ for different ratios of the basal heat flow, $q_b$, and the observed heat flow $q_0$.

spectively. This model indicates that the larger heat flow observed along the eastern margin of the Wagner basin could be attributed to greater flow rates, larger values of L, greater permeability along the fault conduits, larger basal heat flux, or a combination of these factors. For example, if the flow velocity on the eastern flank is the same as that on the western flank, flow would need to originate at a depth of about 8.5 km. Because the horizontal variability (several km) is proportional to the source depth in steady state an L of 8.5 km may be too deep. The magnitude of flow also suggests that the heat source will be depleted over time. Both of these observations may be suggesting that this flow system is transient. Without independent evidence, such as geochemical indicators of fluid flow through the seafloor, our model is under constrained and necessarily non-unique.

### 4.3 Continental rupture ?

A central question regarding the Wagner basin is whether continental rupture is complete and seafloor spreading has started. Similar to the Salton Trough and the Guaymas basin (Fuis *et al.*, 1984; Han *et al.*, 2016; Kluesner and Lonsdale, 2008), the crust has a stratified structure consisting of sediments and metasediments overlying a layer of felsic and/or gabbroic material. The gabbroic material flows upwards and where the hydrostatic pressure equalizes with their surroundings, they flow out horizontally as sills. We consider the continental crust to be ruptured if gabbroic dikes reach the base of the metasediment layer. We address this question using a two-pronged approach: first, we use isostatic considerations to make inferences about the crustal structure, and then use a thermal model to test if the heat flow data is consistent with diking at the base of the upper crust.

Because of the high heat flow and small free-air gravity anomalies associated with the Wagner basin we assume it is in isostatic equilibrium. Our inferred crustal geometry is shown in Figure 35a. For this situation seafloor depth can be expressed as (e.g., Lachenbruch and Morgan 1990),

$$d = \frac{\rho_a - \rho_{uc}}{\rho_a - \rho_w} L_{uc} + \frac{\rho_a - \rho_{lc}}{\rho_a - \rho_w} L_{lc} - \frac{\rho_a}{\rho_a - \rho_w} H_0 \tag{50}$$

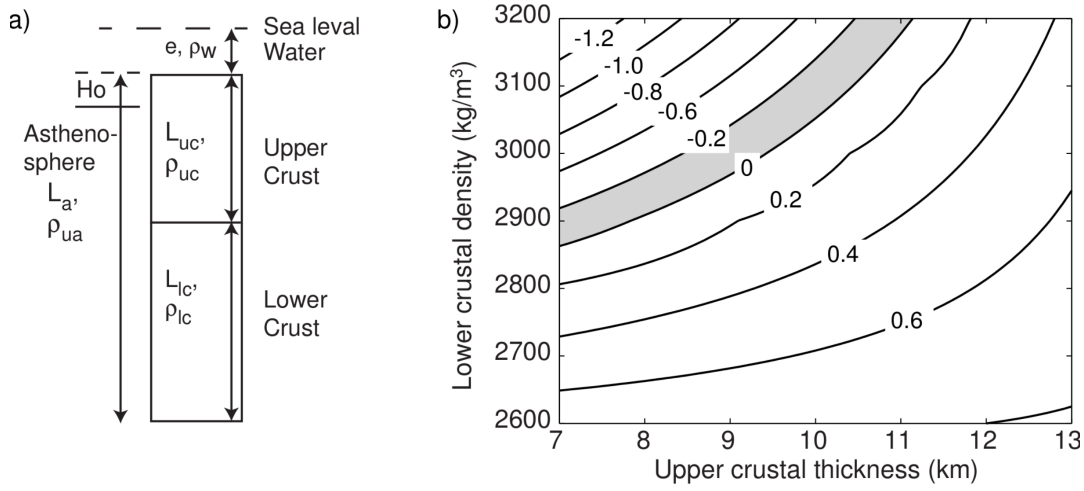


**Figure 35.** Isostatic model for the Wagner basin. a) Schematic representation of the crustal comprising the Wagner basin. b) Predicted bathymetry/elevation in km for the Wagner basin as a function of lower crustal density and upper crustal thickness. In the diagram the upper crustal density is taken as 2550 kg $m^{-3}$ and the total crustal thickness is 15 km (Lewis *et al.*, 2001). Shaded are shows permissible combinations of lower crustal density and upper crustal thickness.

where $\rho_a$, $\rho_u c$, $\rho_l c$, and $\rho_w$ are the densities of the asthenosphere, the upper crust, the lower crust, and water, respectively. $L_u c$ and $L_l c$ are the thicknesses of the upper and lower crust and $Ho$ is the buoyant height of sea level, taken to be 2.6 km based on the average depth of ridges and an asthenospheric density of 3200 kg m$^{-3}$ (e.g., Lachenbruch and Morgan 1990). Sediment is seismically imaged to at least 7 km (González-Escobar *et al.*, 2010) and receiver functions indicate that the total crustal thickness is 15 km (Lewis *et al.*, 2001). A gravity model across the northern GC in the region of the Wagner basin shows an upper crust of $\sim$ 8 km with an average density of 2550 kg m$^{-3}$ (Couch *et al.*, 1991). This density is consistent with density logs from nearby boreholes that extend to depths of 4 km or more, and which show a compaction trend suggesting that the maximum sediment density is no more than approximately 2500 kg m$^{-3}$ (Pacheco *et al.*, 2006). The gravity model suggests a metasedimentary lower crust with a density of 2630 kg m$^{-3}$ and is consistent with a similar gravity model over the Salton Trough (Fuis and Kohler, 1984).

Figure 35b shows the isostatic seafloor depth as a function of upper crustal thickness and lower crustal density for a sediment density of 2550 kg m$^{-3}$. If continental rupture has occurred then the lower crust would have a density between 2900 and 3000 kg m$^{-3}$, consistent with a mafic lower crust, and require a sediment thickness between $\sim$ 8 and 8.5 km as indicated by point A on the figure. This thickness is consistent with gravity models and indicates that the observed bathymetry is consistent with a gabbroic lower crust, and that a felsic layer in the lower crust is not required. However, a gabbroic lower crust could also be due to underplating.

We now investigate whether the heat flow data is consistent with gabbroic dikes through the lower crust or underplating at the base of the crust using the approach of Lachenbruch *et al.* (1985). They developed one-dimensional steady-state thermal models of extension to test whether continental rupturing had completed in the Salton Trough.

In these models, extension is accompanied by sedimentation at rate $s$, and either diking or underplating at rate $b$. The crustal thickness $a$, satisfies the following differential equation in which the first term on the right represents the rate of crustal thinning caused by extension and the second and third terms are the rates of thickening by sedimentation and under plating, respectively (Lachenbruch *et al.*, 1985),

$$\frac{da}{dt} = -\epsilon a + s + b \tag{51}$$

where $\epsilon$ is the strain rate. Assuming steady state, Equation 51 reduces to,

$$a = S + B \tag{52}$$

where $S$ is the portion of the crust whose thinning is compensated by sedimentation and $B$ is the portion compensated by underplating. Even if varies with time and horizontal position, $S$ and $B$ will remain constant as long as the accumulation rates remain proportional to strain rate (Lachenbruch *et al.*, 1985).

Lachenbruch *et al.* (1985) parameterized their model in terms of the strain rate and normalized sedimentation rate, $S'$, defined as the ratio of sedimentation rate to combined rate of sedimentation and under plating,

$$S' = \frac{S}{S + B} \tag{53}$$

Based on the isostatic result above $S'$ is approximately 0.5. Assuming rifting has occurred over the past 6 Myr with a total orthogonal offset of $\sim$ 255 km (Oskin *et al.*, 2001), the resulting strain rate of about $1 \times 10^{-15}$ $s^{-1}$ for the underplating model is calculated after:

$$\epsilon = \frac{v(t)}{L_0} \tag{54}$$

where $v(t)$ represents the speed at which the ends are moving away from each other and $L_0$ is the original length.

With these parameters we compute the geotherm due to underplating (Figure 36a) using following Equations in Lachenbruch *et al.* (1985).

$$\frac{\theta}{\theta_a} = \frac{erf(P/\sqrt{2})(\xi - \phi) + erf(P/\sqrt{2}\phi)}{erf(P/\sqrt{2})(1 - \phi) + erf(P/\sqrt{2}\phi)} \tag{55}$$

where $\xi = z/a$, is dimensionless independent variable, $\phi$ the dimensionless sedimentation rate and $P$ the Peclet number given as:

$$P^2 = \frac{a^2}{\kappa}\epsilon \tag{56}$$

with $a$ being the crustal thickness.

Lachenbruch *et al.* (1985) uses two different boundary conditions: First, a constant boundary temperature:

$$\theta = \theta_a \qquad z = a \tag{57}$$

and second to specify the conductive heat flux from the mantle a heat balance boundary condition. In Equation 55 the heat released at the base of the crust by the underplated magma is modeled as a plane source with a discontinuity in conductive heat flow. I assume the base of the crust is kept isothermal at the gabbro solidus temperature of $\theta_a$= 1010°C. Note that this condition is not contingent on the heat flow entering from the mantle.

In the alternative scenario, complete rupturing of the continental lithosphere implies that the dikes cut through the lower crust reaching the bottom of the sediments (Figure 36b). In this case the geotherm is calculated using Equation 58 in Lachenbruch *et al.* (1985).

$$\theta(\xi) = \theta(\phi)\frac{erf(P/\sqrt{2})(\xi - \phi)}{erf(P/\sqrt{2})\phi} \qquad 0 < \xi < \phi \tag{58}$$

$$\theta(\xi) = \theta(\phi) + [\theta_i(\phi) - \theta(\phi)](1 - \frac{cosh(P(1-\xi))}{cosh(P(1-\phi)} - \frac{sinh(P(\xi-\phi))}{sinh(P(1-\phi))}[1 - sech(P(1-\phi))]) + \frac{sinh(P(\xi-\phi))}{sinh(P(1-\phi))}[\theta_a - \theta(\phi) - 2aG_m(1-\phi)] + 2aG_m(\xi-\phi) \qquad \phi < \xi < a \tag{59}$$

$$\theta(\phi) = \left(\frac{\pi}{2}\right)^{1/2} erf\left(\frac{P}{\sqrt{2}}\phi\right) tanh(P(1-\phi))(tanh(P(1-\phi)) + \left(\frac{\pi}{2}\right)^{1/2} erf\frac{P}{\sqrt{2}}\phi)^{-1} (\theta_i(\phi)\left[\frac{cosh(P(1-\phi)) - 1}{sinh(P(1-\phi))}\right] + \frac{1}{sinh(P(1-\phi))}) [\theta_a - 2aG_m(1-\phi)] + \frac{2aG_m}{P} \qquad \theta(\phi) at \xi = \phi \tag{60}$$

with

$$\theta_i(\phi) = \theta_m(a\phi) + f\frac{L}{C} \tag{61}$$

and

$$\theta_i = \theta_i(\phi) + G_m a(\xi - \phi) \tag{62}$$

where $\theta_m$ is the adjusted basalt solidus temperature, $f$ is the melt fraction at time of intrusion, $\frac{L}{C}$ the latent heat to specific heat and $G_m$ the gradient of solidus.

Equation 58 accounts for heat lost by the dike as it cools in place and heat lost by its magma during its rise. In this scenario I assume extension takes place over a width of 5 km, similar to oceanic spreading systems. This smaller region of extension leads to a higher strain rate of 5 $\times$ $10^{-14}$ $s^{-1}$, more consistent with typical plate boundary strain rates.

The geotherms for distributed and focused extension are shown in Figure 36c. The increase in temperature with depth for the focused extension model is more rapid than the distributed extension

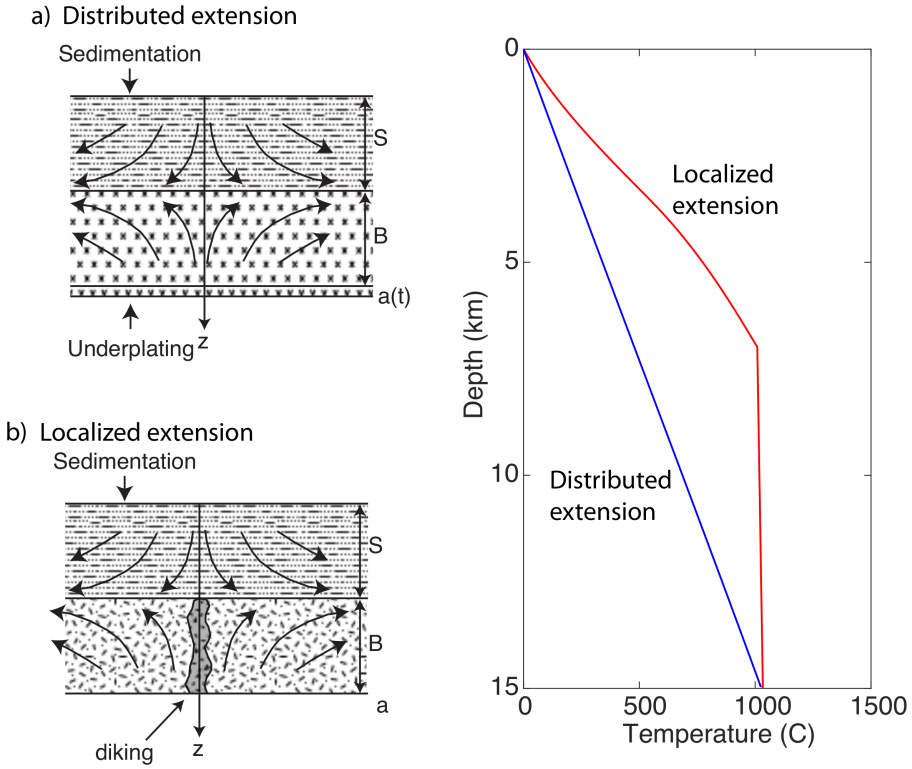


**Figure 36.** a) Pure shear and b) diking model of crustal extension (modified from Lachenbruch *et al.* (1985)). In the diagram S refers to sediment and B is the thickness of underplated material. c) Geotherms corresponding to pure shear (blue) and diking (red) that includes the effects of sedimentation and cooling and crystallization of gabbro.

model because the depth to melt is much shallower; 8.5 km as opposed to 15 km. If there is diking and it has not yet reached the base of the metasediments the geotherm would fall between these two end member models.

We estimated the heat flow by computing the thermal gradient and multiplying through by the thermal conductivity. In the northern Salton Sea, Sass and Elders (1986) report thermal conductivities of 1.8 W $m^{-1}$ $K^{-1}$ for siliclastics with a mean porosity of 26%. These siliclastics are similar to those found in the Wagner basin. The corresponding grain thermal conductivity is 2.8 W $m^{-1}$ $K^{-1}$. I construct a compaction curve based on Athy's law with a surface porosity of 70% and a compaction factor of 0.46 $km^{-1}$, appropriate for this mixture, and compute a thermal conductivity. This calculation yields sediment thermal conductivities that increase from about 0.9 W $m^{-1}$ $K^{-1}$ at the surface to a maximum of 2.7 W $m^{-1}$ $K^{-1}$ at 8.5 km.

At the surface the geotherms corresponding to distributed and localized extension lead to heat flow values of approximately 105 and 165 mW $m^{-2}$, respectively. Sass and Elders (1986) report

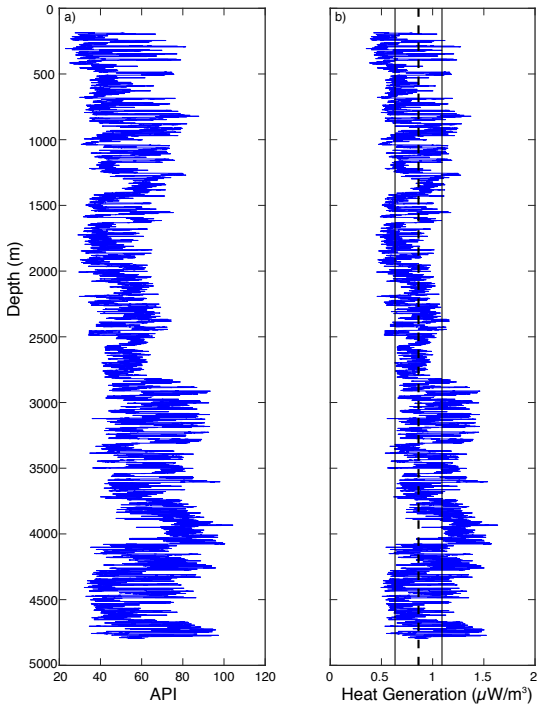


**Figure 37.** a) Gamma Ray log (Martín-Barajas *et al.*, 2006). b) Heat generation, dashed line represents the mean value and the two solid lines the 95% confidence interval

an average radioactive heat production of 1 $\mu$W m$^{-3}$ for the Salton Trough. Radiogenic heat generation is estimated from well logs, using gamma ray GR (Standard American Petroleum Institute, API units). Bücker and Rybach (1996) used a empirical relationship from a small number of wells mostly in Europe:

$$A = 0.0158(GR - 0.8) \tag{63}$$

The analysis of a gamma ray log in the northern part of the Wagner basin shows that the radioactive heat production is 0.86 $\pm$ 0.23 $\mu$Wm$^{-3}$ (Figure 37). For further calculation I used the value reported by Sass and Elders (1986), as we believe this value is appropriate for the Wagner basin.

This value of heat production contributes 8 mW m$^{-2}$ to the surface heat flow and brings our predicted heat flow values to 113 and 173 mW m$^{-2}$, respectively, a 35% difference in heat flow.

Because sedimentation is included in this model we compare these values against our heat flow values uncorrected for sedimentation. The heat flow value for distributed extension compares very well with our observed heat flow of 99 mW $m^{-2}$ and is well within our 95% uncertainty of 14 mW $m^{-2}$.

# Chapter 5. Discussion

We suggest that an observed heat flow of approximately 99$\pm$14 mW m$^{-2}$ and a sedimentation corrected value of $\sim$ 150$\pm$21 mW m$^{-2}$ is appropriate for the central Wagner Basin. The largest uncertainties of our heat flow analysis over the central Wagner Basin stems from our BWT variation correction and the sediment correction. The sensitivity analysis suggests that we can recover heat flow estimates to a few percent in the presence of realistic BWT variations. Comparisons of the values against bottom hole temperatures from nearby boreholes and at depths well below the influence of BWT variations are within the 95% uncertainty of the observed heat flow. Bottom borehole temperatures from PEMEX (Figure 28) are 273°C at 5591 m, 238°C at 4930 m, and 159°C at 3302 m, respectively (Espinoza-Ojeda *et al.*, 2017). These values yield an average thermal gradient of 49.5°C km$^{-1}$ and a heat flow value of 89 mW m$^{-2}$ uncorrected for sedimentation. However, comparisons between the estimated basal heat flow of 150$\pm$21 mW m$^{-2}$ and a Curie isotherm analysis suggests we may be overestimating the sediment correction. The Curie isotherm analysis suggests a basal heat flow of 126 mW m (Sanchez-Zamora *et al.*, 1991). Note the consistency of our sediment corrected heat flow values, the bottom hole temperatures from depths of approximately 5 km and the Curie isotherm analysis based on a depth of approximately 11 km. The consistency of these results suggests, that significant quantities of heat are not being advected from the central Basin to the either the western or eastern flanks.

We interpret the high and scattered heat flow values on the western and eastern margin of the Wagner Basin in terms of advective fluid flow. The Wagner basin is bounded on the east by the Cerro Prieto fault and on the west by the Percebo and Consag fault (González-Escobar *et al.*, 2010). These basin bounding listric normal faults are active and transfer oblique extension between the Wagner and Consag basins. The footwalls of these faults are dissected by numerous faults. We hypothesize that these faults are permeable and focus fluid flow. The main evidence that these anomalies are not due to a conductive source is the large variation over spatial scales of less than a few kilometers. If these anomalies were due to a conductive heat source, the source would need to be very close to the seafloor and there is no evidence for such a source. Testing this hypothesis required additional heat flow data in and out of the plane of the transect and geochemical data.

Moreover, we argue that the lower crust beneath the Wagner Basin has not yet fully ruptured

and underplating is occurring at $\sim$ 15 km, the base of the crust. We suggest underplating may be an important process in weakening the lithosphere just prior to complete rupture and the onset of seafloor spreading. In this environment, underplating occurs as a result of adiabatic upwelling and decompression melting of mantle material during extension. As the underplated material solidifies and cools it warms and weakens the overlying crust. For the Wagner basin, we envision underplating as a precursor to diking during continental rupture.

These models, of course, are clearly an approximation because in reality neither the steady state nor one-dimensional assumptions are completely valid. However, relaxing these assumptions requires data for the Wagner Basin that does not yet exist, such as basement structure, rifting and subsidence history, etc. The thermal time constant associated with diking at 8.5 km is approximately 2 Myr; therefore the steady state equation may not be a bad representation. In contrast, the time constant associated with underplating at 15 km is approximately 7 Myr and given that strain localized approximately 6 Ma, the observed heat flow associated with underplating may be underestimated. The one-dimensional assumption also leads to uncertainties in our analysis. The central part of the Wagner Basin, which we interpret to have seafloor heat flow indicative of conductive conditions at depth, is about 15 km across giving a width/depth ratio of about one for underplating, and may also lead to an underestimate of the surface heat flow. However, given the relatively uniform values of heat flow across the central Wagner Basin, this assumption may be adequate.

Even though our simple pure shear model is in agreement with more sophisticated thermo-mechanical models, supporting the idea of distributed deformation (Persaud *et al.*, 2016), there is evidence of new oceanic crust being produced under the depocenters of the Consag and Delfín Basins farther south (Martín-Barajas *et al.*, 2013; González-Escobar *et al.*, 2014). These authors note the presence of a large amplitude reflector at the base of the sediments at a depth of $\sim$ 4 km, which they interpret as an igneous intrusion. Moreover, south of the Wagner Basin, the San Pedro Mártir fault has been interpreted as a large detachment suggesting simple shearing by low angle detachments. These finding suggests that basins in the northern GC are experiencing contrasting modes of extension and thermal regimes. Understanding the contrasting modes of extension in the northern GC is important to understanding its tectonics, rifting processes and is of economic relevance to the geothermal industry.

In this last regard, the regional value of 150$\pm$21 mW m$^{-2}$ across the central Basin with an area of approximately 1330 km$^2$ yields a heat output of approximately 200 MW. The throughput of the eastern bounding fault and uplifted block, by comparison, is tenfold that of the axial depression.

# Chapter 6. Conclusion

On the basis of the analysis we conclude the following:

1. Conductive heat flow, corrected for sedimentation over the Wagner Basin is about 150±21 mW $m^{-2}$. This value is consistent with 126 mW $m^{-2}$ based on a Curie isotherm analysis (Sanchez-Zamora *et al.*, 1991) but over an order of magnitude less than suggested by Prol-Ledesma *et al.* (2013).

2. The conductive heat loss along the profile varies dramatically. On the western flank, it has a median of $\sim$ 220 mW $m^{-2}$, in the central basin $\sim$ 99 mW $m^{-2}$ and on the eastern flank, where I observe abundant shallow faulting and it crosses the extension of the major Wagner Fault, a median value, for the ten complete penetrations, has a value of $\sim$ 889 mW $m^{-2}$.

3. Distributed and localized extension lead to different predictions of heat flow. The heat flow results are consistent with underplating at a depth of 15 km.

# Bibliography


Aguilar-Campos, C. (2007). *Sísmica de reflexión en el alto Golfo de California*. Master-thesis, CICESE.

Allison, E. C. (1964). Geology of areas bordering gulf of california: A144: Marine geology of the gulf of california. pp. 3–29.

Alvarez, L. G., Suárez-Vidal, F., Mendoza-Borunda, R., and González-Escobar, M. (2009). Bathymetry and active geological structures in the upper gulf of california. *Boletín de la Sociedad Geológica Mexicana*, **61**(1): 129–141.

Alvarez-Borrego, S. and Lara-Lara, J. R. (1991). The physical environment and primary productivity of the gulf of california. *The gulf and peninsular province of the Californias*, **47**: 555–567.

Andrews, E. D. (1991). Sediment transport in the colorado river basin. En: *Colorado River Ecology and Dam Management: Proceedings of a Symposium, May 24–25, 1990, Santa Fe, New Mexico*. pp. 54–74.

Aragón-Arreola, M. and Martín-Barajas, A. (2007). Westward migration of extension in the northern gulf of california, mexico. *Geology*, **35**(6): 571–574.

Aragón-Arreola, M. d. J. (2006). *Evolución estructural de las cuencas del norte y centro del Golfo de California. Implicaciones en la cinemática de apertura y en el acomodo de la deformación*. Ph.d-thesis, CICESE.

Argote, M. L., Amador, A., Lavín, M., and Hunter, J. R. (1995). Tidal dissipation and stratification in the gulf of california. *Journal of Geophysical Research: Oceans*, **100**(C8): 16103–16118.

Athy, L. F. (1930). Density, porosity, and compaction of sedimentary rocks. *AAPG Bulletin*, **14**(1): 1–24.

Baba, J., Peterson, C. D., and Schrader, H. J. (1991). Fine-grained terrigenous sediment supply and dispersal in the gulf of california during the last century: Chapter 28: Part v. physical oceanography, primary productivity, sedimetology.

Beardsmore, G. R. and Cull, J. P. (2001). *Crustal heat flow: a guide to measurement and modelling*. Cambridge University Press.

Bertani, R. (2005). World geothermal power generation in the period 2001–2005. *Geothermics*, **34**(6): 651–690.

Bertani, R. (2012). Geothermal power generation in the world 2005–2010 update report. *Geothermics*, **41**: 1–29.

Birch, F., Roy, R. F., and Decker, E. R. (1968). Heat flow and thermal history in new england and new york. *Studies of Appalachian geology*, pp. 437–451.

Blackwell, J. (1956). The axial-flow error in the thermal-conductivity probe. *Canadian Journal of Physics*, **34**(4): 412–417.

Bücker, C. and Rybach, L. (1996). A simple method to determine heat production from gamma-ray logs. *Marine and Petroleum Geology*, **13**(4): 373–375.

Bullard, E. (1939). Heat flow in south africa. *Proceedings of the Royal Society of London. Series A, Mathematical and Physical Sciences*, pp. 474–502.

Bullard, E. (1954a). The flow of heat through the floor of the atlantic ocean. En: *Proceedings of the Royal Society of London A: Mathematical, Physical and Engineering Sciences*. The Royal Society, Vol. 222, pp. 408–429.

Bullard, E. (1954b). Heat-flow through the floor of the ocean. *Deep Sea Research (1953)*, **1**(2): 65–66.

Carriquiry, J. and Sánchez, A. (1999). Sedimentation in the colorado river delta and upper gulf of california after nearly a century of discharge loss. *Marine Geology*, **158**(1): 125–145.

Carslaw, H. and Jaeger, J. (1959). Heat conduction in solids. *Oxford University Press, Oxford*, p. 75.

Castro, R., Stock, J., Hauksson, E., and Clayton, R. (2017). Active tectonics in the gulf of california and seismicity (m> 3.0) for the period 2002–2014. *Tectonophysics*.

CeMIE-Geo (2014). Centro Mexicano de Inovación en Energía Geotérmica. Recovered from:. http://www.cemiegeo.org/.

Chanes-Martínez, J. J. (2012). *Características estructurales y sismoestratigráficas en un sector del delta del Río Colorado, noroeste de México, a partir de sísmica de reflexión*. Master-thesis, CICESE.

Contreras, J., Martín-Barajas, A., and Herguera, J. C. (2005). Subsidence of the laguna salada basin, northeastern baja california, mexico, inferred from milankovitch climatic changes. *Geofísica Internacional*, **44**(1): 103–111.

Couch, R. W., Ness, G. E., Sanchez-Zamora, O., Calderon-Riveroll, G., Doguin, P., Plawman, T., Coperude, S., Huehn, B., and Gumma, W. (1991). Gravity anomalies and crustal structure of the gulf and peninsular province of the californias: Chapter 3: Part ii. geological and geophysical maps.

Davis, E., Lister, C., Wade, U., and Hyndman, R. (1980). Detailed heat flow measurements over the juan de fuca ridge system. *Journal of Geophysical Research: Solid Earth*, **85**(B1): 299–310.

Di Luccio, F., Persaud, P., and Clayton, R. (2014). Seismic structure beneath the gulf of california: a contribution from group velocity measurements. *Geophysical Journal International*, **199**(3): 1861–1877.

Dorsey, R. J. (2010). Sedimentation and crustal recycling along an active oblique-rift margin: Salton trough and northern gulf of california. *Geology*, **38**(5): 443–446.

Dorsey, R. J., Fluette, A., McDougall, K., Housen, B. A., Janecke, S. U., Axen, G. J., and Shirvell, C. R. (2007). Chronology of miocene–pliocene deposits at split mountain gorge, southern california: A record of regional tectonics and colorado river evolution. *Geology*, **35**(1): 57–60.

Duchkov, A. and Kazantsev, S. (2007). Autumn-winter anomalous variations in bottom water and sediment temperatures in lake teletskoe. *Russian Geology and Geophysics*, **48**(12): 1061–1064.

Díaz-Méndez, G., González-Fernández, A., Marinone-Moschetto, G., Piñero-Lajas, D., and de Dios-Sánchez, D. (2015). Batimetría de alta resolución adquirida durante los cruceros geotermia 2015. *GEOS*, **35**(1): 177.

Espinoza-Ojeda, O., Prol-Ledesma, R., Iglesias, E., and Figueroa-Soto, A. (2017). Update and review of heat flow measurements in méxico. *Energy*.

FIELAX (2017). FIELAX Gesellschaft für wissenschaftliche Datenverarbeitung mbH. Recovered from:. https://www.fielax.de/.

Flores-Armenta, M., Ramírez-Montes, M., and Morales-Alcalá, L. (2014). Geothermal activity and development in mexico–keeping the production going. *Proceedings of the Short Course VI on Utilization of Low-and Medium-Enthalpy Geothermal Resources and Financial Aspects of Utilization", organized by UNU-GTP and LaGeo, in Santa Tecla, El Salvador*, pp. 1–12.

Fowler, C. M. R. (1990). *The solid earth: an introduction to global geophysics*. Cambridge University Press.

Fuis, G., Mooney, W., Healy, J., McMechan, G., and Lutter, W. (1984). A seismic refraction survey of the imperial valley region, california. *Journal of Geophysical Research: Solid Earth*, **89**(B2): 1165–1189.

Fuis, G. S. and Kohler, W. M. (1984). Crustal structure and tectonics of the imperial valley region, california.

Godínez, V., Lavín, M., Galindo-Bect, M., and Sánchez-Velasco, L. (2013). Datos Hidrográficos en el Alto Golfo de California: Campaña PANGAS-1306 (11 al 21 de junio del 2013). Informe ténico 106556. Reporte técnico doi:10.13140/RG.2.1.4622.8645, Departamento de Oceanografía Física, CICESE.

González-Escobar, M., Aguilar-Campos, C., Suárez-Vidal, F., and Martín-Barajas, A. (2009). Geometry of the wagner basin, upper gulf of california based on seismic reflections. *International Geology Review*, **51**(2): 133–144.

González-Escobar, M., Suárez-Vidal, F., Hernández-Pérez, J. A., and Martín-Barajas, A. (2010). Seismic reflection-based evidence of a transfer zone between the wagner and consag basins: implications for defining the structural geometry of the northern gulf of california. *Geo-Marine Letters*, **30**(6): 575–584.

González-Escobar, M., Suárez-Vidal, F., Sojo-Amezquita, A., Gallardo-Mata, C. G., and Martin-Barajas, A. (2014). Consag basin: northern gulf of california, evidence of generation of new crust, based on seismic reflection data. *International Geology Review*, **56**(11): 1315–1331.

González-Fernández, A., Dañobeitia, J. J., Delgado-Argote, L. A., Michaud, F., Córdoba, D., and Bartolomé, R. (2005). Mode of extension and rifting history of upper tiburón and upper delfín basins, northern gulf of california. *Journal of Geophysical Research: Solid Earth*, **110**(B1).

Han, L., Hole, J. A., Stock, J. M., Fuis, G. S., Kell, A., Driscoll, N. W., Kent, G. M., Harding, A. J., Rymer, M. J., González-Fernández, A., *et al.* (2016). Continental rupture and the creation of new crust in the salton trough rift, southern california and northern mexico: Results from the salton seismic imaging project. *Journal of Geophysical Research: Solid Earth*, **121**(10): 7469–7489.

Hartmann, A. (2004). *Ein neues Inversionsverfahren zur Auswertung mariner Wärmestromdichtemessungen*. Diplom, University of Bremen.

Hartmann, A. and Villinger, H. (2002). Inversion of marine heat flow measurements by expansion of the temperature decay function. *Geophysical Journal International*, **148**(3): 628–636.

Helenes, J., Carreño, A., and Carrillo, R. (2009). Middle to late miocene chronostratigraphy and development of the northern gulf of california. *Marine Micropaleontology*, **72**(1): 10–25.

Henyey, T. L. and Bischoff, J. L. (1973). Tectonic elements of the northern part of the gulf of california. *Geological Society of America Bulletin*, **84**(1): 315–330.

Hernández-Pérez, J. A. (2008). *Estructura y estratigrafía en las cuencas Wagner y Consag, Golfo de California, a partir de sísmica de reflexión*. Master-thesis, CICESE.

Hurtado-Brito, J. C. (2012). *Registro volcánico en las cuencas Rift del norte del Golfo de California a partir de sísmica de reflexión*. Master-thesis, CICESE.

Hutnak, M. and Fisher, A. (2007). Influence of sedimentation, local and regional hydrothermal circulation, and thermal rebound on measurements of seafloor heat flux. *Journal of Geophysical Research: Solid Earth*, **112**(B12).

Hyndman, R. D., Davis, E. E., and Wright, J. a. (1979). The measurement of marine geothermal heat flow by a multipenetration probe with digital acoustic telemetry and insitu thermal conductivity. *Marine Geophysical Researches*, **4**(2): 181–205.

Jarvis, A., Reuter, H. I., Nelson, A., Guevara, E., *et al.* (2008). Hole-filled srtm for the globe version 4. *available from the CGIAR-CSI SRTM 90m Database (http://srtm. csi. cgiar. org)*.

Jemsek, J., Von Herzen, R., Rehault, J.-P., Williams, D., and Sclater, J. (1985). Heat flow and lithospheric thinning in the ligurian basin (nw mediterranean). *Geophysical Research Letters*, **12**(10): 693–696.

Klitgord, K. D., Mudie, J. D., Bischoff, J. L., and Henyey, T. L. (1974). Magnetic anomalies in the northern and central gulf of california. *Geological Society of America Bulletin*, **85**(5): 815–820.

Kluesner, J. and Lonsdale, P. (2008). Young saucer-shaped sills within rapidly accumulated sediments of the central gulf of california. En: *AGU Fall Meeting Abstracts*.

Lachenbruch, A. H. (1968). Preliminary geothermal model of the sierra nevada. *Journal of Geophysical Research*, **73**(22): 6977–6989.

Lachenbruch, A. H. and Morgan, P. (1990). Continental extension, magmatism and elevation; formal relations and rules of thumb. *Tectonophysics*, **174**(1-2): 39–62.

Lachenbruch, A. H., Sass, J., and Galanis, S. (1985). Heat flow in southernmost california and the origin of the salton trough. *Journal of Geophysical Research: Solid Earth*, **90**(B8): 6709–6736.

Larson, P. A., D MUDIE, J., and Larson, R. L. (1972). Magnetic anomalies and fracture-zone trends in the gulf of california. *Geological Society of America Bulletin*, **83**(11): 3361–3368.

Lavín, M. and Marinone, S. (2003). An overview of the physical oceanography of the gulf of california. En: *Nonlinear processes in geophysical fluid dynamics*. Springer, pp. 173–204.

Levi, S. and Riddihough, R. (1986). Why are marine magnetic anomalies suppressed over sedimented spreading centers? *Geology*, **14**(8): 651–654.

Levitus, S., Antonov, J., Baranova, O. K., Boyer, T., Coleman, C., Garcia, H., Grodsky, A., Johnson, D., Locarnini, R., Mishonov, A. V., *et al.* (2013). The world ocean database. *Data Science Journal*, **12**: WDS229–WDS234.

Lewis, J. L., Day, S. M., Magistrale, H., Castro, R. R., Astiz, L., Rebollar, C., Eakins, J., Vernon, F. L., and Brune, J. N. (2001). Crustal thickness of the peninsular ranges and gulf extensional province in the californias. *Journal of Geophysical Research: Solid Earth*, **106**(B7): 13599–13611.

Lindquist, K. G., Engle, K., Stahlke, D., and Price, E. (2004). Global topography and bathymetry grid improves research efforts. *EOS, Transactions American Geophysical Union*, **85**(19): 186–186.

Lister, C. (1979). The pulse-probe method of conductivity measurement. *Geophysical Journal International*, **57**(2): 451–461.

Lizarralde, D., Axen, G. J., Brown, H. E., Fletcher, J. M., González-Fernández, A., Harding, A. J., Holbrook, W. S., Kent, G. M., Paramo, P., Sutherland, F., *et al.* (2007). Variation in styles of rifting in the gulf of california. *Nature*, **448**(7152): 466–469.

Lonsdale, P. (1989). Geology and tectonic history of the gulf of california. *The eastern Pacific Ocean and Hawaii: Boulder, Colorado, Geological Society of America, Geology of North America, v. N*, pp. 499–521.

Lonsdale, P. (1991). Structural patterns of the pacific floor offshore of peninsular california. *The gulf and peninsular province of the Californias*, **47**: 87–125.

Lund, J. W. and Boyd, T. L. (2016). Direct utilization of geothermal energy 2015 worldwide review. *Geothermics*, **60**: 66–93.

Mar-Hernández, J. E. (2009). *Tectónica de la cuenca Tiburón a partir de sísmica de reflexión*. Master-thesis, CICESE.

Martín-Barajas, A., Abdeslem-García, J., Helenes-Escamilla, J., González-Escobar, M., Aragón-Arreola, M., and Pacheco-Romero, M. (2006). Evolución Tectonoestratigráfica de las Cuencas del Norte del Golfo de California, Volumen 1, Integración de resultados. Reporte técnico No. 80303843, PEMEX. 63. Reporte técnico, Departamento de Ciencias de la Tierra, CICESE.

Martín-Barajas, A., González-Escobar, M., Fletcher, J. M., Pacheco, M., Oskin, M., and Dorsey, R. (2013). Thick deltaic sedimentation and detachment faulting delay the onset of continental rupture in the northern gulf of california: Analysis of seismic reflection profiles. *Tectonics*, **32**(5): 1294–1311.

Menke, W. (1989). *Geophysical data analysis: Discrete inverse theory*, Vol. 45. Academic press.

Montes, J. M., Lavín, M. F., and Parés-Sierra, A. F. (2015). Seasonal heat and salt balance in the upper gulf of california. *Journal of Coastal Research*, **32**(4): 853–862.

Montoya-Valenzuela, J. A. (2014). *Evidencias basadas en sísmica de reflexión de un sector de tectónica inactiva en el norte del Golfo de California*. Master-thesis, CICESE.

Oskin, M. and Stock, J. (2003). Pacific–north america plate motion and opening of the upper delfín basin, northern gulf of california, mexico. *Geological Society of America Bulletin*, **115**(10): 1173–1190.

Oskin, M., Stock, J., and Martín-Barajas, A. (2001). Rapid localization of pacific–north america plate motion in the gulf of california. *Geology*, **29**(5): 459–462.

Pacheco, M., Martín Barajas, A., Elders, W., Espinosa Cardeña, J. M., Helenes, J., and Segura, A. (2006). Stratigraphy and structure of the altar basin of nw sonora: Implications for the history of the colorado river delta and the salton trough. *Revista Mexicana de Ciencias Geológicas*, **23**(1).

Pérez-Cruz, G. (1980). Exploración petrolera de la porción noroccidental del golfo de california. *Bol. Asoc. Mex. Geofıs. Explor*, **21**: 3–4.

Persaud, P. (2004). *Images of Early Continental Breakup in and around the Gulf of California and the Role of Basal Shear in Producing Wide Plate Boundaries*. Ph.d-thesis, California Institute of Technology.

Persaud, P., Stock, J. M., Steckler, M. S., Martín-Barajas, A., Diebold, J. B., González-Fernández, A., and Mountain, G. S. (2003). Active deformation and shallow structure of the wagner, consag, and delfín basins, northern gulf of california, mexico. *Journal of Geophysical Research: Solid Earth*, **108**(B7).

Persaud, P., Di Luccio, F., and Clayton, R. W. (2015). Rayleigh wave dispersion measurements reveal low-velocity zones beneath the new crust in the gulf of california. *Geophysical Research Letters*, **42**(6): 1766–1774.

Persaud, P., Tan, E., Contreras, J., and Lavier, L. (2016). A bottom-driven mechanism for distributed faulting in the gulf of california rift. *Tectonophysics*.

Plattner, C., Malservisi, R., Dixon, T. H., LaFemina, P., Sella, G., Fletcher, J., and Suarez-Vidal, F. (2007). New constraints on relative motion between the pacific plate and baja california microplate (mexico) from gps measurements. *Geophysical Journal International*, **170**(3): 1373–1380.

Pollack, H. N., Hurter, S. J., and Johnson, J. R. (1993). Heat flow from the earth's interior: analysis of the global data set. *Reviews of Geophysics*, **31**(3): 267–280.

Powell, W., Chapman, D., Balling, N., Beck, A., Haenel, R., Rybach, L., and Stegena, L. (1988). Continental heat flow density. *Handbook of Terrestrial Heat Flow Density Determination, edited by R. Haenel, R. Rybach, and L. Stegena*, pp. 167–222.

Prol-Ledesma, R. M., Torres-Vera, M.-A., Rodolfo-Metalpa, R., Ángeles, C., Deveze, C. H. L., Villanueva-Estrada, R. E., Shumilin, E., and Robinson, C. (2013). High heat flow and ocean acidification at a nascent rift in the northern gulf of california. *Nature communications*, **4**: 1388.

QGIS Development Team (2009). *QGIS Geographic Information System*. Open Source Geospatial Foundation.

RESNOM (2015). Red Sísmica del Noroeste de México, Departamento de Sismología del Centro de Investigación Científica y Educación Superior de Ensenada. Baja California, México. Recovered from: . http://resnom.cicese.mx.

Revelle, R. and Maxwell, A. E. (1952). Heat flow through the floor of the eastern north pacific ocean. *Nature*, **170**(4318): 199–200.

Rodríguez-Iturbe, I. and Rinaldo, A. (2001). *Fractal river basins: chance and self-organization*. Cambridge University Press.

Roy, R. F., Blackwell, D. D., and Birch, F. (1968). Heat generation of plutonic rocks and continental heat flow provinces. *Earth and Planetary Science Letters*, **5**: 1–12.

Sanchez-Zamora, O., Doguin, P., Couch, R., and Ness, G. (1991). Magnetic anomalies of the northern gulf of california: Structural and thermal interpretations: Chapter 22: Part iii. regional geophysics and geology.

Sass, J. and Elders, W. (1986). Salton sea scientific drilling project: Scientific program. *Trans. Geothermal Resources Council*, **10**: 473–478.

Smith, D. L. (1974). Heat flow, radioactive heat generation, and theoretical tectonics for northwestern mexico. *Earth and Planetary Science Letters*, **23**(1): 43–52.

Sojo-Amezquita, A. (2012). *Características estructurales de la frontera entre las cuencas Consag y Delfín Superior, Golfo de California, México*. Master-thesis, CICESE.

Stein, C. A. and Stein, S. (1994). Constraints on hydrothermal heat flux through the oceanic lithosphere from global heat flow. *Journal of Geophysical Research: Solid Earth*, **99**(B2): 3081–3095.

Stober, I. and Bucher, K. (2012). *Geothermie*. Springer.

Stock, J. M. and Lee, J. (1994). Do microplates in subduction zones leave a geological record? *Tectonics*, **13**(6): 1472–1487.

Sánchez-García, A. C. (2013). *Rasgos estructurales en el suroeste del delta del Río Colorado : interpretación de perfiles de sísmica de reflexión*. Master-thesis, CICESE.

Turcotte, D. L. and Schubert, G. (2014). *Geodynamics*. Cambridge University Press.

Umhoefer, P. J. (2011). Why did the southern gulf of california rupture so rapidly?—oblique divergence across hot, weak lithosphere along a tectonically active margin. *GSA Today*, **21**(11): 4–10.

Vega-Saucedo, G. A. (2014). *Características sismoestructurales de una región al suroeste del delta del Río Colorado, a partir de sísmica de reflexión 2D*. Master-thesis, CICESE.

Villinger, H. and Davis, E. E. (1987). A new reduction algorithm for marine heat flow measurements. *Journal of Geophysical Research: Solid Earth*, **92**(B12): 12846–12856.

Von Herzen, R. P., Detrick, R. S., Crough, S. T., Epp, D., and Fehn, U. (1982). Thermal origin of the hawaiian swell: Heat flow evidence and thermal models. *Journal of Geophysical Research: Solid Earth*, **87**(B8): 6711–6723.

Wessel, P. and Smith, W. H. (1998). New, improved version of generic mapping tools released. *Eos, Transactions American Geophysical Union*, **79**(47): 579–579.